Mechanistic Study of Surface Enhanced Raman Scattering for High Sensitivity PAH Detection in Water

by

©Abhijit Chatterjee

A Dissertation submitted to the School of Graduate Studies in partial fulfillment of the requirements for the degree of

Doctor of Philosophy

Department of Chemistry

Memorial University of Newfoundland

January 2018

St. John's Newfoundland

Abstract

The main objective of this thesis is the study of surface enhanced Raman scattering (SERS) mechanisms in order to fabricate efficient SERS substrates for the trace detection of PAHs. SERS is gaining tremendous attention in environmental pollutant sensing. SERS mainly relies on the plasmonic enhancement of the Raman signal from metal nanoparticles on the SERS substrate. In addition, metal–molecule charge transfer upon analyte adsorption is also important. Therefore, a study of the SERS enhancement mechanism is crucial in order to design an efficient SERS substrate. Polycyclic aromatic hydrocarbons (PAHs; phenanthrene, pyrene etc.) gained our attention due to their impact on the environment. PAHs dissolve in water at trace concentrations. Therefore, PAH sensing is challenging using typical environmental monitoring techniques. In this thesis, the SERS technique was employed to detect PAHs (phenanthrene and pyrene) with enhancement factors (EFs) of 10^5 to 10^6.

The SERS activities of different types of substrates (metal-semiconductor, bimetallic, metal-insulator) were tested, and the Raman enhancement mechanism was investigated using plasmon absorption studies, scanning probe microscopy, and other spectroscopic and microscopic techniques. A synergistic effect of electromagnetic and chemical enhancement on the SERS performance was illustrated with scanning probe microscopy. This thesis presents new applications or extensions of materials characterization methods, including Kelvin probe force microscopy (KPFM) and electrostatic

force microscopy (EFM), to the SERS mechanism question.

A range of materials was used to create the SERS substrates through multilayer deposition. In all cases, the top layer consisted of Au, Ag, or both. These plasmonic materials were supported by ZnO or silica spheres, whose morphology contributed to hotspot formation, plasmon tuning, and surface hydrophobicity. Substrate's surface morphology was tuned by varying the film preparation methods. Some methods allowed for independent tuning of surface roughness and surface area, two distinct contributors to enhancement.

The semiconducting and insulating supports also electronically impacted the top metal layer. By varying the method of preparation of the ZnO, or by adding an insulating poly(methyl methacrylate) (PMMA) interlayer, both the morphology and the electronic interactions were tuned. Different surface electronic interactions between the metal and the analyte were linked to chemical enhancement.

Among Au/ZnO substrates, Au possessed a partial positive surface charge as a result of Fermi level equilibrium with certain types of ZnO, while defect-rich ZnO led to a negative surface charge on Au. Bimetallic films with Au and Ag similarly generated a positive or negative surface charge on the substrate depending on which metal was on top. The direct measurement of surface charge, enabled by EFM, explained why these surface charges impacted the EFs in an analyte-specific way.

Tuning the SERS activity of Au/ZnO by the elimination of impurities in ZnO was also studied. The types of ZnO impurities and defects were identified by X-ray diffraction (XRD), Raman, thermogravimetric analysis (TGA), cathodoluminescence (CL), electron paramagnetic resonance (EPR), X-ray photoelectron spectroscopy (XPS), which were also used to identify changes in defects and impurities during the optimization of substrate preparation.

Acknowledgements

Foremost, I would like to express my deepest gratitude to my supervisor Prof. Erika Merschrod for giving me the opportunity to conduct my doctoral degree under her esteemed supervision. Her constant support of the development of my research plans and their execution are highly appreciated. Her valuable suggestions on my thesis, conference presentation and research seminars were immensely helpful.

I would also like to convey my acknowledgment of Dr. Christopher Rowley and Dr. Cora Young as members of my supervisory committee for their significant amount of help and support. They were always accessible and encouraging to me during every step of my degree program.

I am grateful to my fellow Merschrod group members for their constant help and being friendly in every moment. I would like to convey my special appreciation to Dr. Dmytro Grebennikov (former post-doctoral fellow) for his valuable guidance on research. Words are not enough to express my special thanks to David Gale for his friendship and making my life smooth in St. John's. I am also thankful to Amarender Manchoju, Nick Ryan and Tiber Reardon for their constant encouragement and always being great friends to me.

I am grateful to Prof. Anand Yethiraj and Prof. Raymond Poirier for their extensive help during courses and as well as providing references for my post doctoral applications.

I would like to express my deepest gratitude to Prof. Travis Fridgen and Prof. Len Zedel for their encouragement and constant support during my thesis submission.

I am also thankful to Prof. M. J. Clouter (MUN Department of Physics and Physical Oceanography) for the use of the metal evaporator, Technical Services (MUN) for operational assistance, and Dr. W. Aylward (MUN CREAIT network) for technical assistance with XRD and SEM.

The Chemistry general office stuff are gratefully thanked for being supportive and helpful.

I would not have been to reach this position if I did not have support and encouragement from my Mother. Therefore, I would like to dedicate all of my achievements to her – who is the most important person in my life.

I would like to express my deepest gratitude for funding resources to the Natural Sciences and Engineering Research Council of Canada, Canada Foundation for Innovation and the Research Development Corporation, the Atlantic Innovation Fund and the School of Graduate studies (Memorial University). I am thankful to Compute Canada and ACEnet for providing me with the necessary resources for computational work.

Table of Contents

Abstract ii

Acknowledgments iv

List of Tables xv

List of Figures xxiii

List of Abbreviations and Symbols xxiv

1 Introduction 1

1.1 Motivation 1

1.1.1 Polycyclic aromatic hydrocarbons (PAHs) as environmental pollutants 1

1.1.2 PAH sensing techniques 2

1.2 Current advances in SERS detection of PAHs 3

1.3 Raman spectroscopy 4

1.3.1 Origin and fundamentals of Raman spectroscopy 4

1.4 Surface enhanced Raman scattering 6

1.4.1 Electromagnetic enhancement: Surface plasmons 7

1.4.2 Distance dependence of enhancement 11

1.4.3 Adsorption effects 12
1.4.4 Charge-transfer enhancement mechanism 15
1.5 SERS mechanistic studies 16
1.5.1 Theoretical approaches 16
1.5.2 Experimental approaches 20
1.6 SERS substrate fabrication 27
1.6.1 Chemical synthesis 27
1.6.2 Nanofabrication 28
1.7 Multicomponent SERS substrates 30
1.7.1 Metal-semiconductor substrates 30
1.7.2 Bimetallic substrates 31
1.8 Summary 31
1.8.1 Chapter 2: Surface Potential and Morphological Mapping to Investigate Analyte Adsorption Effects on Surface Enhanced Raman Scattering (SERS) 32
1.8.2 Chapter 3: Thermal Annealing: A Three-fold Approach to Improving Surface Enhanced Raman Scattering (SERS) Activity of Metal-semiconductor Substrate 33
1.8.3 Chapter 4: SERS Detection Using Metal-insulator Multilayers: Effect of Insulator on Plasmonic Enhancement 33
1.8.4 Chapter 5: Effect of ZnO Defects on SERS Activity of Au/ZnO Hybrid Films 33
1.8.5 Chapter 6: Direct Evidence of Surface Charge Controlled SERS Activity in a Bilayer Metal Film by EFM 34

1.8.6 Chapter 7: Kelvin Probe Force Microscopy to Probe Metal–molecule Interactions: A Comparative SERS Sensing of Phenanthrene and Pyrene 34

Bibliography 34

Co-authorship Statement **54**

2 Surface Potential and Morphological Mapping to Investigate Analyte Adsorption Effects on Surface Enhanced Raman Scattering (SERS) **56**

2.1 Abstract 56

2.2 Introduction 57

2.3 Experimental 59

2.4 Results and discussion 59

2.5 Conclusions 65

Bibliography 66

3 Thermal Annealing: A Three-fold Approach to Improving Surface Enhanced Raman Scattering (SERS) Activity of Metal-semiconductor Substrate **73**

3.1 Abstract 73

3.2 Introduction 74

3.3 Experimental 75

3.4 Results and discussion 75

3.5 Conclusions 83

Bibliography 84

4 SERS Detection Using Metal-insulator Multilayers: Effect of Insulator on Plasmonic Enhancement **89**

4.1 Abstract . . . 89
4.2 Introduction . . . 90
4.3 Experimental details . . . 91
4.3.1 Materials . . . 91
4.3.2 Synthesis of SERS substrate . . . 91
4.3.3 SERS measurement . . . 93
4.4 Results and discussion . . . 94
4.4.1 SERS performance . . . 94
4.4.2 The role of the PMMA layer: a comparison between A_n, B_n, and C_n substrates . . . 95
4.4.3 Detection at environmentally-relevant levels. . . . 97
4.5 Conclusions . . . 98
Bibliography . . . 99

5 Effect of ZnO Defects on SERS Activity of Au/ZnO Hybrid Films 104
5.1 Abstract . . . 104
5.2 Introduction . . . 104
5.3 Experimental . . . 106
5.3.1 Materials . . . 106
5.3.2 Au/ZnO film synthesis . . . 106
5.3.3 Characterization methods and instrumentation . . . 107
5.3.4 SERS experiment . . . 109
5.4 Results and discussion . . . 109
5.4.1 ZnO crystallite and film morphology . . . 109
5.4.2 ZnO crystallographic analysis . . . 110
5.4.3 ZnO electronic structure . . . 110
5.4.4 SERS activity . . . 112

5.5 Conclusions . . . 113
Bibliography . . . 114

6 Direct Evidence of Surface Charge Controlled SERS Activity in a Bilayer Metal Film by EFM 121

6.1 Abstract . . . 121
6.2 Introduction . . . 122
6.3 Experimental procedure . . . 123
6.3.1 Materials . . . 123
6.3.2 Synthesis of SERS substrate . . . 123
6.3.3 Characterization methods . . . 124
6.4 Results and discussion . . . 127
6.4.1 SERS study . . . 127
6.4.2 EFM study . . . 129
6.5 Conclusions . . . 131
Bibliography . . . 132

7 Kelvin Probe Force Microscopy to Probe Metal–molecule Interactions: A Comparative SERS Sensing of Phenanthrene and Pyrene 136

7.1 Abstract . . . 136
7.2 Introduction . . . 137
7.3 Experimental details . . . 138
7.3.1 Materials . . . 138
7.3.2 Synthesis of SERS substrate . . . 139
7.3.3 Characterization methods . . . 139
7.3.4 SERS measurement . . . 140
7.3.5 Computational details . . . 140

7.4 Results and discussion . . . 140
7.4.1 SERS performance . . . 140
7.4.2 KPFM study . . . 142
7.5 Conclusions . . . 143
Bibliography . . . 144

8 Conclusions and Future Direction **150**
8.1 Conclusions . . . 150
8.1.1 Fundamental advances . . . 150
8.1.2 Practical applications . . . 153
8.2 Future Direction . . . 153
8.2.1 Background . . . 154
8.2.2 Experimental approach . . . 155
Bibliography . . . 156

A Supporting Information: Chapter 2 **157**
A.1 ZnO film synthesis . . . 157
A.2 XRD and SEM instrumental details . . . 158
A.3 Raman analysis . . . 159
A.4 Plasmon absorption of different substrates . . . 159
A.5 Enhancement factor (EF) calculations . . . 160
A.6 SERS activity of only Au and only ZnO . . . 162
A.7 Surface area, roughness, and work function measurements . . . 163

B Supporting Information: Chapter 3 **165**
B.1 ZnO film synthesis . . . 165
B.2 XRD and SEM instrumental details . . . 165
B.3 Raman microscopy . . . 166

B.4 Thermogravimetric analysis 166
B.5 DRS technique 167
B.6 Enhancement factor calculation 168
B.7 Contact angle measurement 168
B.8 Atomic force microscopy 168
B.9 Cathodoluminescence (CL) analysis 169

C Supporting Information: Chapter 4 **171**
C.1 Substrate fabrication 171
C.2 Characterization methods 172
C.2.1 FESEM 172
C.2.2 Scanning probe microscopy (SPM) 172

D Supporting Information: Chapter 5 **174**
D.1 The differences between Au/ZnO hybrids in Chapter 2 and 5 174
D.2 Enhancement factor calculation 176
D.3 XPS and EPR spectra 176
D.4 Roughness of Au/ZnO film 177
D.5 Exploring the possibility of Au doping 177
D.5.1 XRD data 178
D.5.2 Local bonding: Raman and XPS evidence 179
D.5.3 ZnO luminescence: defects and charge transfer 181

E Supporting Information: Chapter 6 **183**
E.1 Surface morphological information of monometallic substrates 183
E.2 EF and surface charge of 25 and 15 nm thick Au and Ag bimetallic SERS substrates 184

F Supporting Information: Chapter 7 **185**

F.1 SERS performance with 10 nm of Au 185

F.2 Computational Raman spectra of PAHs in gas phase 186

Bibliography 187

List of Tables

1.1 Crystal shapes and defects of the different types of ZnO used in this thesis, by chapter. 32

1.2 Different ZnO synthesis parameters used in this thesis, specifying the mole ratio of [Zn] to [OH] in the starting materials, additives, reaction times and temperatures, and settling times. 32

2.1 Surface area, enhancement factor (EF), and surface area corrected enhancement factor (EF*) for different substrates. 61

2.2 Work function Φ for Au films of varying thicknesses. The change in Φ with thickness for Au films on ZnO is markedly different than for Au films on glass, as a result of the Fermi level equilibrium with ZnO. . . 64

3.1 A direct relationship between the surface roughness factor (R_q) and the hydrophobicity (water contact angle). 80

4.1 List of SERS substrates. All consist of Au on PMMA on SiO_2 spheres on glass. 92

5.1 EFM phase shift ($\Delta\varphi$) determines the surface charge of the gold surface on Au/ZnO substrate. 111

6.1 List of monometallic and bilayer metallic SERS substrates 124

6.2 EF of monometallic and bimetallic films for pyrene sensing 129

7.1 Link between $\Delta\Phi$ and EF for two PAHs. 143

A.1 Roughness factors of different thicknesses of Au on ZnO. 164

B.1 Surface area (per μm^2) for different SERS substrates. 169

C.1 Surface roughness and EFs for samples with 35 nm Au. 172

D.1 Comparison of lattice parameters a and c between ZnO crystals of Chapters 2 and 5 175

D.2 EFM phase shift ($\Delta\varphi$) to determine the quality of surface charge on the gold in Au/ZnO substrates. 175

D.3 The change of lattice parameters (a and c) of ZnO with Au incorporation compared to analogous samples from Chapter 2. 178

D.4 The ZnO crystal domain size D increases with Au thickness for the defect-rich ZnO, unlike for the ZnO in Chapter 2. 179

E.1 Surface roughness and surface area (5×5 μm^2 scan image) of monometallic substrate and relation with EF 183

E.2 Consistency of surface charge controlled SERS of 25 and 15 nm thick Au and Ag bimetallic substrates. 184

List of Figures

1.1 Elastic Rayleigh scattering and inelastic Raman scattering. 5

1.2 Enhancement factor variation with distance from a gold tip. 12

1.3 Different Langmuir isotherm depending on the molecular orientation on the rough surface. 14

1.4 (a) Molecule on a rough Au surface and (b) molecule in a sandwich between Au spheres and a planar Au surface. 15

1.5 Electronic excitation mediated chemical enhancement in SERS: HOMO–LUMO electronic transition from the Raman laser (left), and metal to molecule electron transfer from excitation by the Raman laser (right). 16

1.6 The electric field distribution in (a) Ag/Ge and (b) Ag/Si. Ag/Ge shows a more intense plasmonic field at the junction. 18

1.7 Wavelength dependent SERS activity. The 785 nm laser delivers the highest Raman enhancement because it matches the plasmon absorption maximum of the SERS substrate. 21

1.8 The consistency of theoretical (BEM) and experimental (CL, labelled as "SEM") plasmon modes. 23

1.9 Higher order plasmon modes have been mapped with EELS, but CL failed to resolve. 24

1.10 SPM images of different silver surfaces. 26

1.11 Steps involved in nanosphere lithography (NSL) to produce highly ordered NP arrays. 29

2.1 The XRD data (left) shows the wurtzite crystal structure of ZnO with $Zn(OH)_2$ contaminants. The FESEM image (right) depicts rod shaped ZnO crystals. 60

2.2 A35 (blue) shows the highest SERS activity, which is comparable to that of A45 (red) and A25 (black) and greater than that of A15 (green). Symbols indicate enhanced Raman modes of phenanthrene. Spectra are offset for clarity. 61

2.3 Concurrent KPFM and morphology scans of A35. 64

2.4 Both surface roughness (R_q) and surface charge (through the work function, Φ) are controlling factors of the Au thickness dependent Raman enhancement (EF^*). 65

2.5 The intensity of the 710 cm^{-1} peak increases with higher concentrations of analyte. The relation between concentration and intensity follows a (non-linear) Langmuir adsorption profile. 66

3.1 A) FESEM images of unannealed and annealed ZnO crystals show the formation of fractures due to annealing. B) XRD data of annealed and unannealed ZnO crystals indicate structural changes with the heat treatment: Unannealed ZnO (red), 200°C annealed (blue) and 400°C annealed (black) (graphs are offset for clarity). 76

3.2 Au-covered annealed ZnO yields substrates (AZ200, blue; AZ400, black) with higher plasmonic absorption relative to Au on unannealed ZnO (AZRT, red). 78

3.3 SERS spectra of phenanthrene on different Au/ZnO substrates: AZ400 (black) has the highest SERS activity in comparison to AZ200 (blue) and AZRT (red). (Plots are offset for clarity). 79
3.4 Photographs or water droplets on Au covered ZnO substrates showing the change in hydrophobicity after thermal treatment. 80
3.5 Plot showing a linear relationship between the roughness factor and the water contact angle. The r^2 value for the fit (red line) is 0.9973. . 81
3.6 A consistent change of CPD of adsorbed phenanthrene on Au covered heat treated ZnO substrate. 81
3.7 Quantitative detection of phenanthrene by SERS. The Raman intensity decreases linearly with the concentration of phenanthrene (see inset, $r^2 = 0.9985$). A log-linear plot shows more clearly the intensities at different concentrations. 83

4.1 FESEM image of a sphere coated substrate. 92
4.2 The SERS spectrum (red, 1 ppm phenanthrene solution on an A2 substrate) and the normal Raman spectrum (blue, 0.1 M phenanthrene solution on a glass slide). Graphs are offset for a clear view. 94
4.3 PMMA-thickness dependent SERS activity of substrates. The PMMA layer thickness decreases from left (A_n) to right (C_n). EFs of 15 and 25 nm thick Au layers decrease with decreasing PMMA thickness. In contrast, 35 nm thick Au layer shows opposite trend. 95
4.4 Poor SERS activity of 25 nm of Au on PMMA-free SiO_2 spheres compared to 25 nm of Au on PMMA-coated SiO_2 spheres. Spectra are offset for clarity. 97

4.5 The Raman signal intensity increases with increasing phenanthrene concentration. The log-linear plot emphasizes the broad range of detectable concentrations. 98

5.1 FESEM image of a ZnO film shows the packing of triangular crystals into a dumbbell-shaped cluster. 109

5.2 XRD data confirms the wurtzite crystal structure. Peak positions and peak widths change with the addition of a Au layer. 110

5.3 Work function of Au/ZnO vs Au/glass, shows negative surface charge formation on Au surface in Au/ZnO. 112

5.4 SERS activity of Au/ZnO substrates towards phenanthrene. 30 nm Au/ZnO and 20 nm Au/ZnO show considerable SERS activity of phenanthrene detection. 10 nm Au/ZnO is SERS inactive. Spectra are offset for clarity. 113

5.5 Plasmonic absorption spectra of 10 nm Au/ZnO (black), 20 nm Au/ZnO (violet) and 30 nm Au/ZnO (green). 10 nm of Au film on ZnO shows significantly lower plasmonic response at the laser excitation wavelength (830 nm). 114

6.1 Phase shift differences between 3 V and –3 V is highest compared to 2 V/–2 V and 1 V/–1 V revealing higher voltage can lead to higher amount of tip-sample Coulombic interaction to determine surface charge more accurately. 126

6.2 SERS response of pyrene with Au (black) and Ag (green). In this case, monometallic Au has higher SERS activity than Ag. Spectra are offset for clarity. 128

6.3 SERS response of pyrene with Ag on top of Au (B1, blue) and Au on top of Ag (B2, red). Ag on top of Au demonstrates high SERS activity relative to Au on Ag. Spectra are offset for clarity. 129

6.4 Phase shift of Ag on Au system (B1). Phase shifts from –3 V (left) and 3 V (right). 130

6.5 Phase shift ($\Delta\varphi$) of Ag on Au (B1, top) and Au on Ag (B2, bottom). This data indicates a positive surface charge with Ag on top and a negative surface charge for Au as the top layer in the bilayer metallic films. In some cases, the error bars are smaller than the symbol. . . . 131

6.6 Phase shift of Ag film (M1, top) and Au film (M2, bottom). No considerable deviation of $\Delta\varphi$ between +3 V and –3 V, which supports a neutral surface charge on the monometallic films. The error bars are smaller than the symbol. 132

7.1 SERS spectra of phenanthrene (black) and pyrene (red). Pyrene shows notable Raman enhancement compared to phenanthrene. Dots indicate principal peaks. Spectra are offset for clarity. 141

8.1 SERS spectra of phenanthrene under exposure of 633 nm (top) and 830 mm (bottom) of Raman laser wavelengths. Au 35 nm (red), Au 25 nm (black) and Au 15 nm (blue) on ZnO film. The laser wavelength dependent SERS activity is demonstrated here. 15 nm of Au on ZnO shows highest SERS activity under 830 nm of Raman laser exposure, while 35 nm of Au on ZnO is the superior one with 633 nm of Raman laser. Graphs are offset for clarity. 154

A.1 FESEM image of a film of rod shaped ZnO crystals, taken at lower magnification than the image in Figure 1 in Chapter 2. 158

A.2 Raman spectrum of ZnO shows three characteristic ZnO Raman peaks. 159

A.3 Optical absorption of different thicknesses of Au covered ZnO shows higher plasmon absorption of A45 (red) and A35 (blue) over A15 (green) and A25 (black). 160

A.4 The plasmon absorption spectrum of a 35 nm thick Au film on glass alone does not show any absorption near the Raman excitation wavelength. This spectrum was recorded using a transmission geometry since Au on glass generates a relatively transparent film. 161

A.5 A comparison of Raman signal at 710 cm^{-1} for phenanthrene solutions of 1 ppm, 0.1 ppm, 0.01 ppm and 0.001 ppm (1 ppb). The spectra are offset for clarity. 162

A.6 Both Au and ZnO films alone are SERS inactive. 162

A.7 Masking procedure to calculate surface area of Au covered ZnO nanorods. The screen capture is from the Asylum Research procedures within IGOR. In this example, the 1 μm^2 small gray box in the image at left has a surface area of 1.4 μm^2. This approach was used to select data for the work function calculations as well, selecting areas near the centers of crystals. 164

B.1 Raman spectra of different types of ZnO films (unannealed ZnO (red), 200°C ZnO (blue) and 400°C ZnO (black); Spectra are offset for clarity.). Annealed ZnO spectra have the characteristic 438 cm^{-1} peak. . 166

B.2 Thermogravimetric analysis of ZnO film shows the water elimination process during heat treatment. 167

B.3 CL spectra show the change of band gap of ZnO with annealing. . . . 170

C.1 Schematic representation of Au-PMMA-SiO_2 sphere substrate synthesis. Au is deposited on top of the PMMA-coated SiO_2 spheres and at the junction of the spheres. 171

C.2 No SERS activity was observed with substrates of only SiO_2 spheres, only PMMA, or PMMA-SiO_2, when exposed to a 1 ppm aqueous solution of phenanthrene. The peaks below 1000 cm^{-1} are characteristic of the PMMA film itself. Spectra are offset for clarity. 173

D.1 Low crystallinity of ZnO was observed in Au doping studies compare to ZnO in Chapter 2. 174

D.2 The different onset of optical absorption of ZnO in Chapter 2 and Chapter 5 reveals different electronic structure of two ZnO. 175

D.3 A shift of $4f_{7/2}$ peak with increasing Au thickness on ZnO indicates Au–ZnO interaction. 176

D.4 EPR spectra for ZnO (red), 10 nm Au/ZnO (black), 20 nm Au/ZnO (violet) and 30 nm Au/ZnO (green). All spectra have the same gyromagnetic ratio with nearly the same spin counts, which is related to oxygen concentration in ZnO. 177

D.5 Roughness of different thicknesses of Au on glass (solid line) and Au on ZnO (dashed line). 178

D.6 Raman spectra of ZnO and Au/ZnO samples showing significant changes in the vibrational modes with thicker Au films. 180

D.7 CL spectra show a drop in the ZnO defect emission peak with increased thickness of the Au film. 181

E.1 Surface roughness controls SERS activity in monometallic case. . . . 184

F.1 SERS spectra of phenanthrene (black) and pyrene (red) on 10 nm of Au on SiO_2 spheres show pyrene has high SERS intensity relative to phenanthrene. Spectra are offset for clarity. 185
F.2 Computed Raman modes of phenanthrene (gas phase). 186
F.3 Computed Raman modes of pyrene (gas phase). 186

List of Abbreviations and Symbols

AFM	Atomic force microscopy
BEM	Boundary element method
CCD	Charge coupled device
CL	Cathodoluminescence
CPD	Contact potential difference
CT	Charge Transfer
CTAB	Cetyltrimethylammonium bromide
TPR	Tetratricopeptide repeat
DDA	Discrete dipole approximation
DFT	Density functional theory
EELS	Electron-energy-loss spectroscopy
EF	Enhancement factor
EFM	Electrostatic force microscopy
EPR	Electron paramagnetic resonance
FDTD	Finite-difference-time-domain
FESEM	Field emission scanning electron microscopy
FWHM	Full width at half maximum
HPLC	High-performance liquid chromatography
HOMO	Highest occupied molecular orbital

KPFM	Kelvin probe force microscopy
LOD	Limit of detection
LSPR	Localized surface plasmon resonance
LUMO	Lowest unoccupied molecular orbital
MIP	Molecularly imprinted polymers
M-m	Metal-molecule
NP	Nanoparticle
PAH	Polycyclic aromatic hydrocarbon
PDMS	Polydimethylsiloxane
PMMA	Poly(methyl methacrylate)
QCM	Quartz crystal microbalance
RPA	Random phase approximation
RT	Room temperature
SEM	Scanning electron microscopy
SERS	Surface enhanced Raman scattering (or spectroscopy)
SKPM	Scanning Kelvin probe microscopy
SPM	Scanning probe microscopy
SPME	Solid phase microextraction
SPP	Surface plasmon polariton
SPR	Surface plasmon resonance
TDDFT	Time dependent density functional theory
TERS	Tip enhanced Raman spectroscopy
TGA	Thermogravimetric analysis
UV-Vis	Ultraviolet-visible
Vis-NIR	Visible-near infrared
WF	Work function

XPS	X-ray photoelectron spectroscopy
XRD	X-ray diffraction

Chapter 1

Introduction

1.1 Motivation

1.1.1 Polycyclic aromatic hydrocarbons (PAHs) as environmental pollutants

Polycyclic aromatic hydrocarbons (PAHs) are a class of aromatic organic compounds that consist of two or more fused benzene rings with shared carbon atoms. [1] They occur mostly as a colorless, white, or yellow solid. Phenanthrene and anthracene are the most common PAHs, and consist of three fused benzene rings, whereas pyrene has four fused rings. Naphthalene, with two aromatic rings, is not a true polycyclic aromatic hydrocarbon, but is instead known as a bicyclic aromatic compound. PAHs have high boiling and melting points and very low solubility in water. PAHs primarily form during incomplete combustion of oil and coal.

The occurrence of PAHs is generally classified as pyrogenic, petrogenic, or biological. [2, 3] PAHs form from pyrolysis, when organic compounds decompose under high temperature in very low oxygen or no-oxygen environments. This incomplete

combustion, whether of fuels in vehicles or from wood burning, generates PAHs as by-products. Petrogenic PAHs are released by crude oil spills during extraction or transport, whether on land or at sea. Spills on sea water can eventually impact coastal land, so the release of oils in the environment can impact numerous ecosystems. Biological PAHs can be formed as a residue through incomplete oxidation in some biological reactions. Microbe-mediated degradation of vegetative matter also produces PAHs.

PAHs are toxic and cause both mutagenic and carcinogenic effects in mammals. [2, 4, 5] Due to the nonpolar property of PAHs, they can easily dissolve in lipids and stay in body fat. Cytochrome P450 based mixed oxidases metabolize PAHs to various epoxides, which are highly reactive and carcinogenic. For example, phenanthrene acts as a photosensitizer of human skin, and it can even initiate a tumor. [4] Similarly, naphthalene binds strongly with kidney and liver tissue, potentially increasing the toxicity of naphthalene in the body.

1.1.2 PAH sensing techniques

Trace sensing of PAHs is crucial for studying their environmental impact. Detection of PAHs is difficult due to their low solubility in water, causing them to occur in only trace amounts. For example, phenanthrene has a solubility of 1 mg/L in water. [6] Consequently, highly sensitive techniques for PAH detection have been developed by researchers. Fluorescence or mass spectrometry, preceded by chromatographic separation, have proven to be efficient for PAH detection in water samples.

High-performance liquid chromatography (HPLC) integrated with fluorescence spectroscopy has been used to detect PAHs in water with a detection limit of 0.5 microgram/L. [7] Solid-phase extraction can enhance PAH uptake, thus improving the sensitivity of the method. An in-tube solid phase microextraction (SPME) with the

HPLC-fluorescence technique uses polydimethylsiloxane (PDMS) as a sorbent layer to attract PAHs. [8] Another technique involves molecularly imprinted polyurethanes as the capture layer, yielding an enrichment factor of 10^7 and enabling trace detection of PAHs by fluorescence. [9] Using mass spectrometry rather than fluorescence can bring the detection limit down to ng/L, when combined with solid-phase extraction. [10]

1.2 Current advances in SERS detection of PAHs

In contrast to the methods described in section 1.1.2, surface enhanced Raman scattering (SERS) is fast and near-real-time responsive. SERS has vast applications in environmental analysis, [11] pharmaceutical research, [12] chemical science, [13, 14] archaeological analysis, [15] food quality determination, [16] explosive detection, [17] and forensic science, [18]. Naturally, it has also been applied to the detection of PAHs.

A superhydrophobic substrate facilitates the nonpolar PAH adsorption, which ultimately enhances the SERS response. [19–22] A Au nanoparticle (NP)-based superhydrophobic substrate achieved 10^{-8} M detection of pyrene. [23] In addition, other types of PAHs and their derivatives were also detected. Due to the superhydrophobicity of this substrate, oil-water separation was achieved, enhancing PAH separation and detection.

Magnetic-metal hybrid materials are one of the class of the multicomponent SERS substrates that have been employed for PAH sensing using SERS. [24, 25] 16 PAHs were detected with high enhancement factors using Fe_3O_4-Au magnetic-metal nanohybrids. [6] This SERS substrate enabled qualitative detection of different PAHs in a real world sample (river water).

Metal functionalization has been used to enhance the adsorption of nonpolar PAHs on the metal. [26,27] An earlier report achieved a limit of detection (LOD) of 10^{-10} M

for pyrene using a Ag/graphene hybrid material. [28] Hexadecyl trimethyl ammonium bromide (CTAB) micelles functionalized with reduced graphene oxide-Ag NPs shows notable sensitivity towards PAH detection. [29]

1.3 Raman spectroscopy

1.3.1 Origin and fundamentals of Raman spectroscopy

Photons, after incidence on a molecule (or more generally, substance), can scatter elastically or inelastically. Raman scattering is inelastic, in contrast to Rayleigh scattering, which is elastic. [30,31] The Raman effect is named for Dr. C. V. Raman, who observed a frequency shift in scattered photons from a molecule.

Figure 1.1 describes this scattering process. An incident photon with an energy of $h\nu$ excites the molecule to a virtual state or a non-stationary state. The molecule can return to the same initial state resulting in a scattered photon with the same energy $h\nu$ (Rayleigh scattering). If the excited molecule returns to a state that is higher in energy than the original state, then the scattered photon has energy less than the incident photon ($h\nu$-$h\nu'$). The shift in frequency of the scattered photon is known as the Stokes shift. Conversely, if the excited molecule relaxes back to a state lower in energy than the starting state, then the scattered photon will have energy higher than the incident photon ($h\nu$+$h\nu'$). This shift is designated as an anti-Stokes shift, and has lower intensity due to the excitation of the molecule from a less populated, excited vibrational state.

The intensity (I) of the scattered light for a Raman mode depends on the dipole moment (μ) [32]

$$I \propto \mu^2 \tag{1.1}$$

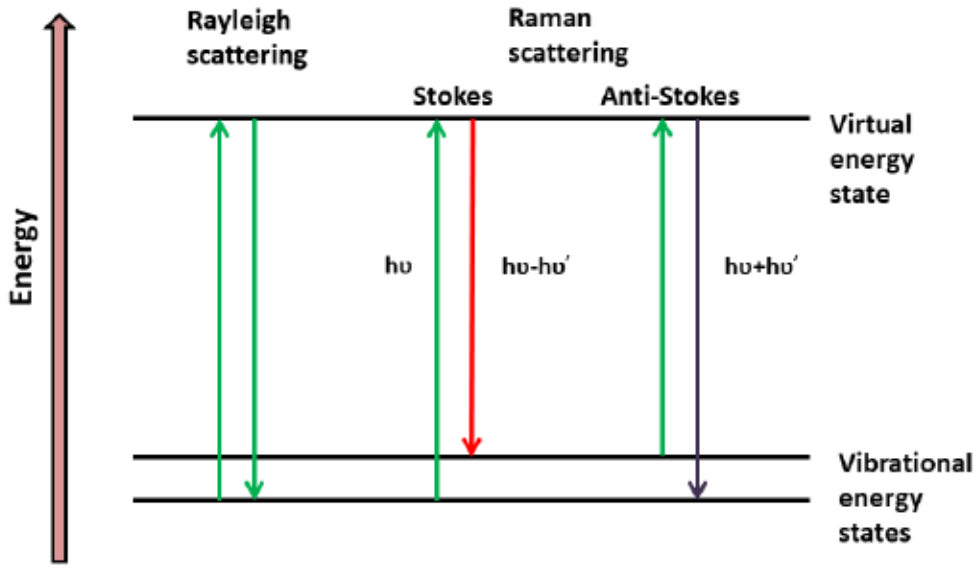

Figure 1.1: Elastic Rayleigh scattering and inelastic Raman scattering.

The dipole moment depends on the incident electromagnetic field (E) and the polarizability (α) of the molecule as

$$\mu = \mu_o + \alpha E \tag{1.2}$$

where μ_o is the permanent dipole of the molecule (zero for nonpolar molecules). Combining equations 1.1 and 1.2 yields

$$I \propto \alpha^2 \cdot E^2 \tag{1.3}$$

In other words, the intensity I of a Raman mode is proportional to the square of the incident field E, and the square of the polarizability α. The enhancement discussed in the next section (1.4) tackles both increasing α and increasing E.

Conventional Raman spectroscopy generates very low signal, as it is a scattering method. In addition, Raman spectra has low signal-to-noise ratio. [33] The discovery of surface enhanced Raman scattering (SERS) enabled the measurement of Raman spectra of analytes at trace concentrations, opening doors for applications in sensing.

[34] The SERS method is explained in the following section.

1.4 Surface enhanced Raman scattering

SERS was first observed by the Raman enhancement of pyridine on an electrochemically roughened silver surface. [35] This discovery introduced a powerful sensitive and selective tool for trace detection. [36]

We can relate the SERS intensity I_{SERS} to the normal Raman intensity I_R by the enhancement factor, EF

$$I_{SERS} = I_R \cdot \mathrm{EF} \tag{1.4}$$

Empirically, the enhancement factor is defined as [37]

$$\mathrm{EF} = \frac{\mathrm{I}_{SERS}}{\mathrm{C}_{SERS}} \times \frac{\mathrm{C}_{Normal}}{\mathrm{I}_{Normal}} \tag{1.5}$$

I_{SERS} and I_{Normal} are the intensities of the surface enhanced Raman mode and the normal Raman mode, respectively. C_{SERS} and C_{Normal} are the concentrations of the analyte in the SERS and normal Raman measurements, respectively. This analytical EF includes contributions from additional surface sites available in the (usually) rougher SERS substrate compared to a SERS-inactive substrate. A surface area corrected EF (EF^*) will measure the contributors to enhancement independent of surface area changes, allowing for direct comparison between candidate substrates when tuning material properties.

The enhancement factor can be presented in two parts, arising from the electromagnetic (EM) and the chemical (CM) enhancement mechanisms [34]

$$I = I_R \cdot (\mathrm{EF}_{EM}) \cdot (\mathrm{EF}_{CM}) \tag{1.6}$$

Electromagnetic enhancement relies on the surface plasmon electromagnetic field generated by metal nanoparticles (NPs), among other materials. In the electromagnetic model, the enhancement of the Raman intensity occurs twice, [38, 39] from the coupling of the local plasmonic field with both the incident field (E_i) and scattered field (E_s). This coupling of fields gives rise to an electromagnetic enhancement factor of [34, 40]

$$\mathrm{EF}_{EM} = E_i^2 \times E_s^2 \tag{1.7}$$

Therefore, the SERS enhancement is proportional to the fourth power of the electromagnetic field. The surface plasmon can increase E by a factor of 10, leading to a Raman enhancement of 10^4.

Chemical enhancement results from the adsorption of the analyte on the metal surface, which can lead to charge transfer, geometric changes, or other changes to the electronic structure of the adsorbate, all of which affect the polarizability of the molecule $\alpha_{molecule}$. [41] The enhanced polarizability of the molecule, α_{SERS}, can be quite a bit larger, with an EF_{CM} of [34]

$$\mathrm{EF}_{CM} = \frac{\alpha_{SERS}^2}{\alpha_{molecule}^2} \tag{1.8}$$

The chemical enhancement can contribute to an enhancement factor by 10^2 or more. [42]

1.4.1 Electromagnetic enhancement: Surface plasmons

"Surface plasmon" refers to the collective oscillation of conductive surface electrons of a metal. [43] This surface plasmon oscillation propagates along the metal-dielectric interface. When incident photons couple with surface plasmons, an excitation occurs known as a surface plasmon polariton (SPP). When the plasmonic material is in the

form of a particle which is smaller than the wavelength of the incident radiation, localized surface plasmon resonance (LSPR) occurs, resulting in the formation of an intense and confined plasmonic field. LSPR is sensitive to the dielectric environment and is also influenced by the geometry factor of the particle.

The surface plasmon property of a metal can be described with the classical electrodynamics approach by solving Maxwell's equations. The Drude–Sommerfeld model is presented here to describe the metal optical property in terms of the collection of unbound electrons and a stationary positive charge center (a rigid ionic lattice). [44] In this mathematical description, an oscillating electron has an equation of motion under the influence of an applied electric field described by

$$m_e \frac{d^2\vec{r}}{dt^2} + m_e \Gamma \frac{d\vec{r}}{dt} = e_c \vec{E}_0 e^{-i\omega t} \tag{1.9}$$

where m_e is the effective electron mass, e_c is one electron charge, and $\vec{r}$ is the displacement of the electron from the equilibrium position as a function of time t. Γ is the damping constant, which is proportional to the Fermi velocity of the electron. E_0 is the magnitude of the applied electric field and ω is the frequency of the field.

Macroscopic polarization (P) can be defined as

$$\varepsilon = 1 + \frac{|P|}{\varepsilon_0 |E|} \tag{1.10}$$

where ε is the dielectric constant of the metal. Using $\vec{r} = r_0 e^{-i\omega t}$ (r_0 is position of the electron at the equilibrium position), one can obtain the Drude dielectric $\varepsilon_{\text{Drude}}$ of the metal:

$$\varepsilon_{\text{Drude}}(\omega) = 1 - \frac{\omega_p^2}{\omega^2 + i\Gamma\omega} \tag{1.11}$$

where ω_p is plasmon frequency of the metal, which is the resonance frequency of

electrons. This plasmon frequency can be expressed as

$$\omega_p = \sqrt{\frac{ne_c^2}{m_e \varepsilon_0}} \tag{1.12}$$

Here, n is electron density. This relationship has been used extensively to calculate the approximate dielectric constant of the metal within the approximation of free electrons on the metal surface. This model is quite accurate in the infrared region but can lead to problems in the visible region as it neglects interband transitions. Interband transitions occurs when high energy photons excite electrons to a higher energy state. These transitions are more important in the visible region, where the incident light has a higher energy than the band transition energy.

In the classical picture, this interband transition can be described as exciting the oscillation of bound electrons. Hence a spring constant k, describing the potential barrier of the bound electron, appears in the modified version of the Drude–Sommerfeld equation, known as the Lorentz–Drude model [45]

$$m_b \frac{d^2\vec{r}}{dt^2} + m_b \gamma \frac{d\vec{r}}{dt} + k\vec{r} = e_c \vec{E}_0 e^{-i\omega t} \tag{1.13}$$

where γ is the damping constant in Lorentz–Drude model and m_b is the effective mass of the bound electron. With this modification of the Drude model, one can arrive at an expression for the dielectric constant of the metal,

$$\varepsilon_{\text{interband}}(\omega) = 1 + \frac{\omega_p^2}{(\omega_0^2 - \omega^2) - i\gamma\omega} \tag{1.14}$$

This equation is known to be a better approximation for calculating the dielectric function of metals (Ag, Au) in the visible region. [46]

The plasmon electromagnetic Raman enhancement can be calculated by deriving

the electromagnetic field generated outside the metal sphere. [47] In this case, ε_0 is the dielectric constant of the surrounding medium and ε_i is that of the metal. By solving Maxwell's equations, one can arrive at the electromagnetic field outside the metal sphere E_P, *i.e.* the plasmonic field, due to the incident field E_0

$$E_{\mathrm{P}} = E_0\hat{z} - \alpha_i E_0\Big[\frac{\hat{z}}{r^3} - \frac{3z}{r^5}(z\hat{z} + x\hat{x} + y\hat{y})\Big] \tag{1.15}$$

In this equation x, y, and z are Cartesian coordinates, r is radial distance and $\hat{x}$, $\hat{y}$, and $\hat{z}$ are unit vectors along Cartesian axes. The polarizability of the metal sphere can be expressed as

$$\alpha_i = ga^3 \tag{1.16}$$

where α_i is the polarizability of the metal and a is the radius of the metal sphere. g is defined as

$$g = \frac{\varepsilon_i - \varepsilon_0}{\varepsilon_i + 2\varepsilon_0} \tag{1.17}$$

where ε_i can be quantified theoretically from the Drude model (equation 1.14).

The Raman intensity from a molecule adsorbed on the plasmonic metal sphere can be evaluated as the absolute square of the plasmonic field (E_P^2, see equation 1.3), which can be expressed as

$$E_P^2 = E_0^2\Big[|1 - |g|^2| + 3\cos^2\theta(2\Re(g) + |g|^2)\Big] \tag{1.18}$$

Here, θ is the angle between the incident field vector and the vector describing the position of the molecule on the surface of the plasmonic material (the surface normal). For large $|g|$, this equation reduces to

$$E_P^2 = E_0^2|g|^2(1 + 3\cos^2\theta) \tag{1.19}$$

Therefore, at 0° and 180° angles, the highest enhancement occurs. For the anti-Stokes peaks,

$$\mathrm{EF} = \frac{{E_P}^2 {E'_P}^2}{E_0^4} \tag{1.20}$$

where E'_P refers to the scattered radiation, to differentiate it from the plasmonic field E_P and the incident field E_0. When $|g| \gg 1$ one can insert equation 1.19 into 1.20, yielding

$$\mathrm{EF} = \propto |g|^2 |g'|^2 \tag{1.21}$$

g' is defined by the dielectric constant for the scattered radiation. Hence, the more general expression for the enhancement factor is EF$\propto g^4$, which is commonly known as E^4 enhancement, as defined earlier in equation 1.7.

1.4.2 Distance dependence of enhancement

The dependence of the Raman intensity on the distance between the analyte and the metal surface is complex. [41] However, with a more general version one can correlate the distance between the metal sphere and the analyte with I_{SERS}. Typically, the highest plasmonic enhancement of the Raman mode of the analyte can be achieved in the close vicinity of the metal surface, where the analyte molecule experiences the intense surface plasmonic electromagnetic field. For a metal sphere with radius r, the field enhancement decays as r^{-3}, from the solution to the Laplace equation. [41] (The supplementary information in Ref. 48 derives the solution in great detail.) Since the SERS intensity goes as E^4 (see equation 1.7), it decays with a factor of r^{-12}. Figure 1.2 depicts the EF as a function of the distance from a plasmonic (gold) structure (tip). [49]

The enhancement factor can be dramatically increased by the generation of plasmonic hotspots. Plasmonic hotspots are intense plasmonic fields at the junction of

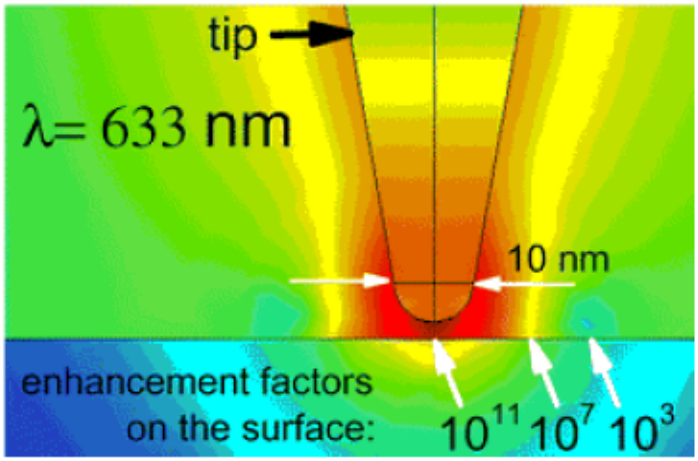

Figure 1.2: Enhancement factor variation with distance from a gold tip. Reproduced "in part" from Ref. 49 with permission of the PCCP Owner Societies.

two or more metal nanoparticles (NPs). [50] Single molecule detection is possible when that molecule is in a hotspot (nanoparticle junction), as demonstrated with haemoglobin (Hb) [51] and rhodamine 6G measured with Ag NPs. [52]

1.4.3 Adsorption effects

Since the enhancement of the Raman signal from an analyte by the metal plasmonic field is distance dependent, a strong adsorption interaction between the analyte and the metal surface is crucial in order to experience maximum near-field enhancement, as the signal from molecules in solution above the surface is negligible (see section 1.4.2). Furthermore, the adsorption of the analyte can also impact the polarizability of the analyte, thus impacting the Raman intensity (equation 1.8). These adsorption effects are explained in this section.

Adsorption interactions are generally classified as: [53]

Chemisorption: This involves chemical bonding interaction between an analyte and the surface of the SERS substrate.

Physisorption : Electrostatic force or other physical forces between the analyte and

the surface of the SERS substrate, no chemical bonds are involved in this interaction.

Surface coverage of analytes determines the SERS signal. SERS intensity is directly proportional to the number of *adsorbed* molecules in the scattering volume, which is not necessarily linear with the number of molecules in the scattering volume (*i.e.* the molecule concentration). Above monolayer coverage, the molecule in the second layer will not experience the same surface plasmonic field as the adsorbed molecule in the first layer. Therefore, above the monolayer coverage, the SERS signal is no longer directly proportional to the number of adsorbed molecules. [54]

The number of adsorbed molecules depends on the number of available sites for adsorption, which in the simplest case is related to surface area. [54] An early work showed Langmuir adsorption behaviour for physisorbed monolayers of different analyte organic molecules on glassy carbon. The intensity *vs.* solution concentration plot shows the typical Langmuir isotherm, similar to a logarithmic relation between solution concentration and SERS intensity. [55] A typical Langmuir isotherm can be represented as

$$n_e = \frac{n_m \cdot K_L \cdot C_e}{1 + K_L \cdot C_e} \tag{1.22}$$

where n_e is the amount of analyte molecules adsorbed at equilibrium ($\mathrm{mg{\cdot}g^{-1}}$), n_m is the maximum amount of analyte molecule to form a monolayer on the adsorbent, ($\mathrm{mg{\cdot}g^{-1}}$), K_L is the Langmuir isotherm constant ($\mathrm{L{\cdot}mg^{-1}}$), and C_e is the analyte concentration ($\mathrm{mg{\cdot}L^{-1}}$).

In many cases, however, the adsorption interactions are not so simple. One deviation from the simple Langmuir isotherm comes from surface roughness. Non-uniform surface roughness generates different types of spaces for the analyte molecule, which affects the possible molecular orientations upon adsorption. Therefore, if we consider two possible orientations of a molecule, a simple Langmuir isotherm transforms to a modified Langmuir profile. [56] Figure 1.3 shows three models: single Langmuir, dual-

site Langmuir (adsorption on different type of sites) and dual arrangement Langmuir (different orientations at the same type of site).

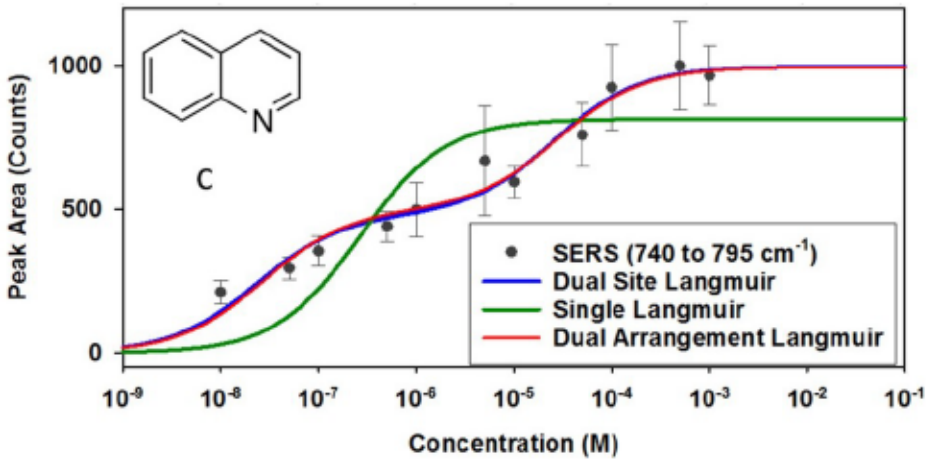

Figure 1.3: Different Langmuir isotherm depending on the molecular orientation on the rough surface. Adapted with permission from Ref. 56. Copyright (2016) American Chemical Society.

Another source of deviation from simple Langmuir adsorption involves intermolecular interactions between adsorbates, which are excluded in the Langmuir model. [57] The adsorption of molecules with strong intermolecular interactions would be better described with the Brunauer–Emmett–Teller (BET) model, as observed for quinacridones on a Ag surface. [58] The relationship between solution concentration and adsorption concentration (and hence SERS intensity) is not as simple as in equation 1.22, as the BET model does not level off like the Langmuir model.

A further effect of analyte adsorption, beyond impacting the relationship between solution concentration and number of adsorbates, is the impact of adsorption on the electronic structure of the analyte. In the case of chemisorption, the molecule-surface binding interaction changes the polarizability (α) of the associated bonds in the molecule and consequently shifts the vibrational frequency. [36] For example, 1,4-benzenedithiol shows different SERS response depending on how it interacts with the SERS substrate. [59] Figure 1.4 depicts two types of substrates: a rough Au

surface and a sandwich structure between Au spheres and a Au surface. In the first case, the molecule is attached through one thiol group and, in the second case, both thiol groups. Due to these different adsorption effects, there is a marked shift in the vibrational frequencies of the ring breathing, C=C stretching, and C–S stretching modes.

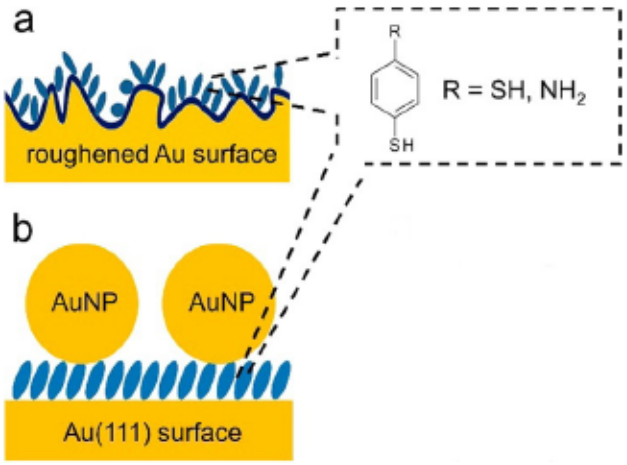

Figure 1.4: (a) Molecule on a rough Au surface and (b) molecule in a sandwich between Au spheres and a planar Au surface. Adapted with permission from Ref. 59. Copyright (2016) American Chemical Society.

1.4.4 Charge-transfer enhancement mechanism

In resonance Raman enhancement the laser excitation wavelength is in resonance with the molecular electronic excitation (HOMO→LUMO), as shown in the Figure 1.5. [36] This electronic excitation changes the polarizability ($\alpha_{molecule}$) of the molecule, thus changing its Raman scattering cross section. Even without resonance Raman, using SERS can also change the polarizability of the molecule through charge transfer (CT) between the SERS substrate and the molecule. This CT is shown at right in Figure 1.5. Hence CT also leads to perturbation or modification of $\alpha_{molecule}$, which ultimately impacts the intensity of the Raman mode (see equation 1.8). [34]

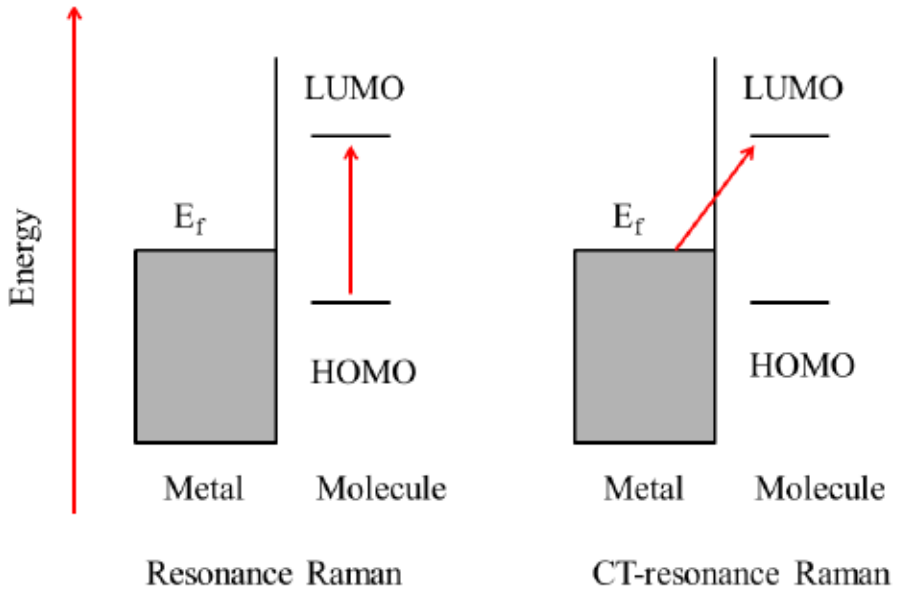

Figure 1.5: Electronic excitation mediated chemical enhancement in SERS: HOMO–LUMO electronic transition from the Raman laser (left), and metal to molecule electron transfer from excitation by the Raman laser (right).

Substrate-analyte charge transfer modifies the electron density of the analyte molecule, which also changes the energy of the vibrational mode, resulting in shifted Raman peaks. [60, 61] Charge transfer can also lead to the appearance of additional or new Raman peaks when CT results in symmetry breaking. [62, 63]

1.5 SERS mechanistic studies

1.5.1 Theoretical approaches

Both classical and quantum approaches have been applied to determine the enhancement mechanisms of SERS. The classical electrodynamics approach is mainly employed for the simulation of electromagnetic enhancement, whereas quantum mechanical calculations can provide insight on chemical enhancement mechanisms.

Classical electrodynamics approach

Solving Maxwell's equations for electrodynamics is the classical way to determine the surface plasmon electric field. Some good implementations include finite-difference-time-domain (FDTD) solutions, [64] the boundary element method (BEM), [65] and the discrete dipole approximation (DDA). [66] The FDTD simulation is observed to be the best among them due to its excellent performance for large scale calculations with great accuracy. [67] Therefore, the FDTD formalism and its application to SERS mechanism studies are explained here. [67, 68]

The FDTD simulation solves electromagnetic equations in the time domain with a finite-difference calculation. Maxwell's equation for a electric field can be written as

$$\nabla \times \vec{H} = \varepsilon \frac{\delta \vec{E}}{\delta t} \tag{1.23}$$

or

$$\frac{\delta \vec{E}}{\delta t} = \frac{1}{\varepsilon} \nabla \times \vec{H} \tag{1.24}$$

where $\vec{H}$ is the magnetic field, $\vec{E}$ is the electric field, and ε is the dielectric constant of the material.

The FDTD treats equation 1.24 with finite time steps:

$$\frac{\vec{E}(t + \Delta t) - \vec{E}(t))}{\Delta t} = \frac{1}{\varepsilon} \nabla \times [\vec{H}(t + \frac{\Delta t}{2})] \tag{1.25}$$

A simulation of the response of a nanoscale plasmonic material of a particular shape with dielectric ε yields the plasmonic electric field $\vec{E}$. The location of maximum intensity E corresponds to a hotspot. For example, silver nanospheres on a flat gold surface were modeled using the FDTD simulation. [69] The maximum electric field intensity was found to be at the junction of the two metals.

FDTD simulations can run on systems of realistic size, facilitating direct predictive or confirmatory links to experimental data. In the example above, [69] the model system consisted of Ag spheres (20–80 nm) 1 nm apart on a flat Au surface (400 nm×400 nm) that was 150 nm thick, a system which mimics closely the SERS substrate used experimentally. The enhancement factors (EFs) can be calculated from equation 1.20, since the simulation yields the magnitude of the plasmonic electric field (E_P) generated by an incident field (*i.e.* from the Raman laser) of magnitude E_0. As a result, the authors were able to check the EFs with several different excitation wavelengths and confirm a match between simulation and experiment.

Even more complex systems can be simulated, as seen in another recent study of the effect of the semiconductor's dielectric constant on the SERS response from a metal-semiconductor hybrid material. [70] FDTD simulations illustrate the generation of the high intensity plasmonic electric field in the case of Ag spheres on a Ge surface (Ag/Ge) as compared to Ag spheres on a Si surface (Ag/Si) (see Figure 1.6), which is consistent with experimental SERS measurements on these substrates.

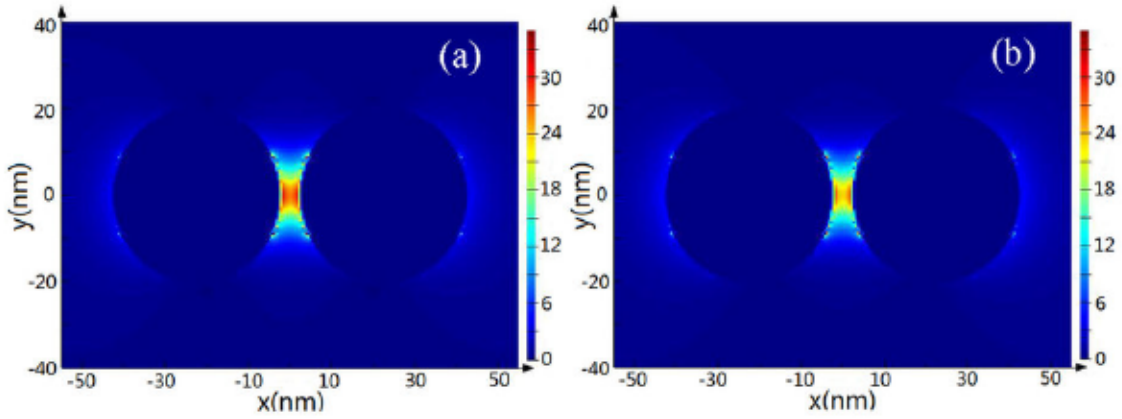

Figure 1.6: The electric field distribution in (a) Ag/Ge and (b) Ag/Si. Ag/Ge shows a more intense plasmonic field at the junction. This figure from Ref. 70 is reproduced under the CC BY-NC-ND 3.0 license.

Quantum mechanical calculations

Several experimental and quantum simulation studies have been performed to investigate chemical contributions. [71, 72] The electronic structure calculation of the molecule-metal system provides information on the binding behavior of the molecule to the metal and the impact on the polarizability. This simulation also offers insight on the electronic excitation of the metal-molecule system, which governs the enhancement of the Raman cross section.

Quantum mechanical calculations provide tools to explore beyond the electromagnetic contributions to SERS enhancement. [42] In the classical electrodynamics model, the adsorbed molecule is treated as a point dipole; hence, the polarizability dependence of Raman activity (see equation 1.3) is completely ignored. The quantum mechanical model offers a more detailed description of the enhancement of the adsorbed molecule on the metal, calculating Raman intensities (I) from

$$I \propto \left| \frac{\delta \alpha_{molecule}}{\delta q} \right|^2 \tag{1.26}$$

$\alpha_{molecule}$ is the polarizability of the molecule and q is the coordinate set for a given mode of the molecule. Based on the definition of Raman intensity I from equation 1.26, it follows that the Raman intensity must be zero when there is no polarizability change upon changing the molecular coordinates.

A number of chemical enhancement mechanisms have been evaluated using quantum chemical calculations, yielding a detailed understanding of the sources of enhancement. [73–76] An example demonstrating that detail involves a TDDFT study of pyridine on a Ag cluster. [77] Two types of Ag-pyridine orientations were modeled, and the polarizability change was calculated for each. It was observed that the highest Raman enhancement can be achieved by the metal surface–pyridine interaction

relative to the metal vertex–pyridine complex. The polarizability change (and hence the Raman enhancement) is found to be a result of charge transfer between Ag and Py.

A hybrid quantum-classical approach has been used to describe the SERS mechanism of pyridine on a surface of a Ag sphere, explicitly. [78] The electromagnetic enhancement is modeled using Mie theory, and then chemical enhancements (both adsorption and CT effect) were calculated with time-dependent density functional theory (TDDFT). These two models were then combined to develop an overall metal–molecule system, which distinguishes EM and CM. This approach was demonstrated with a pyridine-Ag system. [78] This hybrid simulation method was also applied to benzene-Ag and [79] *para*-nitrothiophenol-Ag [80] systems to determine laser frequency dependence of Raman enhancement.

1.5.2 Experimental approaches

Optical absorption spectroscopy

Optical absorption of the plasmonic nanoparticles offers insight into the plasmonic field. Since the plasmonic electromagnetic enhancement is the primary enhancement mechanism, the magnitude of the plasmonic electromagnetic field generation is crucial to achieving high enhancement. [41] Thus, the Raman excitation wavelength should be comparable with the plasmonic absorption wavelength for high enhancement of Raman signals.

One should be able to improve enhancement, therefore, by matching the laser excitation wavelength and the plasmon peak. Normally, noble metals, such as Au and Ag, have their plasmonic absorption near the 400 nm region. However, as per the earlier discussion (section 1.4.1), this plasmonic absorption can be tuned with

varying shape, size, or dielectric environments. [43] A plasmonic absorption study of a SERS substrate can indicate which wavelength of the Raman laser will yield maximum enhancement. A recent example of this strategy is seen in gold nanoring SERS substrates, where the SERS signal is higher for the excitation wavelength, which coincides with the plasmonic absorption maximum. [81]

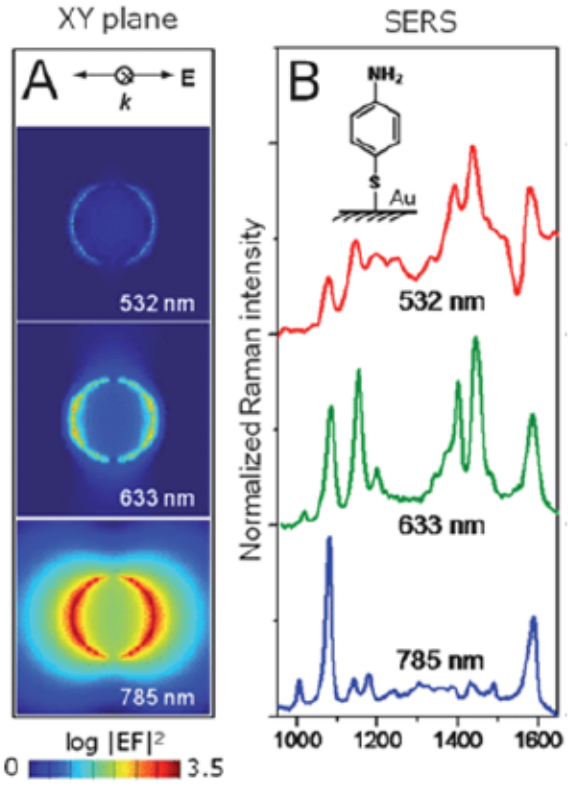

Figure 1.7: Wavelength dependent SERS activity. The 785 nm laser delivers the highest Raman enhancement because it matches the plasmon absorption maximum of the SERS substrate. Reproduced "in part" from Ref. 81 with permission of The Royal Society of Chemistry.

Conversely, the substrate plasmon absorption can be tuned to match a desired excitation wavelength. For example, changing the size of the pits in gold pyramid arrays tunes the localized plasmon absorption in order to complement the Raman laser wavelength. [82] Plasmon tuning for nanoparticles typically involves changing

their size. [83, 84]

However, the relation between the plasmon wavelength and the Raman laser wavelength for plasmonic enhancement is more complex. [41] For example, if the energy gap between plasmon absorption and excitation source matches the energy of a Raman mode, that can also boost the SERS signal. [85] This process is not to be confused with Resonance Raman, where the Raman laser wavelength matches an electronic excitation in the molecule of interest. In resonance Raman, no plasmonic field is present.

Optical absorption spectroscopy can also demonstrate where the enhancement mechanism is not controlled by the plasmonic field intensity. Matching the Raman laser wavelength to the plasmon absorption maximum is not a requirement for SERS activity when chemical (as opposed to electromagnetic) enhancement plays a significant role. [81, 86]

Electron microscopy

While imaging, cathodoluminescence (CL), [89] it can also produce a spatially resolved plasmon map describing different modes of plasmonic field and intensity. The plasmon map is also very important in understanding hotspot generation and plasmonic enhancement, as simulated in the theoretical FDTD calculations described in section 1.5.1.

In CL, the electron bombardment causes electronic excitation in the sample, including plasmon excitation in the so-called "low-loss" region (0-100 eV) of the CL spectrum. After the relaxation of excited electrons, the emitted photons are detected to produce the CL spectrum. These emitted photons yield spatially and spectrally resolved plasmon maps for plasmonic materials. [90, 91]

In a study of Au nanodecahedra, [87] the authors found excellent agreement be-

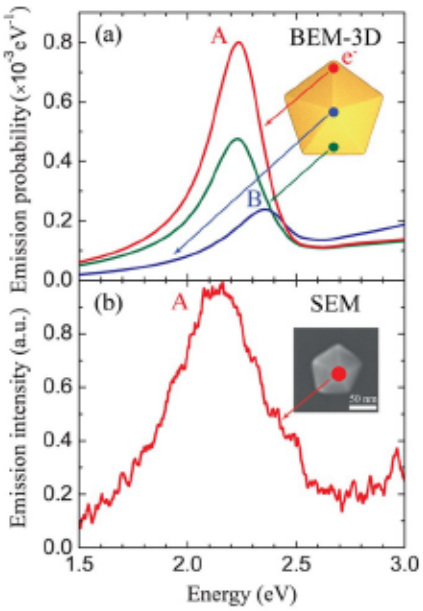

Figure 1.8: The consistency of theoretical (BEM) and experimental (CL, labelled as "SEM") plasmon modes. Adapted with permission from Ref. 87. Copyright (2015) American Chemical Society.

tween theoretical and experimental results. The gold nanodecahedron particle was excited by the electrons, and CL emission spectra showed similar features as the theoretical calculations (using the boundary element method). Although both azimuthal and polar modes were calculated, experimentally only the azimuthal mode was resolved (Figure 1.8). Electron-energy-loss spectroscopy (EELS) can also map plasmonic activity, addressing modes which cannot be resolved by CL. EELS is an electron spectroscopic technique, which can probe both radiative losses and energy transfers (inelastical), and thus resolves more plasmon modes. Losquin et al. [88] measured plasmon modes of a gold nanoprism by EELS and CL. Dipolar plasmon modes were resolved by both techniques (Figure 1.9). Higher order plasmon modes were not resolved by CL, but through EELS these were successfully observed.

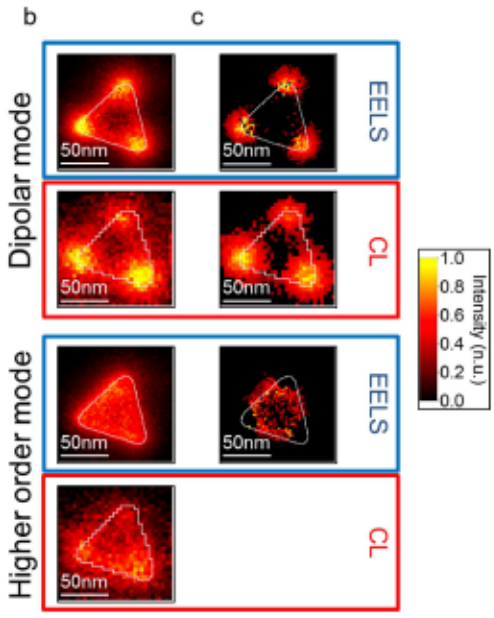

Figure 1.9: Higher order plasmon modes have been mapped with EELS, but CL failed to resolve. Adapted with permission from Ref. 88. Copyright (2015) American Chemical Society.

Scanning probe microscopy

Surface architecture plays a crucial role in SERS due to the reasons described in Section 1.4. A substrate with a rough surface is always a good candidate for the SERS sensing because of the potential for hotspot generation. Additionally, surface electronic properties have a significant impact on SERS activity. [92] Both the surface morphology and the electrical effects are important for studying SERS mechanisms.

Scanning probe microscopy (SPM) is a versatile technique for measuring surface morphology and electrical properties. [93, 94] The instrument scans a tip across a sample, building up an image using data from a series of adjacent line scans. When mapping surface topography, tip-sample van der Waals interactions (short range interactions) tend to govern the tip movement. In contact mode, the SPM tip interacts with the sample surface directly, and the movement of the tip is tracked by the reflection of a laser from the tip to a detector. Tapping mode imaging involves tip-sample

interactions over a much shorter time scale, where tip oscillation damping is tracked by the laser reflection on the detector.

Kelvin probe force microscopy (KPFM) and electrical force microscopy (EFM) can measure both surface morphology and electrical properties. [95, 96] Surface work function can be determined by KPFM, while surface charge can be measured by EFM. In both cases, an initial line scan determines the topography, while a rescan of that line at some distance from the sample measures the (longer-range) electrical forces. There are no published applications of KPFM or EFM to study SERS mechanisms. This thesis demonstrates the utility of these techniques in investigating SERS mechanisms by detailed surface characterizations.

Several research investigations have been devoted to determining the relationship between surface topographical features and the SERS response. One of the earliest and most notable studies on the effect of a rough surface on plasmon activity using SPM studied Ag films. [97] The plasmonic absorption and EFs of the films changed with different thicknesses of evaporated Ag. SPM images showed that different thicknesses of evaporated Ag yielded different particle sizes, demonstrating particle size dependent plasmonic absorption tuning. Another demonstration of morphology-controlled SERS comes from a comparison between a rough and a smooth Ag thin films, [98] where the rough surface exhibited a significantly higher SERS activity (Figure 1.10).

A recent article, which uses SPM data and FDTD simulation to explore the electromagnetic field generation, is worth mentioning. [99] The 3D surface morphology of different Ag films (smooth and rough) were imaged using SPM. By importing the surface topography (coordinates) into the FDTD geometry, the simulation mapped the plasmonic field for the various surfaces, showing that the rough surface generated the highest electromagnetic field.

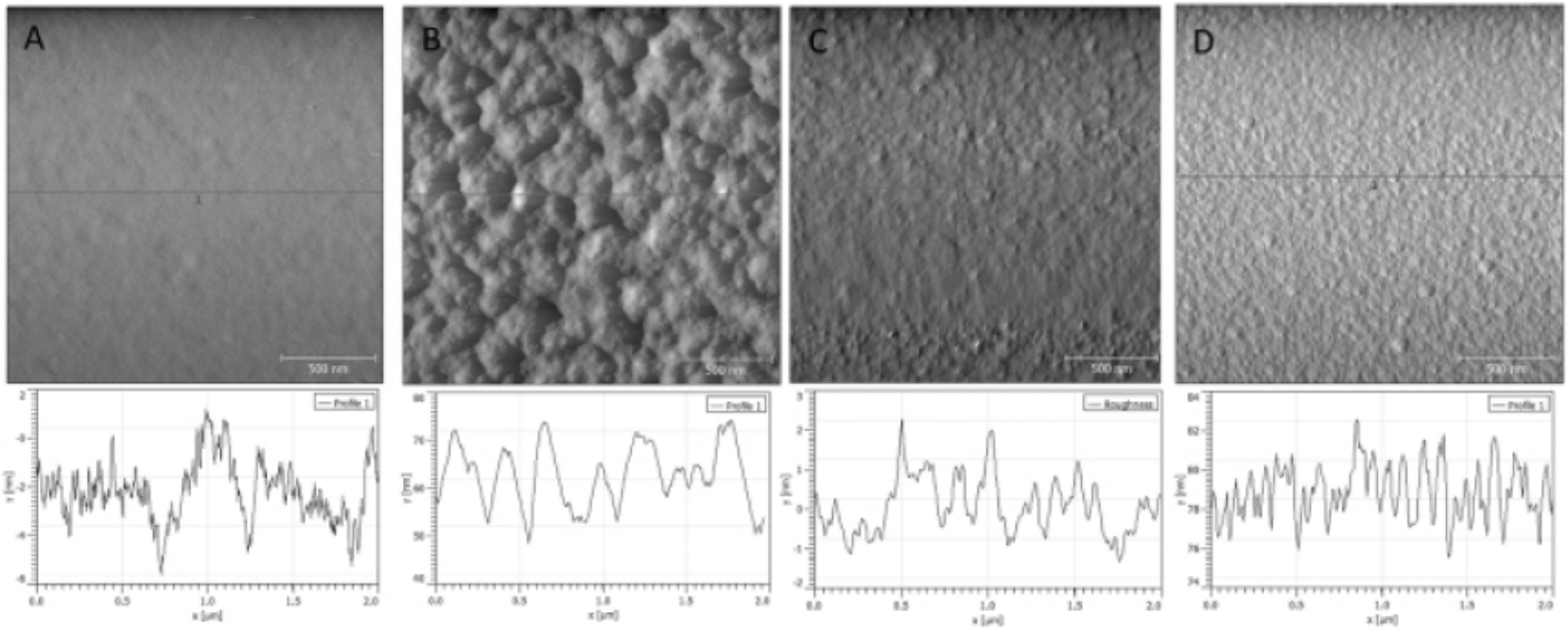

Figure 1.10: SPM images of different silver surfaces. [98]

1.6 SERS substrate fabrication

In this section, different synthetic approaches of SERS substrates are illustrated. Noble metal nanoparticles are of particular interest due to their unique plasmonic properties. Since the surface plasmon enhancement is a surface phenomena, the surface morphology of the SERS substrate has a major impact on the SERS activity. Generally, increased surface roughness is one of the most important requirements for a highly efficient SERS substrate. A rough metallic surface not only generates plasmonic hotspots, but can also increase available adsorption sites for the analyte. To control roughness, these films are often made of nanoparticles of given sizes and shapes.

1.6.1 Chemical synthesis

Gold or silver nanoparticles (NPs) can be synthesized by the reduction of metal salts, generally $AgNO_3$ and AgCl for Ag colloidal NP synthesis and $HAuCl_4$ for Au NPs. [100–103] Both organic and inorganic reducing agents are used for NP formation, with sodium citrate and sodium borohydride being the most common. [104] In most cases, the nanoparticle size is controlled by the addition of a capping agent. The capping agent acts as a stabilizer for individual metal nanoparticles, preventing agglomeration from forming larger particles through electrostatic interactions. [105]

Capping agents can also impact NP shape, forming spheres, nanowires, nanotubes, nanodisks, etc. [106, 107] One of the most recent examples involves the formation of Ag nanoprisms using a biopolymer (protein) as a stabilizing agent, where the amount of biopolymer chain controls the morphology of the Ag NPs. [108] These Ag nanoprisms show high SERS efficiency towards 4-mercapto benzoic acid detection with an enhancement factor of 2.8×10^6.

Addition of multiple stabilizing agents compared to only one stabilizing agent can have drastic effects on nanoparticle shape. [109] Using cetyltrimethylammonium bromide (CTAB) as the stabilizing agent yields spherical shaped Au NPs. A mixture of CTAB and sodium oleate stabilizing agents produces compass-like gold nanoparticles, which after self-assembly, generate a highly ordered periodic array. The compass-like Au NPs have an EF of 4.4×10^6, much higher than that of spherical NPs (EF of 8×10^4).

1.6.2 Nanofabrication

Electron-beam lithography

Electron-beam (e-beam) lithography etches the desired nanoscale features into a substrate by removing material with the high energy and focused beam. Using e-beam lithography, one can design a substrate with a wide range of array geometries and spacings composed of a variety of nanoscale features. [110] Recent examples emphasizing that variety include cone-shaped, [111] bowtie-shaped, [112] and triangle-shaped [113] metallic arrays. The control over shape, size and spacing – particularly the nanoscale spacing possible with an e-beam – allows for the optimization of hotspot generation. [110]

Nanosphere lithography

Nanosphere lithography (NSL) is a simpler way to fabricate highly ordered metal nanoparticle arrays that does not require the specialized equipment or laboratories used for e-beam lithography [41, 114] but is highly reproducible and can also generate nanoscale interparticle spacing. First, micron or sub-micron sized spheres are deposited on a solid support, creating a hexagonal close-packed array of nanospheres

as the sphere carrier evaporates. Metal is then deposited on the drop cast spheres using physical vapor deposition, electron-beam deposition, or pulsed laser deposition with thickness ranges from nm to μm. The nanosphere mask is then removed by sonication or with appropriate solvent, leaving behind an array of triangle-shaped metal nanoparticles formed between the spheres. Particle shape and size can be tuned by the size of the nanosphere, the thickness of the metal film, or metal film treatment (post deposition) such as thermal annealing. [115, 116]

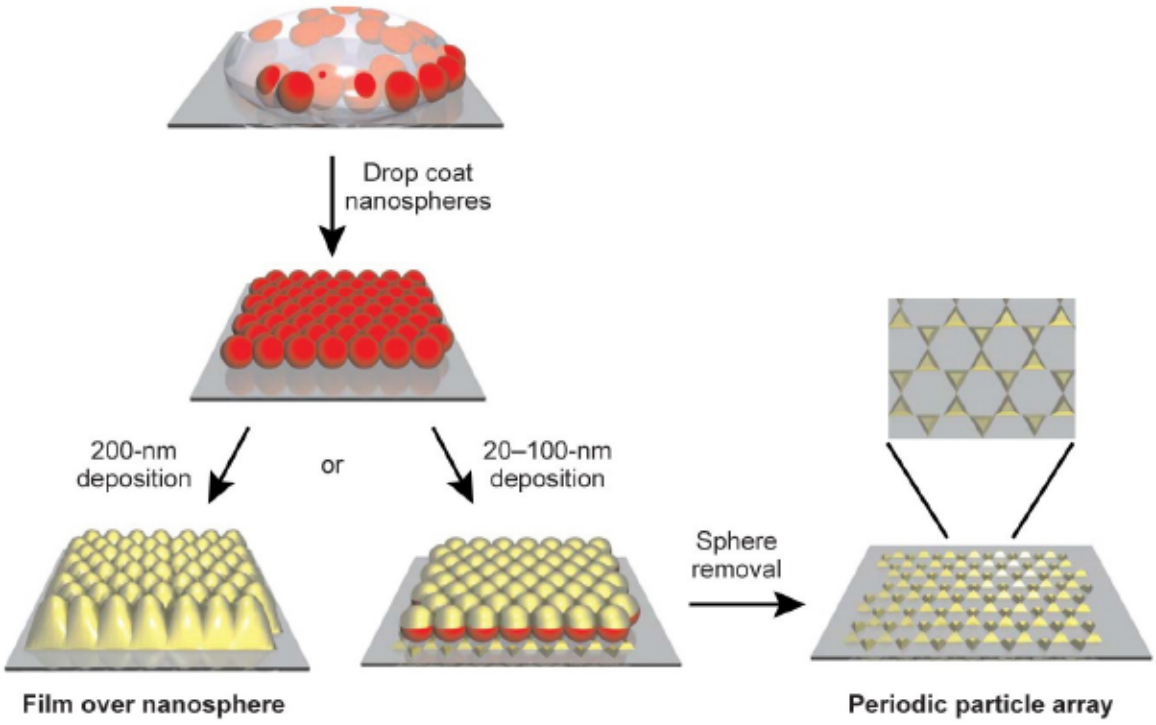

Figure 1.11: Steps involved in nanosphere lithography (NSL) to produce highly ordered NP arrays. [41]

In an interesting inversion of the process, metal "nanovoids" (concave hemispheres) can also be fabricated with NSL, producing intense electromagnetic hotspots at the ridge between the voids. [117] The process begins with deposition of Al on polystyrene (PS) spheres on poly(methyl methacrylate) (PMMA). The Al is covered with a polyimide sheet. The substrate is inverted, and the PMMA and PS are dissolved with

THF. The resulting Al nanovoids are supported on polyimide, which is insoluble in THF. This fabrication yields a highly efficient and reproducible SERS substrate.

1.7 Multicomponent SERS substrates

1.7.1 Metal-semiconductor substrates

Metal-semiconductor hybrid materials are garnering much attention due to their tunable electronic (and hence optical) properties. [118] In the field of plasmonics, semiconductors serve as a suitable dielectric environment to manipulate the plasmonic response of the metal. [70] A semiconductor also affects the surface morphology of the metal layer and hence the generation of surface hotspots. [119] A metal film deposited on a polycrystalline semiconductor film may then adopt the rough surface morphology of the underlying semiconductor. [120] Therefore, this rougher metal surface generates intense plasmonic hotspots as a result of the overlapping of the electromagnetic field at the junction of metal particles. Just as the metal nanoparticles can be synthesized with different shapes, so too can the semiconductor crystallites, whether forming nanorods, nanoflower, and many more. [121]

A semiconductor layer also plays an important role in the generation of a partial surface charge on the metal. [119] Noble metals (Ag, Au) often have higher Fermi levels compared to metal oxide semiconductors (ZnO, TiO_2), resulting in electron transfer from the metal to the semiconductor in order to reach the Fermi level equilibrium. Thus, the metal surface possesses a positively charged surface, and an electron-rich analyte molecule adsorbs through an electrostatic interaction, as observed for PAHs. [122, 123] This enhanced adsorption impacts SERS response, as described in section 1.4.3.

1.7.2 Bimetallic substrates

Bimetallic nanostructures and their applications in SERS is an emerging field of nanoplasmonic research. [124] Au-Ag, Ag-Pd, and many more bimetallic combinations have been observed to be efficient SERS substrates. [125–127] One key feature of bimetallic nanostructures is the generation of a partial surface charge after Fermi level equilibrium between the metals. [92] Due to the higher Fermi level of Ag than that of Au, there is electron transfer from Ag to Au in the Au-Ag bimetallic system, which results in a Ag surface with a partial positive charge and a Au surface with a partial negative surface charge. This surface charge formation facilitates the adsorption of the analyte through an electrostatic interaction. Furthermore, the surface charge density tunes the plasmonic energy. A negative surface charge density shifts the plasmon to a higher wavelength, while a positive surface charge leads to a blue shift of the plasmon absorption. [128, 129]

1.8 Summary

This thesis is mainly devoted to the mechanistic study of PAH sensing by surface enhanced Raman scattering. As mentioned in this introduction, the study of the enhancement mechanism is crucial for understanding the activity of the SERS substrate towards a given analyte. Different hybrid (metal-semiconductor, bimetallic, metal-insulator) materials were fabricated and their SERS performance towards the detection of phenanthrene and pyrene (PAH analytes) were investigated.

The types of ZnO used in this thesis differ in crystal shape as well as in defects and impurities. These defects and impurities are beneficial for semiconductor-driven SERS enhancement [130] and are summarized in Table 1.1. The different types of ZnO are achieved by varying the sol-gel synthesis parameters, which are listed in Table 1.2.

Table 1.1: Crystal shapes and defects of the different types of ZnO used in this thesis, by chapter.

Chapter	Shape	Crystalline domain size (nm) (002)	Defects and impurities
2	Rod	22.87	O deficiency, $Zn(OH)_2$
3	Hexagonal pyramid	26.49	$Zn(OH)_2$
5	Triangular	7.01	Zn vacancies, $Zn(OH)_2$

Table 1.2: Different ZnO synthesis parameters used in this thesis, specifying the mole ratio of [Zn] to [OH] in the starting materials, additives, reaction times and temperatures, and settling times.

Chapter	[Zn]:[OH]	Additive	Reaction temp.	Reaction time	Settling time
2	0.05:1.50		35°C	30 mins	6 hours
3	0.05:1.50		40°C	1 hour	Overnight
5	0.10:0.56	thiourea	40°C	35 mins	2 hours

In this thesis, the enhancement mechanisms for a range of SERS substrates were studied by different experimental techniques, some of which have not been applied before to the investigation of SERS mechanisms. By identifying the key factors in enhancement for each type of SERS substrate, I produced highly sensitive SERS substrates for detection of an organic PAH analyte molecule. A brief chapter summary follows.

1.8.1 Chapter 2: Surface Potential and Morphological Mapping to Investigate Analyte Adsorption Effects on Surface Enhanced Raman Scattering (SERS)

This chapter explains the Au thickness dependent SERS performance of a Au/ZnO substrate. Electron transfer at the metal-semiconductor interface leads to surface positive charge formation on Au, detected from changes in the work function. A substrate of 35 nm of Au on ZnO achieves ppb detection of phenanthrene by balancing

the competitive effects of surface charge and roughness, both of which can lead to plasmonic enhancement.

1.8.2 Chapter 3: Thermal Annealing: A Three-fold Approach to Improving Surface Enhanced Raman Scattering (SERS) Activity of Metal-semiconductor Substrate

Thermal treatment of ZnO prior to Au deposition leads to a significant improvement of SERS activity in the Au-ZnO SERS substrates studied in this chapter. Thermal annealing tunes the surface hydrophobicity, roughness, and electronic structure of the multicomponent substrate. The optimized combination of these three factors leads to an EF of 10^5 for phenanthrene detection in water solution.

1.8.3 Chapter 4: SERS Detection Using Metal-insulator Multilayers: Effect of Insulator on Plasmonic Enhancement

An insulating co-layer with the plasmonic metal can enhance the metal's plasmonic field and, as a whole, improve the SERS activity. The key to this improvement is the suppression of plasmon loss by the insulating layer. This multilayered polymer-metal substrate displays ppb detection of phenanthrene in aqueous solution.

1.8.4 Chapter 5: Effect of ZnO Defects on SERS Activity of Au/ZnO Hybrid Films

In this Au-ZnO nanohybrid, unlike the one in Chapter 2, Au possesses a negative surface charge from reverse charge transfer from ZnO to Au, due to the different preparation of ZnO producing defect-rich crystallites. The metal layer changes the

crystal and electronic properties of the ZnO, with that change depending on the thickness of the Au layer. The changing electronic structure of the ZnO results in different EFs. This introduces a new mode by which metal layers can impact SERS activity.

1.8.5 Chapter 6: Direct Evidence of Surface Charge Controlled SERS Activity in a Bilayer Metal Film by EFM

For the bimetallic substrates studied in Chapter 6, the high SERS activity arises from enhanced analyte adsorption. The positive surface charge on a metal can attract π electron rich PAHs. Electrostatic force microscopy (EFM) directly measures the surface charge, explaining the link to the corresponding enhancement factors for detecting pyrene.

1.8.6 Chapter 7: Kelvin Probe Force Microscopy to Probe Metal–molecule Interactions: A Comparative SERS Sensing of Phenanthrene and Pyrene

Chapter 7 presents the effect of the metal-molecule interaction on the SERS response. A higher enhancement of pyrene on Au compared to phenanthrene is ascribed to the differing strengths of the metal-molecule interactions. KPFM measurement indicates changes in work function that links to the strength of the metal-molecule interactions.

Bibliography

[1] Jamson Masih, Amit Masih, Aditi Kulshrestha, Raj Singhvi, and Ajay Taneja. Characteristics of polycyclic aromatic hydrocarbons in indoor and outdoor at-

mosphere in the North central part of India. *J. Hazard. Mater.*, 177(1–3):190, 2010.

[2] Hussein I. Abdel-Shafy and Mona S.M. Mansour. A review on polycyclic aromatic hydrocarbons: Source, environmental impact, effect on human health and remediation. *Egypt. J. Pet.*, 25(1):107, 2016.

[3] Immaculada Tolosa, Josep M. Bayona, and Joan Albaigés. Aliphatic and Polycyclic Aromatic Hydrocarbons and Sulfur/Oxygen Derivatives in Northwestern Mediterranean Sediments: Spatial and Temporal Variability, Fluxes, and Budgets. *Environ. Sci. Technol.*, 30(8):2495, 1996.

[4] Sudip K Samanta, Om V Singh, and Rakesh K Jain. Polycyclic aromatic hydrocarbons: environmental pollution and bioremediation. *Trends Biotechnol.*, 20(6):243, 2002.

[5] G. Mastrangelo, E. Fadda, and V. Marzia. Polycyclic aromatic hydrocarbons and cancer in man. *Environ Health Perspect*, 104(11):1166, 1996.

[6] Jingjing Du, Jianwei Xu, Zhenli Sun, and Chuanyong Jing. Au nanoparticles grafted on Fe_3O_4 as effective SERS substrates for label-free detection of the 16 EPA priority polycyclic aromatic hydrocarbons. *Anal. Chim. Acta*, 915:81, 2016.

[7] H. G. Kicinski, S. Adamek, and A. Kettrup. Trace enrichment and HPLC analysis of polycyclic aromatic hydrocarbons in environmental samples, using solid phase extraction in connection with UV/VIS diode-array and fluorescence detection. *Chromatographia*, 28(3):203, 1989.

[8] H. Bagheri and A. Salemi. Coupling of a Modified In-Tube Solid Phase Microextraction Technique with High Performance Liquid Chromatography-

Fluorescence Detection for the Ultra-Trace Determination of Polycyclic Aromatic Hydrocarbons in Water Samples. *Chromatographia*, 59(7):501, 2004.

[9] Franz L. Dickert, Matthias Tortschanoff, Wolf E. Bulst, and Gerhard Fischerauer. Molecularly Imprinted Sensor Layers for the Detection of Polycyclic Aromatic Hydrocarbons in Water. *Anal. Chem.*, 71(20):4559, 1999.

[10] Elena Martinez, Meritxell Gros, Sílvia Lacorte, and Damià Barceló. Simplified procedures for the analysis of polycyclic aromatic hydrocarbons in water, sediments and mussels. *J. Chromatogr. A*, 1047(2):181, 2004.

[11] Jumin Hao, Mei-Juan Han, Songman Han, Xiaoguang Meng, Tsan-Liang Su, and Qingwu K. Wang. SERS detection of arsenic in water: A review. *J. Environ. Sci.*, 36:152, 2015.

[12] Wei Zhang, Xueyuan Bai, Yingping Wang, Bing Zhao, Yu Zhao, Wei Hou, Yinping Jin, and Daqing Zhao. SERS study of different configurations of pharmaceutical and natural product molecules ginsenoside Rg3 under the interaction with human serum albumin on simple self-assembled substrate. *Spectrochim. Acta, Part A*, 117:210, 2014.

[13] Wei Xie, Bernd Walkenfort, and Sebastian Schlücker. Label-Free SERS Monitoring of Chemical Reactions Catalyzed by Small Gold Nanoparticles Using 3D Plasmonic Superstructures. *J. Am. Chem. Soc.*, 135(5):1657, 2013.

[14] Bhavya Sharma, Renee R. Frontiera, Anne-Isabelle Henry, Emilie Ringe, and Richard P. Van Duyne. SERS: Materials, applications, and the future. *Mater. Today*, 15(1–2):16, 2012.

[15] Danilo Bersani, Claudia Conti, Pavel Matousek, Federica Pozzi, and Peter Vandenabeele. Methodological evolutions of Raman spectroscopy in art and archaeology. *Anal. Methods*, 8:8395, 2016.

[16] Jing Yang, Gregory L. Rorrer, and Alan X. Wang. Bioenabled SERS substrates for food safety and drinking water monitoring. *Proc. SPIE*, 9488:948808, 2015.

[17] Alison Chou, Esa Jaatinen, Ricardas Buividas, Gediminas Seniutinas, Saulius Juodkazis, Emad L. Izake, and Peter M. Fredericks. SERS substrate for detection of explosives. *Nanoscale*, 4:7419, 2012.

[18] Samantha Boyd, Massimo F. Bertino, Dexian Ye, Lauren S. White, and Sarah J. Seashols. Highly Sensitive Detection of Blood by Surface Enhanced Raman Scattering,. *J. Forensic Sci.*, 58(3):753, 2013.

[19] Hai-Xin Gu, Kai Hu, Da-Wei Li, and Yi-Tao Long. SERS detection of polycyclic aromatic hydrocarbons using a bare gold nanoparticles coupled film system. *Analyst*, 141:4359, 2016.

[20] Lixiao Jing, Yu-e Shi, Jingcheng Cui, Xiaoli Zhang, and Jinhua Zhan. Hydrophobic gold nanostructures via electrochemical deposition for sensitive SERS detection of persistent toxic substances. *RSC Adv.*, 5:13443, 2015.

[21] Xuan Wang, Weimin Hao, Han Zhang, Yingcheng Pan, Yan Kang, Xiaofang Zhang, Mingqiang Zou, Peijin Tong, and Yiping Du. Analysis of polycyclic aromatic hydrocarbons in water with gold nanoparticles decorated hydrophobic porous polymer as surface-enhanced Raman spectroscopy substrate. *Spectrochim. Acta, Part A*, 139(Supplement C):214, 2015.

[22] Olivier Péron, Emmanuel Rinnert, Michel Lehaitre, Philippe Crassous, and Chantal Compère. Detection of polycyclic aromatic hydrocarbon (PAH) com-

pounds in artificial sea-water using surface-enhanced Raman scattering (SERS). *Talanta*, 79(2):199, 2009.

[23] Hongyue Zhao, Jing Jin, Weijun Tian, Ran Li, Zhi Yu, Wei Song, Qian Cong, Bing Zhao, and Yukihiro Ozaki. Three-dimensional superhydrophobic surface-enhanced Raman spectroscopy substrate for sensitive detection of pollutants in real environments. *J. Mater. Chem. A*, 3:4330, 2015.

[24] Dan Song, Rong Yang, Chongwen Wang, Rui Xiao, and Feng Long. Reusable nanosilver-coated magnetic particles for ultrasensitive SERS-based detection of malachite green in water samples. *Sci. Rep.*, 6:22870, 2016.

[25] Jingjing Du and Chuanyong Jing. Preparation of Thiol Modified Fe3O4@Ag Magnetic SERS Probe for PAHs Detection and Identification. *J. Phys. Chem. C*, 115(36):17829, 2011.

[26] Juan He, Fujian Xu, Zhuo Chen, Xiandeng Hou, Qin Liu, and Zhou Long. AuNPs/COFs as a new type of SERS substrate for sensitive recognition of polyaromatic hydrocarbons. *Chem. Commun.*, 53:11044, 2017.

[27] P. Leyton, S. Sanchez-Cortes, J. V. Garcia-Ramos, C. Domingo, M. Campos-Vallette, C. Saitz, and R. E. Clavijo. Selective Molecular Recognition of Polycyclic Aromatic Hydrocarbons (PAHs) on Calix[4]arene-Functionalized Ag Nanoparticles by Surface-Enhanced Raman Scattering. *J. Phys. Chem. B*, 108(45):17484, 2004.

[28] Shaojie Jia, Dan Li, Essy Kouadio Fodjo, Hu Xu, Wei Deng, Yue Wu, and Yuhong Wang. Simultaneous preconcentration and ultrasensitive on-site SERS detection of polycyclic aromatic hydrocarbons in seawater using hexanethiol-modified silver decorated graphene nanomaterials. *Anal. Methods*, 8:7587, 2016.

[29] Meng Jiang, Zhijiang Qian, Xufeng Zhou, Xing Xin, Jinghua Wu, Chao Chen, Gongjun Zhang, Gaojie Xu, and Yuchuan Cheng. CTAB micelles assisted rGO-AgNP hybrids for SERS detection of polycyclic aromatic hydrocarbons. *Phys. Chem. Chem. Phys.*, 17:21158, 2015.

[30] Derek Albert Long and DA Long. *Raman spectroscopy.* McGraw-Hill New York, 1977.

[31] CN Banwell and Elaine M McCash. *Fundamentals of molecular spectroscopy.* Tata McGraw Hill, New Delhi, 1994.

[32] Jeanette G Grasselli and Bernard J Bulkin. *Analytical Raman spectroscopy.* New York : Wiley, 1991.

[33] Shuo Chen, Xiaoqian Lin, Clement Yuen, Saraswathi Padmanabhan, Roger W. Beuerman, and Quan Liu. Recovery of Raman spectra with low signal-to-noise ratio using Wiener estimation. *Opt. Express*, 22(10):12102, 2014.

[34] Eric C. Le Ru and Pablo G. Etchegoin. Quantifying SERS enhancements. *MRS Bull.*, 38(8):631, 2013.

[35] M. Fleischmann, P.J. Hendra, and A.J. McQuillan. Raman spectra of pyridine adsorbed at a silver electrode. *Chem. Phys. Lett.*, 26(2):163, 1974.

[36] Sebastian Schlücker. Surface-Enhanced Raman Spectroscopy: Concepts and Chemical Applications. *Angew. Chem. Int. Ed.*, 53(19):4756, 2014.

[37] E. C. Le Ru, E. Blackie, M. Meyer, and P. G. Etchegoin. Surface Enhanced Raman Scattering Enhancement Factors: A Comprehensive Study. *J. Phys. Chem. C*, 111(37):13794, 2007.

[38] J. G. Bergman, D. S. Chemla, P. F. Liao, A. M. Glass, A. Pinczuk, R. M. Hart, and D. H. Olson. Relationship between surface-enhanced Raman scattering and the dielectric properties of aggregated silver films. *Opt. Lett.*, 6(1):33, 1981.

[39] S.L. McCall, P.M. Platzman, and P.A. Wolff. Surface enhanced Raman scattering. *Phys. Lett. A*, 77(5):381, 1980.

[40] N. M. B. Perney, F. J. García de Abajo, J. J. Baumberg, A. Tang, M. C. Netti, M. D. B. Charlton, and M. E. Zoorob. Tuning localized plasmon cavities for optimized surface-enhanced Raman scattering. *Phys. Rev. B*, 76:035426, 2007.

[41] Paul L. Stiles, Jon A. Dieringer, Nilam C. Shah, and Richard P. Van Duyne. Surface-Enhanced Raman Spectroscopy. *Annu. Rev. Anal. Chem.*, 1(1):601, 2008.

[42] Lasse Jensen, Christine M. Aikens, and George C. Schatz. Electronic structure methods for studying surface-enhanced Raman scattering. *Chem. Soc. Rev.*, 37:1061, 2008.

[43] Katherine A. Willets and Richard P. Van Duyne. Localized Surface Plasmon Resonance Spectroscopy and Sensing. *Annu. Rev. Phys. Chem.*, 58(1):267, 2007.

[44] A F J Levi. *Essential Classical Mechanics for Device Physics.* 2053-2571. Morgan & Claypool Publishers, San Rafael, 2016.

[45] Uwe Kreibig and Michael Vollmer. *Optical properties of metal clusters*, volume 25. Springer, Berlin, 2013.

[46] P. B. Johnson and R. W. Christy. Optical Constants of the Noble Metals. *Phys. Rev. B*, 6:4370, 1972.

[47] George C. Schatz and Richard P. Van Duyne. *Electromagnetic Mechanism of Surface-Enhanced Spectroscopy.* John Wiley & Sons, Ltd, 2006.

[48] Katherine A. Willets and Richard P. Van Duyne. Localized Surface Plasmon Resonance Spectroscopy and Sensing. *Annu. Rev. Phys. Chem.*, 58(1):267, 2007.

[49] P. G. Etchegoin and E. C. Le Ru. A perspective on single molecule SERS: current status and future challenges. *Phys. Chem. Chem. Phys.*, 10:6079, 2008.

[50] Christy L. Haynes and Richard P. Van Duyne. Plasmon-Sampled Surface-Enhanced Raman Excitation Spectroscopy. *J. Phys. Chem. B*, 107(30):7426, 2003.

[51] Hongxing Xu, Erik J. Bjerneld, Mikael Käll, and Lars Börjesson. Spectroscopy of Single Hemoglobin Molecules by Surface Enhanced Raman Scattering. *Phys. Rev. Lett.*, 83:4357, 1999.

[52] Jiang, Ken Bosnick, Mathieu Maillard, and Louis Brus. Single Molecule Raman Spectroscopy at the Junctions of Large Ag Nanocrystals. *J. Phys. Chem. B*, 107(37):9964, 2003.

[53] Eric C. Le Ru and Pablo G. Etchegoin. Chapter 7 - Metallic colloids and other SERS substrates. In Eric C. Le Ru, , and Pablo G. Etchegoin, editors, *Principles of Surface-Enhanced Raman Spectroscopy*, page 367. Elsevier, Amsterdam, 2009.

[54] Eric C. Le Ru and Pablo G. Etchegoin. Chapter 4 - SERS enhancement factors and related topics. In Eric C. Le Ru, , and Pablo G. Etchegoin, editors, *Principles of Surface-Enhanced Raman Spectroscopy*, pages 185 – 264. Elsevier, Amsterdam, 2009.

[55] Mark R. Kagan and Richard L. McCreery. Quantitative Surface Raman Spectroscopy of Physisorbed Monolayers on Glassy Carbon. *Langmuir*, 11(10):4041, 1995.

[56] Ashish Tripathi, Erik D. Emmons, Augustus W. Fountain, Steven D. Christesen, and Jason A. Guicheteau. Identification of Nucleophilic and Electrophilic Binding Sites on Gold Surface-Enhanced Raman Substrates. *J. Phys. Chem. C*, 120(41):23523–23528, 2016.

[57] Ricardo Aroca. *Surface-Enhanced Vibrational Spectroscopy*, chapter Surface-Enhanced Raman Scattering, pages 73–106. John Wiley & Sons, Ltd, Chichester, UK, 2007.

[58] Elena del Puerto, Concepcion Domingo, Jose V. Garcia Ramos, and Santiago Sanchez-Cortes. Adsorption Study and Detection of the High Performance Organic Pigments Quinacridone and 2,9-Dimethylquinacridone on Ag Nanoparticles By Surface-Enhanced Optical Spectroscopy. *Langmuir*, 30(3):753, 2014.

[59] Sho Suzuki, Satoshi Kaneko, Shintaro Fujii, Santiago Marqués-González, Tomoaki Nishino, and Manabu Kiguchi. Effect of the Molecule–Metal Interface on the Surface-Enhanced Raman Scattering of 1,4-Benzenedithiol. *J. Phys. Chem. C*, 120(2):1038, 2016.

[60] A. Alyami, D. Saviello, M. A. P. McAuliffe, A. Mirabile, L. Lewis, and D. Iacopino. Metal nanoinks as chemically stable surface enhanced scattering (SERS) probes for the analysis of blue BIC ballpoint pens. *Phys. Chem. Chem. Phys.*, 19:14652, 2017.

[61] F. Wan, H. Shi, W. Chen, Z. Gu, L. Du, J. Wang, P.; Wang, and Y. Huang. Charge Transfer Effect on Raman and Surface Enhanced Raman Spectroscopy of Furfural Molecules. *Nanomaterials*, 7:210, 2017.

[62] Shan Cong, Yinyin Yuan, Zhigang Chen, Junyu Hou, Mei Yang, Yanli Su, Yongyi Zhang, Liang Li, Qingwen Li, Fengxia Geng, and Zhigang Zhao. Noble metal-comparable SERS enhancement from semiconducting metal oxides by making oxygen vacancies. *Nat. Commun.*, 6:7800, 2015.

[63] Jun Hee Yoon, Jung Shin Park, and Sangwoon Yoon. Time-Dependent and Symmetry-Selective Charge-Transfer Contribution to SERS in Gold Nanoparticle Aggregates. *Langmuir*, 25(21):12475, 2009.

[64] W. M. Saj. FDTD simulations of 2D plasmon waveguide on silver nanorods in hexagonal lattice. *Opt. Express*, 13(13):4818, 2005.

[65] Jiunn-Woei Liaw. Simulation of surface plasmon resonance of metallic nanoparticles by the boundary-element method. *J. Opt. Soc. Am. A*, 23(1):108, 2006.

[66] Xi-bin Xu, Zao Yi, Xi-bo Li, Yu-ying Wang, Xing Geng, Jiang-shan Luo, Bing-chi Luo, You-gen Yi, and Yong-jian Tang. Discrete Dipole Approximation Simulation of the Surface Plasmon Resonance of Core/Shell Nanostructure and the Study of Resonance Cavity Effect. *J. Phys. Chem. C*, 116(45):24046, 2012.

[67] Dror Sarid and William Challener. *Modern introduction to surface plasmons: theory, Mathematica modeling, and applications.* Cambridge University Press, Cambridge, 2010.

[68] Allen Taflove, Ardavan Oskooi, and Steven G Johnson. *Advances in FDTD computational electrodynamics: photonics and nanotechnology.* Artech house, 2013.

[69] Kwan Kim, Jeong-Yong Choi, Hyang Bong Lee, and Kuan Soo Shin. Raman scattering of 4-aminobenzenethiol sandwiched between Ag nanoparticle and macroscopically smooth Au substrate: Effects of size of Ag nanoparticles and the excitation wavelength. *J. Chem. Phys.*, 135(12):124705, 2011.

[70] Tao Wang, Zhaoshun Zhang, Fan Liao, Qian Cai, Yanqing Li, Shuit-Tong Lee, and Mingwang Shao. The Effect of Dielectric Constants on Noble Metal/Semiconductor SERS Enhancement: FDTD Simulation and Experiment Validation of Ag/Ge and Ag/Si Substrates. *Sci. Rep.*, 4:4052, 2014.

[71] Ronald L. Birke, John R. Lombardi, Wissam A. Saidi, and Patrick Norman. Surface-Enhanced Raman Scattering Due to Charge-Transfer Resonances: A Time-Dependent Density Functional Theory Study of Ag_{13}-4-Mercaptopyridine. *J. Phys. Chem. C*, 120(37):20721, 2016.

[72] Liping Liu, Haitao Yang, Xiao Ren, Jin Tang, Yongfeng Li, Xiangqun Zhang, and Zhaohua Cheng. Au-ZnO hybrid nanoparticles exhibiting strong charge-transfer-induced SERS for recyclable SERS-active substrates. *Nanoscale*, 7:5147, 2015.

[73] Maurizio Muniz-Miranda, Francesco Muniz-Miranda, and Alfonso Pedone. Raman and DFT study of methimazole chemisorbed on gold colloidal nanoparticles. *Phys. Chem. Chem. Phys.*, 18:5974, 2016.

[74] Nguyen Thi Thai An, Duy Quang Dao, Pham Cam Nam, Bui The Huy, and Hong Nhung Tran. Surface enhanced Raman scattering of melamine on silver substrate: An experimental and DFT study. *Spectrochim. Acta, Part A*, 169(Supplement C):230, 2016.

[75] Lijun Ji, Yingying Sun, Yunfei Xie, Heya Wang, He Qian, Li Wang, and Weirong Yao. Density functional theory and surface-enhanced Raman spectroscopy studies on endocrine-disrupting chemical, dimethyl phthalate. *Vib. Spectrosc.*, 79(Supplement C):44, 2015.

[76] Federico Latorre, Stephan Kupfer, Thomas Bocklitz, Daniel Kinzel, Steffen Trautmann, Stefanie Grafe, and Volker Deckert. Spatial resolution of tip-enhanced Raman spectroscopy - DFT assessment of the chemical effect. *Nanoscale*, 8:10229, 2016.

[77] Zhao, Lasse Jensen, and George C. Schatz. Pyridine$-Ag_{20}$ Cluster: A Model System for Studying Surface-Enhanced Raman Scattering. *J. Am. Chem. Soc.*, 128(9):2911, 2006.

[78] Jonathan Mullin, Nicholas Valley, Martin G. Blaber, and George C. Schatz. Combined Quantum Mechanics (TDDFT) and Classical Electrodynamics (Mie Theory) Methods for Calculating Surface Enhanced Raman and Hyper-Raman Spectra. *J. Phys. Chem. A*, 116(38):9574, 2012.

[79] Zhongwei Hu, Dhabih V. Chulhai, and Lasse Jensen. Simulating Surface-Enhanced Hyper-Raman Scattering Using Atomistic Electrodynamics-Quantum Mechanical Models. *J. Chem. Theory Comput.*, 12(12):5968, 2016.

[80] Martin Thomas, Stefan Mühlig, Tanja Deckert-Gaudig, Carsten Rockstuhl, Volker Deckert, and Philipp Marquetand. Distinguishing chemical and electromagnetic enhancement in surface-enhanced Raman spectra: The case of para-nitrothiophenol. *J. Raman Spectrosc.*, 44(11):1497, 2013.

[81] Jian Ye, James Andell Hutchison, Hiroshi Uji-i, Johan Hofkens, Liesbet Lagae, Guido Maes, Gustaaf Borghs, and Pol Van Dorpe. Excitation wavelength

dependent surface enhanced Raman scattering of 4-aminothiophenol on gold nanorings. *Nanoscale*, 4:1606, 2012.

[82] N. M. B. Perney, F. J. García de Abajo, J. J. Baumberg, A. Tang, M. C. Netti, M. D. B. Charlton, and M. E. Zoorob. Tuning localized plasmon cavities for optimized surface-enhanced Raman scattering. *Phys. Rev. B*, 76:035426, 2007.

[83] Nicolas M. B. Perney, Jeremy J. Baumberg, Majd E. Zoorob, Martin D. B. Charlton, Sven Mahnkopf, and Caterina M. Netti. Tuning localized plasmons in nanostructured substrates for surface-enhanced Raman scattering. *Opt. Express*, 14(2):847, 2006.

[84] Masahiko Shioi, Kristof Lodewijks, Liesbet Lagae, Tatsuro Kawamura, and Pol Van Dorpe. Tuning plasmonic interaction between gold nanorings and a gold film for surface enhanced Raman scattering. *Appl. Phys. Lett.*, 97(16):163106, 2010.

[85] Marilena Ricci, Elena Platania, Cristiana Lofrumento, Emilio M. Castellucci, and Maurizio Becucci. Resonance Raman Spectra of o-Safranin Dye, Free and Adsorbed on Silver Nanoparticles: Experiment and Density Functional Theory Calculation. *J. Phys. Chem. A*, 120(27):5307, 2016.

[86] Wan-Ing Lin, Mohammad Fardin Gholami, Paul Beyer, Nikolai Severin, Feng Shao, Renato Zenobi, and Jurgen P. Rabe. Strongly enhanced Raman scattering of Cu-phthalocyanine sandwiched between graphene and Au(111). *Chem. Commun.*, 53:724, 2017.

[87] Viktor Myroshnychenko, Jaysen Nelayah, Giorgio Adamo, Nicolas Geuquet, Jessica Rodríguez-Fernández, Isabel Pastoriza-Santos, Kevin F. MacDonald, Luc Henrard, Luis M. Liz-Marzán, Nikolay I. Zheludev, Mathieu Kociak, and

F. Javier García de Abajo. Plasmon Spectroscopy and Imaging of Individual Gold Nanodecahedra: A Combined Optical Microscopy, Cathodoluminescence, and Electron Energy-Loss Spectroscopy Study. *Nano Lett.*, 12(8):4172, 2012.

[88] Arthur Losquin, Luiz F. Zagonel, Viktor Myroshnychenko, Benito Rodríguez-González, Marcel Tencé, Leonardo Scarabelli, Jens Förstner, Luis M. Liz-Marzán, F. Javier García de Abajo, Odile Stéphan, and Mathieu Kociak. Unveiling Nanometer Scale Extinction and Scattering Phenomena through Combined Electron Energy Loss Spectroscopy and Cathodoluminescence Measurements. *Nano Lett.*, 15(2):1229, 2015.

[89] Ben G Yacobi and David Basil Holt. *Cathodoluminescence microscopy of inorganic solids.* Springer, Berlin, 2013.

[90] Mathieu Kociak and Odile Stephan. Mapping plasmons at the nanometer scale in an electron microscope. *Chem. Soc. Rev.*, 43:3865, 2014.

[91] F. J. García de Abajo. Optical excitations in electron microscopy. *Rev. Mod. Phys.*, 82:209, 2010.

[92] Pekka Peljo, José A. Manzanares, and Hubert H. Girault. Contact Potentials, Fermi Level Equilibration, and Surface Charging. *Langmuir*, 32(23):5765, 2016.

[93] Seizo Morita, Franz J Giessibl, Ernst Meyer, and Roland Wiesendanger. *Noncontact atomic force microscopy*, volume 3. Springer, Berlin, 2015.

[94] G. Binnig, C. F. Quate, and Ch. Gerber. Atomic Force Microscope. *Phys. Rev. Lett.*, 56:930, 1986.

[95] Wan-Hsien Lin, Jih-Jen Wu, Mitch M. C. Chou, Yu-Ming Chang, and Masahiro Yoshimura. Charge Transfer in Au Nanoparticle–Nonpolar ZnO Photocatalysts

Illustrated by Surface-Potential-Derived Three-Dimensional Band Diagram. *J. Phys. Chem. C*, 118(34):19814, 2014.

[96] Guicun Qi, Yanlian Yang, Hao Yan, Li Guan, Yibao Li, Xiaohui Qiu, and Chen Wang. Quantifying Surface Charge Density by Using an Electric Force Microscope with a Referential Structure. *J. Phys. Chem. C*, 113(1):204, 2009.

[97] R. P. Van Duyne, J. C. Hulteen, and D. A. Treichel. Atomic force microscopy and surface-enhanced Raman spectroscopy. I. Ag island films and Ag film over polymer nanosphere surfaces supported on glass. *J. Chem. Phys.*, 99(3):2101, 1993.

[98] Changwon Lee, Christopher S. Robertson, An H. Nguyen, Mehmet Kahraman, and Sebastian Wachsmann-Hogiu. Thickness of a metallic film, in addition to its roughness, plays a significant role in SERS activity. *Sci. Rep.*, 5:11644, 2015.

[99] Gerard Macias, Maria Alba, Lluis F. Marsal, and Agustin Mihi. Surface roughness boosts the SERS performance of imprinted plasmonic architectures. *J. Mater. Chem. C*, 4:3970, 2016.

[100] Yi-Cheun Yeh, Brian Creran, and Vincent M. Rotello. Gold nanoparticles: preparation, properties, and applications in bionanotechnology. *Nanoscale*, 4:1871, 2012.

[101] Isabel Pastoriza-Santos and Luis M. Liz-Marzán. Synthesis of Silver Nanoprisms in DMF. *Nano Lett.*, 2(8):903, 2002.

[102] Nguyen Ngoc Long, Le Van Vu, Chu Dinh Kiem, Sai Cong Doanh, Cao Thi Nguyet, Pham Thi Hang, Nguyen Duy Thien, and Luu Manh Quynh. Synthesis and optical properties of colloidal gold nanoparticles. *J. Phys. Conf. Ser.*, 187(1):012026, 2009.

[103] J. Kasthuri, S. Veerapandian, and N. Rajendiran. Biological synthesis of silver and gold nanoparticles using apiin as reducing agent. *Colloids Surf., B*, 68(1):55, 2009.

[104] Hélène Dozol, Guillaume Mériguet, Bernard Ancian, Valérie Cabuil, Haolan Xu, Dayang Wang, and Ali Abou-Hassan. On the Synthesis of Au Nanoparticles Using EDTA as a Reducing Agent. *J. Phys. Chem. C*, 117(40):20958, 2013.

[105] Virender K. Sharma, Ria A. Yngard, and Yekaterina Lin. Silver nanoparticles: Green synthesis and their antimicrobial activities. *Adv. Colloid Interface Sci.*, 145(1):83, 2009.

[106] B. Ajitha, Y. Ashok Kumar Reddy, P. Sreedhara Reddy, Hwan-Jin Jeon, and Chi Won Ahn. Role of capping agents in controlling silver nanoparticles size, antibacterial activity and potential application as optical hydrogen peroxide sensor. *RSC Adv.*, 6:36171, 2016.

[107] S. Vijaya Kumar and S. Ganesan. Preparation and Characterization of Gold Nanoparticles with Different Capping Agents. *Int. J. Green Nanotechnol.*, 3(1):47, 2011.

[108] Xi Geng, Weinan Leng, Nathan A. Carter, Peter J. Vikesland, and Tijana Z. Grove. Protein-aided formation of triangular silver nanoprisms with enhanced SERS performance. *J. Mater. Chem. B*, 4:4182, 2016.

[109] Youju Huang, Liwei Dai, Liping Song, Lei Zhang, Yun Rong, Jiawei Zhang, Zhihong Nie, and Tao Chen. Engineering Gold Nanoparticles in Compass Shape with Broadly Tunable Plasmon Resonances and High-Performance SERS. *ACS Appl. Mater. Interfaces*, 8(41):27949, 2016.

[110] Neval A. Cinel, Semih Cakmakyapan, Serkan Butun, Gulay Ertas, and Ekmel Ozbay. E-Beam lithography designed substrates for surface enhanced Raman spectroscopy. *Photonics Nanostruct. Fundam. Appl.*, 15(Supplement C):109, 2015.

[111] Neval A. Cinel, Serkan Bütün, Gülay Ertaş, and Ekmel Özbay. 'Fairy Chimney'-Shaped Tandem Metamaterials as Double Resonance SERS Substrates. *Small*, 9(4):531, 2013.

[112] Gang Bi, Li Wang, Li Ling, Yukie Yokota, Yoshiaki Nishijima, Kosei Ueno, Hiroaki Misawa, and Jianrong Qiu. Optical properties of gold nano-bowtie structures. *Opt. Commun.*, 294(Supplement C):213, 2013.

[113] Lucia Petti, Rossella Capasso, Massimo Rippa, Marianna Pannico, Pietro La Manna, Gianfranco Peluso, Anna Calarco, Eugenia Bobeico, and Pellegrino Musto. A plasmonic nanostructure fabricated by electron beam lithography as a sensitive and highly homogeneous SERS substrate for bio-sensing applications. *Vib. Spectrosc.*, 82(Supplement C):22 – 30, 2016.

[114] Christy L. Haynes and Richard P. Van Duyne. Nanosphere Lithography: A Versatile Nanofabrication Tool for Studies of Size-Dependent Nanoparticle Optics. *J. Phys. Chem. B*, 105(24):5599, 2001.

[115] Valeria Lotito and Tomaso Zambelli. Self-assembly and nanosphere lithography for large-area plasmonic patterns on graphene. *J. Colloid Interface Sci.*, 447:202, 2015.

[116] C L Cheung, R J Nikolić, C E Reinhardt, and T F Wang. Fabrication of nanopillars by nanosphere lithography. *Nanotechnology*, 17(5):1339, 2006.

[117] Daniel O. Sigle, Elaine Perkins, Jeremy J. Baumberg, and Sumeet Mahajan. Reproducible Deep-UV SERRS on Aluminum Nanovoids. *J. Phys. Chem. Lett.*, 4(9):1449, 2013.

[118] Uri Banin, Yuval Ben-Shahar, and Kathy Vinokurov. Hybrid Semiconductor–Metal Nanoparticles: From Architecture to Function. *Chem. Mater.*, 26(1):97, 2014.

[119] Haibin Tang, Guowen Meng, Qing Huang, Zhuo Zhang, Zhulin Huang, and Chuhong Zhu. Arrays of Cone-Shaped ZnO Nanorods Decorated with Ag Nanoparticles as 3D Surface-Enhanced Raman Scattering Substrates for Rapid Detection of Trace Polychlorinated Biphenyls. *Adv. Funct. Mater.*, 22(1):218, 2012.

[120] Ruibin Jiang, Benxia Li, Caihong Fang, and Jianfang Wang. Metal/Semiconductor Hybrid Nanostructures for Plasmon-Enhanced Applications. *Adv. Mater.*, 26(31):5274, 2014.

[121] Zhuo Wang, Xue feng Qian, Jie Yin, and Zi kang Zhu. Large-Scale Fabrication of Tower-like, Flower-like, and Tube-like ZnO Arrays by a Simple Chemical Solution Route. *Langmuir*, 20(8):3441, 2004.

[122] Shuichi Hashimoto, Sigeru Ikuta, Tsuyoshi Asahi, and Hiroshi Masuhara. Fluorescence Spectroscopic Studies of Anthracene Adsorbed into Zeolites: From the Detection of Cation$-\pi$ Interaction to the Observation of Dimers and Crystals. *Langmuir*, 14(15):4284, 1998.

[123] Dongqiang Zhu, Bruce E. Herbert, Mark A. Schlautman, Elizabeth R. Carraway, and Jin Hur. Cation-pi Bonding: A New Perspective on the Sorption

of Polycyclic Aromatic Hydrocarbons to Mineral Surfaces. *J. Environ. Qual.*, 33(4):1322, 2004.

[124] Mohammad Y. Khaywah, Safi Jradi, Guy Louarn, Yvon Lacroute, Joumana Toufaily, Tayssir Hamieh, and Pierre-M. Adam. Ultrastable, Uniform, Reproducible, and Highly Sensitive Bimetallic Nanoparticles as Reliable Large Scale SERS Substrates. *J. Phys. Chem. C*, 119(46):26091, 2015.

[125] M. Vinod and K.G. Gopchandran. Bimetallic Au–Ag nanochains as SERS substrates. *Curr. Appl. Phys.*, 15(8):857, 2015.

[126] Arumugam Sivanesan, Evelin Witkowska, Witold Adamkiewicz, Lukasz Dziewit, Agnieszka Kaminska, and Jacek Waluk. Nanostructured silver-gold bimetallic SERS substrates for selective identification of bacteria in human blood. *Analyst*, 139:1037, 2014.

[127] Zao Yi, Xiulan Tan, Gao Niu, Xibin Xu, Xibo Li, Xin Ye, Jiangshan Luo, Binchi Luo, Weidong Wu, Yongjian Tang, and Yougen Yi. Facile preparation of dendritic Ag–Pd bimetallic nanostructures on the surface of Cu foil for application as a SERS-substrate. *Appl. Surf. Sci.*, 258(14):5429, 2012.

[128] Jean Lermé. Size Evolution of the Surface Plasmon Resonance Damping in Silver Nanoparticles: Confinement and Dielectric Effects. *J. Phys. Chem. C*, 115(29):14098, 2011.

[129] Jean Lermé, Hatim Baida, Christophe Bonnet, Michel Broyer, Emmanuel Cottancin, Aurélien Crut, Paolo Maioli, Natalia Del Fatti, Fabrice Vallée, and Michel Pellarin. Size Dependence of the Surface Plasmon Resonance Damping in Metal Nanospheres. *J. Phys. Chem. Lett.*, 1(19):2922, 2010.

[130] Shan Cong, Yinyin Yuan, Zhigang Chen, Junyu Hou, Mei Yang, Yanli Su, Yongyi Zhang, Liang Li, Qingwen Li, Fengxia Geng, and Zhigang Zhao. Noble metal-comparable SERS enhancement from semiconducting metal oxides by making oxygen vacancies. *Nat. Commun.*, 6:7800, 2015.

Co-authorship Statement

Abhijit Chatterjee has the major contribution on implementing research plans, fabricating substrates and conducting experiments. In addition, result and discussion section of each chapter including data interpretation and illustrating different SERS mechanism was also done by Abhijit Chatterjee. Prof. Erika Merschrod is a consistent co-author in each manuscript and was invaluable in her contributions. This thesis also has contributions from researchers in the Merschrod group. Here the contribution of co-authors is elaborately described chapter-by-chapter. In the manuscript chapters, "we/our" implies group contribution whereas "I/my" is for work attributable directly to me.

Fabrication of ZnO film and characterizations in Chapter 2 (Surface Potential and Morphological Mapping to Investigate Analyte Adsorption Effects on Surface Enhanced Raman Scattering (SERS)) was completed by Abhijit Chatterjee. Dr. Dmytro Grebennikov contributed by explaining the effect of the surface area on the SERS activity. The KPFM study was performed with the help of David Gale. Liam Whelan offered significant insight on the work function calculation from the KPFM scan.

The following chapter (Thermal Annealing: A Three-fold Approach to Improving Surface Enhanced Raman Scattering (SERS) Activity of Metal-semiconductor Substrate) has contributions from Dr. Dmytro Grebennikov on the understanding of the effect of the substrate roughness on the SERS activity. David Gale assisted with the

substrate synthesis and the annealing treatment. He also assisted on the collection of SEM images.

Dr. Dmytro Grebennikov developed the substrate synthesis plan and Abhijit Chatterjee assisted on the substrate fabrication in Chapter 4 (SERS Detection Using Metal-insulator Multilayers: Effect of Insulator on Plasmonic Enhancement). KPFM scans of Au coated substrates were performed by Liam Whelan. KPFM surface scan of polymer coated spheres and bare spheres were conducted by Abhijit Chatterjee. Raman and UV-Vis spectra were also collected by Abhijit Chatterjee.

Chapter 5 (Effect of ZnO Defects on SERS Activity of Au/ZnO Hybrid Films) was primarily developed by Abhijit Chatterjee. David Gale assisted with performing KPFM scans and Dr. Dmytro Grebennikov was also the collaborator on ZnO synthesis.

Chapter 6, entitled "Direct Evidence of Surface Charge Controlled SERS Activity in a Bilayer Metal Film by EFM" has a major contribution of Dr. Dmytro Grebennikov on substrate fabrication. He also helped to understand the surface charge generation in the bimetallic system. EFM study and the surface electrical property determination was accomplished by Abhijit Chatterjee. SERS experiment and the plasmon absorption measurement were also performed by Abhijit Chatterjee.

Chapter 7 (Kelvin Probe Force Microscopy to Probe Metal–molecule Interactions: A Comparative SERS Sensing of Phenanthrene and Pyrene) was also conducted by Abhijit Chatterjee, which includes substrate synthesis and necessary experiments. In addition, computational Raman calculation of pyrene in the gas phase was performed by Abhijit Chatterjee.

Chapter 2

Surface Potential and Morphological Mapping to Investigate Analyte Adsorption Effects on Surface Enhanced Raman Scattering (SERS)*

2.1 Abstract

I demonstrate the power of Kelvin probe force microscopy (KPFM) in enabling a comprehensive study of enhancement mechanisms of surface enhanced Raman scattering (SERS) through the correlation of surface electrical and topographical effects. Local electric fields generated on Au/ZnO nanohybrid films impact analyte adsorption,

*This chapter is a modified version of "Surface Potential and Morphological Mapping to Investigate Analyte Adsorption Effects on Surface Enhanced Raman Scattering (SERS)", Abhijit Chatterjee, David J. G. Gale, Dmytro Grebennikov, Liam D. Whelan and Erika F. Merschrod S., *Chemical Communications*, 2017,53, 12024-12027

while roughness is linked to hotspot generation. Optimizing the interplay between these two effects yields SERS enhancement factors (EFs) of 10^6, achieving ppb detection of polycyclic aromatic hydrocarbons (PAHs) in water.

2.2 Introduction

Surface enhanced Raman scattering (SERS) is an emerging sensing technique for the trace detection of molecules. [1, 2] In the past decade, multicomponent SERS substrates have gained much attention for their significant SERS response. [3–5] Among the multicomponent substrates, metal/semiconductor hybrid nanostructures show unique SERS activity, [6] expanding the range of potential materials for SERS substrates. A better understanding of the enhancement mechanism would enable the fabrication of highly efficient multicomponent SERS substrates for use in sensors with industrial and environmental applications.

Both theoretical and experimental approaches have been employed to explore enhancement mechanisms of SERS. [7, 8] Of the contributing factors, a higher surface area can facilitate the adsorption of an analyte [9], and a rougher surface can generate plasmonic hot spots to enhance the Raman signal of adsorbed analyte molecules. [10] In addition, the surface charge can dominate the interaction of the analyte with the SERS substrate, thus affecting SERS performance. An electron-rich (or negatively charged) analyte molecule will experience an attractive electrostatic interaction with the positively charged surface of a metal substrate. This interaction increases SERS performance [11] by enhancing the adsorption of the analyte. [12] In this chapter, I examine the influence of the surface charge and the morphology on signal enhancement in metal/semiconductor SERS substrates, and I establish a methodology to study them in a wide range of composite SERS materials.

Charge transfer (CT), an inherent feature of metal/semiconductor hybrids, generates a local electric field as a result of the electron transfer at the metal/semiconductor interface. [5, 13] Depending on the difference between the Fermi energy (E_F) of both components, the direction as well as the magnitude of the electron transfer can switch. Generally, noble metals have higher Fermi energies than those of metal oxide semiconductors (ZnO), depending on the size of the nanoparticles. [14] This leads to electron transfer from the metal to the semiconductor in order to reach Fermi level equilibrium, which produces a partial positive charge on the metal surface. This positive charge is enough to promote the adsorption of even non-polar molecules such as polycyclic aromatic hydrocarbons (PAHs). [15, 16]

Scanning probe microscopy (SPM) can map both topographic and electronic properties of the surface of a material [17, 18] that reveal the mechanism of analyte adsorption. The commonly used height scan, as in atomic force microscopy (AFM), delivers the surface topographic information, enabling surface roughness factor and surface area calculations. [19] The metal-semiconductor-generated local electric field can be investigated using Kelvin probe force microscopy (KPFM), [20] which by design also measures topography, providing both electronic and morphological information in a single scan.

KPFM measures the work function of the sample through the electronic interaction between the tip and the sample surface. [21] The work function, Φ, of an element is defined as the amount of energy required to extract one electron from the surface of the material to the vacuum. Therefore, Φ is higher for a positively charged material than when it is neutral. Consequently, a higher positive surface charge density on the surface makes for a higher Φ, [22] allowing for visualization of charge formation on the sample.

In this report, I discuss SERS mechanisms and identify KPFM as a powerful

technique for their study. I synthesized gold covered rod shaped ZnO metal/semiconductor hybrid nanostructures that have significant sensitivity toward phenanthrene, a serious environmental pollutant. [23] With KPFM, I successfully explain the effect of the surface roughness of the Au/ZnO nanohybrid on its SERS activity. In addition, I also demonstrate the charge transfer process between Au and ZnO and its influence on the Raman enhancement.

2.3 Experimental

Rod shaped ZnO crystals were created using a simple sol-gel technique and deposited on glass slides. [24] Different thicknesses of gold were thermally evaporated on the ZnO thin films. For convenience, the four thicknesses of gold on ZnO are indicated as A45 (45 nm of Au), A35 (35 nm of Au), A25 (25 nm of Au) and A15 (15 nm of Au). The SERS experiment was carried out by exposing the substrates to a 1 ppm aqueous phenanthrene solution for 30 minutes and then rinsing with ultrapure water followed by air drying. Sample preparation details are provided in the Appendix A.1.

2.4 Results and discussion

The field emission scanning electron microscope (FESEM) image in Figure 2.1 highlights the faceted rod shape of the resultant ZnO crystals, and the accompanying XRD data confirm their hexagonal wurtzite structure. [25] It is noteworthy that diffraction peaks of ZnO crystals are shifted to a higher angle. This can be explained by the presence of defects in those crystals, where the width and amount of shift of the diffraction peak indicate the defect density. [26] Raman analysis of the ZnO film also indicates the existence of defects (the appendix, Figure A.2). [27, 28] The peak near 33° 2θ could be due to the existence of a $Zn(OH)_2$ phase. [29]

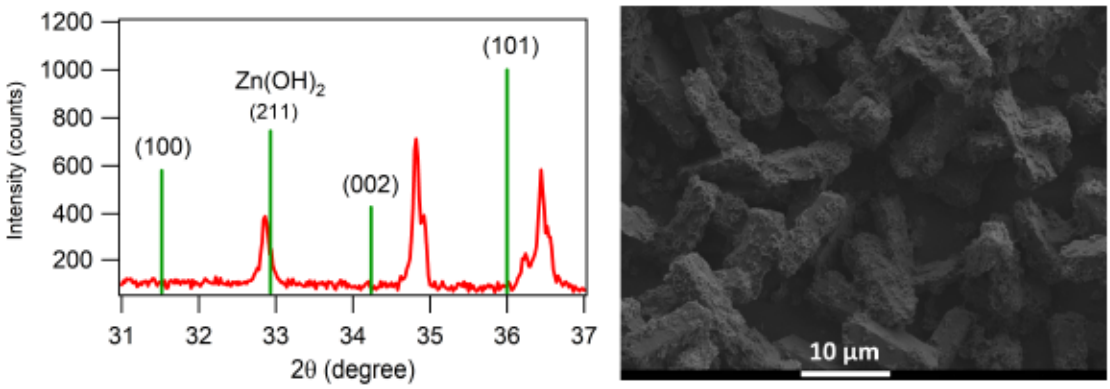

Figure 2.1: The XRD data (left) shows the wurtzite crystal structure of ZnO with $Zn(OH)_2$ contaminants. The FESEM image (right) depicts rod shaped ZnO crystals.

Phenanthrene was successfully detected using Au-covered ZnO films down to 1 ppb (the appendix, Figure A.5). The SERS activity of these films could arise from either component (Au or ZnO) alone, but control experiments demonstrate that the enhancement comes from the interaction between the analyte and the Au surface of the Au/ZnO nanohybrid. The Au film could show plasmonic activity on its own, but the plasmon absorption band turns out to be far from the Raman excitation wavelength (the appendix, Figure A.4), [1] leading to its SERS inactivity (the appendix, Figure A.6). Semiconductor films can show Raman enhancement through semiconductor-analyte charge transfer, [30] which can be increased further by the defects generated by the sol-gel method and seen in the XRD data above (Figure 2.1). However, in our case ZnO alone is SERS inactive (the appendix, Figure A.6).

Au film thickness impacts the SERS activity of the nanohybrid films, with A45 $\approx$ A35 $\approx$ A25 $>$ A15 (Figure 2.2), with the 35 nm Au/ZnO nanohybrid films showing the highest enhancement factor (EF) (Table 2.1). Different thicknesses of Au display different plasmon absorption (the appendix, Figure A.3), but this effect alone does not explain the SERS activity trend of higher Au thicknesses. Therefore, I investigated the consequence of Au thickness changes on other properties of the substrates: surface charge and morphology.

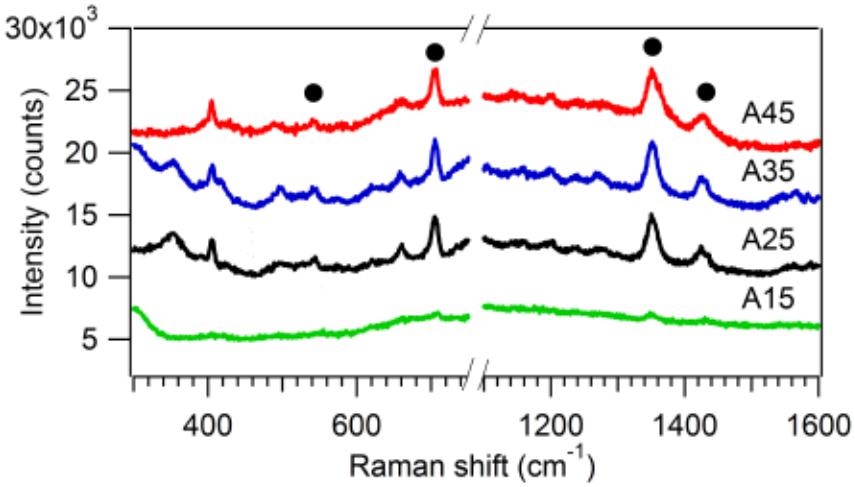

Figure 2.2: A35 (blue) shows the highest SERS activity, which is comparable to that of A45 (red) and A25 (black) and greater than that of A15 (green). Symbols indicate enhanced Raman modes of phenanthrene. Spectra are offset for clarity.

To measure surface morphology and electrical properties, Kelvin probe force microscopy was introduced using a MFP3D (Asylum Research) instrument with a Ti/Pt conductive tip. A key morphological parameter is surface area, since increasing surface area generates more adsorption sites for the analyte. [31] Table 2.1 shows surface area values for a 1×1 μm^2 projected area, where a perfectly flat substrate would show a surface area of 1 μm^2. When I account for changing surface area, by calculating the surface area corrected EF (EF*), the trend in EF with thickness persists. Therefore, the surface area change cannot explain the enhanced SERS activity seen with thicker Au films.

Table 2.1: Surface area, enhancement factor (EF), and surface area corrected enhancement factor (EF*) for different substrates.

Sample tag	Surface area (μm^2)	EF ($\times10^6$)	EF* ($\times10^6$)
A45	1.38 ± 0.29	6.7 ± 0.4	5.1 ± 0.1
A35	1.33 ± 0.17	7.0 ± 0.2	5.4 ± 0.1
A25	1.25 ± 0.21	6.3 ± 0.5	5.0 ± 0.2
A15	1.21 ± 0.12	0.01 ± 0.002	0.008 ± 0.001

The surface area corrected EF (EF*) is calculated by applying a modification to the analytical EF calculation (the appendix equation A.2). [32]

$$EF^* = EF \times \frac{A_{Normal}}{A_{SERS}} \tag{2.1}$$

where A_{Normal} is the surface area of the plain glass slide and A_{SERS} is the surface area of the SERS substrate. The area measured depends on the tip shape; therefore, A_{Normal} was measured each time A_{SERS} was measured. The EF* values in Table 2.1 show that even when the increased surface area is accounted for, the A35 films still show more Raman enhancement than A45 and A25, which in turn show more enhancement than A15. This is where charge transfer and/or hot spot generation must be playing a role.

The ZnO film plays an important role in producing positive charge density on the surface of the Au film, which is then in contact with the analyte. The charge transfer is a consequence of the Fermi level equilibrium at the Au/ZnO interface. Herein, KPFM was used to determine the work function (Φ) of the Au film on ZnO crystals, a measure of the positive surface charge density formation on the metal film. [20]

During a KPFM scan, a Pt coated Ti tip electronically interacts with the sample. The measured contact potential difference (CPD) arises from the difference between Fermi levels of the tip and the sample surface. From the CPD value and the work function of the Pt tip, Φ(tip), I can determine the work function of the sample, Φ(sample)

$$CPD = \Phi(tip) - \Phi(sample) \tag{2.2}$$

The work function of the tip was calibrated using highly oriented pyrolytic graphite (HOPG) with a known work function (4.6 eV). [20]

KPFM scans were performed on A15, A25, A35 and A45, as well as on the cor-

responding 15 nm, 25 nm, 35 nm and 45 nm thick Au films deposited directly on a glass slide. Figure 2.3 shows the concurrent contact potential and morphology scans from one measurement of the A35 substrate. The resultant average work functions, Φ, are gathered in Table 2.2.

The work function of a film can vary because of film thickness and/or the surface charge of the film. [33, 34] Table 2.2 shows that the work function of Au on ZnO is always higher than that of Au on only glass for every Au thickness measured. Therefore, the Au surface charge must be changed by the ZnO. Glass has minimal electronic interaction with the deposited film; therefore we chose glass as a base substrate. [35, 36] Furthermore, an increase in work function can only arise from a more positive surface.

In the Au/ZnO system, the surface charge on Au is generated by the Fermi level equilibration at the Au/ZnO interface. The positive surface charge on Au implies that the electron transfer occurs from Au to ZnO to reach the electronic equilibrium at their interface. This observation is consistent with a previous study which also showed electron transfer from Au to ZnO. [20]

In changing Au film thickness, it was found that the thicker the Au film on ZnO, the higher the work function. Others have also observed an increase in electron transfer between Au and ZnO with thicker Au films. [20] Thus A45, the sample with the thickest Au film, also has the largest gain in work function relative to a plain Au film, and hence the highest surface charge.

Although A45 has the highest surface charge, and therefore the highest affinity for the analyte, its SERS performance is comparable to that of A25 and A35, films with lower surface charge. Therefore, there must be another factor at play in the Raman enhancement mechanism. This other factor is the roughness of the surface, whose increase can generate plasmonic hot spots. The roughness factor (R_q) has a

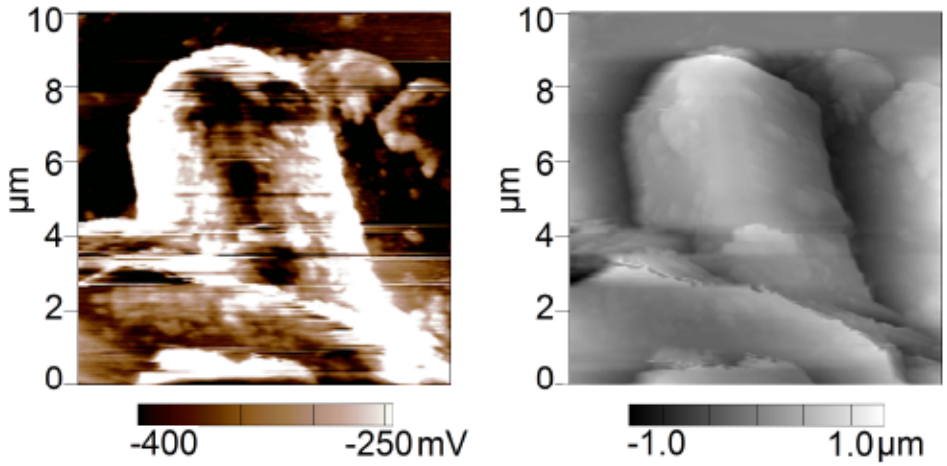

Figure 2.3: Concurrent KPFM and morphology scans of A35.

Table 2.2: Work function Φ for Au films of varying thicknesses. The change in Φ with thickness for Au films on ZnO is markedly different than for Au films on glass, as a result of the Fermi level equilibrium with ZnO.

	Φ (eV)	
Au thickness (nm)	Au on glass	Au on ZnO
45	4.54 ±0.06	5.10 ±0.02
35	4.52 ±0.06	5.02 ±0.05
25	4.49 ±0.09	4.64 ±0.02
15	4.28 ±0.08	4.57 ±0.04

sharp increase from 15 nm to 25 nm but a subsequent drop (the appendix, Table A.1), which is quite different than the surface area trend. In fact, there is no direct relationship between surface roughness and surface area. [37] Therefore, I can see a separate impact of roughness on the surface area corrected EF (EF*).

Figure 2.4 shows a complete picture of the Au thickness dependent SERS activity, where surface charge and surface roughness effects compete. The electrostatic and geometric advantages balance out for higher thicknesses of Au, giving rise to the similar SERS response of A25, A35 and A45.

A35, the highest-performing substrate, was then tested over a broad range of concentrations. I plot the intensity of the 710 cm^{-1} peak versus analyte concentration in Figure 2.5. Clearly the A35 substrate has excellent enhancement over a wide range

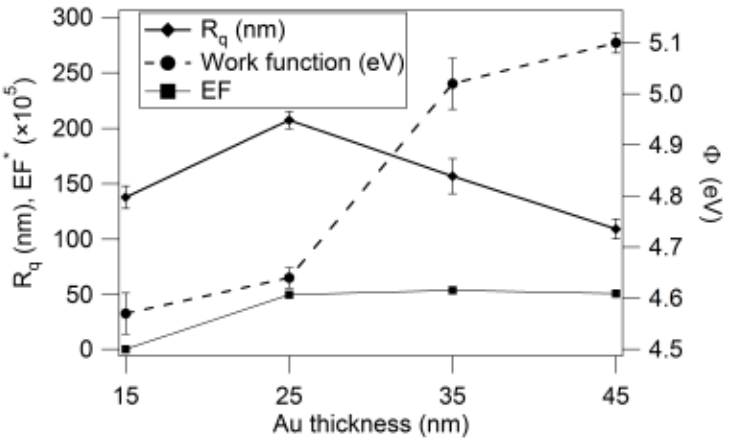

Figure 2.4: Both surface roughness (R_q) and surface charge (through the work function, Φ) are controlling factors of the Au thickness dependent Raman enhancement (EF^*).

of concentrations. This plot does not establish the limit of detection: the 710 cm^{-1} phenanthrene peak was detectable even as low as 1 ppb (the appendix, Figure A.5).

The 710 cm^{-1} peak intensity shows an apparent log-linearity with analyte concentration over this broad range. A non-linear response of intensity to concentration is not surprising in SERS detection, because the signal requires surface adsorption of the analyte. SERS intensity is directly proportional to the number of *adsorbed* molecules in the scattering volume. [31] The relationship between solution concentration and surface coverage, however, is generally not linear, with surface coverage leveling off at higher concentrations, as in the Langmuir adsorption model. [38] The functional form of the Langmuir adsorption profile is similar to a logarithm; hence the apparent log-linearity of the plot in Figure 2.5.

2.5 Conclusions

In conclusion, this work introduces a new approach, KPFM, to investigate SERS enhancement mechanisms. By considering the roles of surface charge and surface

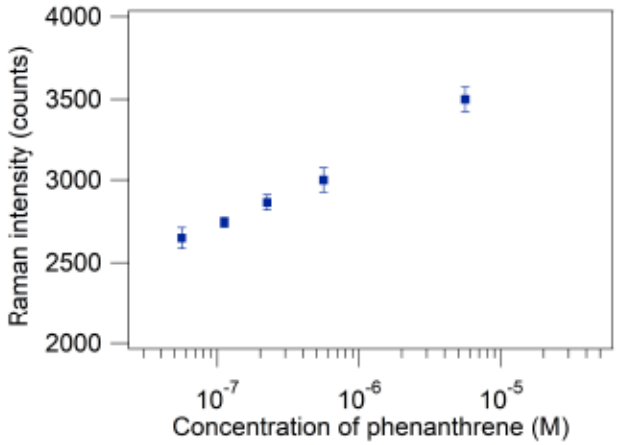

Figure 2.5: The intensity of the 710 cm^{-1} peak increases with higher concentrations of analyte. The relation between concentration and intensity follows a (non-linear) Langmuir adsorption profile.

roughness together, through the simultaneous acquisition of electrical and morphological data, a comprehensive enhancement mechanism emerged. The surface area corrected EF (EF^*) is essential to convincingly show the impacts of factors beyond surface area. With better understanding of the Raman enhancement mechanism in metal/semiconductor nanohybrids, I developed highly efficient Au/ZnO SERS substrates for the trace detection of phenanthrene in water.

Bibliography

[1] Sebastian Schlücker. Surface-Enhanced Raman Spectroscopy: Concepts and Chemical Applications. *Angew. Chem. Int. Ed.*, 53(19):4756, 2014.

[2] Bhavya Sharma, Renee R. Frontiera, Anne-Isabelle Henry, Emilie Ringe, and Richard P. Van Duyne. SERS: Materials, applications, and the future. *Mater. Today*, 15(1–2):16, 2012.

[3] Arumugam Sivanesan, Evelin Witkowska, Witold Adamkiewicz, Lukasz Dziewit,

Agnieszka Kaminska, and Jacek Waluk. Nanostructured silver-gold bimetallic SERS substrates for selective identification of bacteria in human blood. *Analyst*, 139:1037, 2014.

[4] Zao Yi, Xiulan Tan, Gao Niu, Xibin Xu, Xibo Li, Xin Ye, Jiangshan Luo, Binchi Luo, Weidong Wu, Yongjian Tang, and Yougen Yi. Facile preparation of dendritic Ag–Pd bimetallic nanostructures on the surface of Cu foil for application as a SERS-substrate. *Appl. Surf. Sci.*, 258(14):5429, 2012.

[5] Lingwei Ma, Yu Huang, Mengjing Hou, Zheng Xie, and Zhengjun Zhang. Ag Nanorods Coated with Ultrathin TiO2 Shells as Stable and Recyclable SERS Substrates. *Sci. Rep.*, 5:15442, 2015.

[6] Ruibin Jiang, Benxia Li, Caihong Fang, and Jianfang Wang. Metal/Semiconductor Hybrid Nanostructures for Plasmon-Enhanced Applications. *Adv. Mater.*, 26(31):5274, 2014.

[7] Zhao, Lasse Jensen, and George C. Schatz. Pyridine−Ag_{20} Cluster: A Model System for Studying Surface-Enhanced Raman Scattering. *J. Am. Chem. Soc.*, 128(9):2911, 2006.

[8] Liping Liu, Haitao Yang, Xiao Ren, Jin Tang, Yongfeng Li, Xiangqun Zhang, and Zhaohua Cheng. Au-ZnO hybrid nanoparticles exhibiting strong charge-transfer-induced SERS for recyclable SERS-active substrates. *Nanoscale*, 7:5147, 2015.

[9] Shaochun Tang, Sascha Vongehr, Yongguang Wang, Juan Cui, Xiangyu Wang, and Xiangkang Meng. Versatile synthesis of high surface area multi-metallic nanosponges allowing control over nanostructure and alloying for catalysis and SERS detection. *J. Mater. Chem. A*, 2:3648, 2014.

[10] Hu Cang, Anna Labno, Changgui Lu, Xiaobo Yin, Ming Liu, Christopher Gladden, Yongmin Liu, and Xiang Zhang. Probing the electromagnetic field of a 15-nanometre hotspot by single molecule imaging. *Nature*, 469(7330):385, 2011.

[11] Meikun Fan, Feng-Ju Lai, Hung-Lung Chou, Wan-Ting Lu, Bing-Joe Hwang, and Alexandre G. Brolo. Surface-enhanced Raman scattering (SERS) from Au:Ag bimetallic nanoparticles: the effect of the molecular probe. *Chem. Sci.*, 4:509, 2013.

[12] Limei Tian, Sirimuvva Tadepalli, Mikella E. Farrell, Keng-Ku Liu, Naveen Gandra, Paul M. Pellegrino, and Srikanth Singamaneni. Multiplexed charge-selective surface enhanced Raman scattering based on plasmonic calligraphy. *J. Mater. Chem. C*, 2:5438, 2014.

[13] Kunyu Zhao, Jie Lin, and Lin Guo. ZnO/Ag porous nanosheets used as substrate for surface-enhanced Raman scattering to detect organic pollutant. *RSC Adv.*, 5:53524, 2015.

[14] Haibin Tang, Guowen Meng, Qing Huang, Zhuo Zhang, Zhulin Huang, and Chuhong Zhu. Arrays of Cone-Shaped ZnO Nanorods Decorated with Ag Nanoparticles as 3D Surface-Enhanced Raman Scattering Substrates for Rapid Detection of Trace Polychlorinated Biphenyls. *Adv. Funct. Mater.*, 22(1):218, 2012.

[15] Shuichi Hashimoto, Sigeru Ikuta, Tsuyoshi Asahi, and Hiroshi Masuhara. Fluorescence Spectroscopic Studies of Anthracene Adsorbed into Zeolites: From the Detection of Cation$-\pi$ Interaction to the Observation of Dimers and Crystals. *Langmuir*, 14(15):4284, 1998.

[16] Dongqiang Zhu, Bruce E. Herbert, Mark A. Schlautman, Elizabeth R. Carraway, and Jin Hur. Cation-pi Bonding: A New Perspective on the Sorption of Polycyclic Aromatic Hydrocarbons to Mineral Surfaces. *J. Environ. Qual.*, 33(4):1322, 2004.

[17] Man Zhou, Ming Lin, Lie Chen, Yongzheng Wang, Xiangke Guo, Luming Peng, Xuefeng Guo, and Weiping Ding. Thickness-dependent SERS activities of gold nanosheets controllably synthesized via photochemical reduction in lamellar liquid crystals. *Chem. Commun.*, 51:5116, 2015.

[18] K. Saravanan, R. Krishnan, S. H. Hsieh, H. T. Wang, Y. F. Wang, W. F. Pong, K. Asokan, D. K. Avasthi, and D. Kanjilal. Effect of defects and film thickness on the optical properties of ZnO-Au hybrid films. *RSC Adv.*, 5:40813, 2015.

[19] Changwon Lee, Christopher S. Robertson, An H. Nguyen, Mehmet Kahraman, and Sebastian Wachsmann-Hogiu. Thickness of a metallic film, in addition to its roughness, plays a significant role in SERS activity. *Sci. Rep.*, 5:11644, 2015.

[20] Wan-Hsien Lin, Jih-Jen Wu, Mitch M. C. Chou, Yu-Ming Chang, and Masahiro Yoshimura. Charge Transfer in Au Nanoparticle–Nonpolar ZnO Photocatalysts Illustrated by Surface-Potential-Derived Three-Dimensional Band Diagram. *J. Phys. Chem. C*, 118(34):19814, 2014.

[21] Yu-Hsiang Sung, Vadim D. Frolov, Sergei M. Pimenov, and Jih-Jen Wu. Investigation of charge transfer in Au nanoparticle-ZnO nanosheet composite photocatalysts. *Phys. Chem. Chem. Phys.*, 14:14492, 2012.

[22] M. Bieletzki, T. Hynninen, T. M. Soini, M. Pivetta, C. R. Henry, A. S. Foster, F. Esch, C. Barth, and U. Heiz. Topography and work function measurements of thin MgO(001) films on Ag(001) by nc-AFM and KPFM. *Phys. Chem. Chem. Phys.*, 12:3203, 2010.

[23] Jingli Mu, Juying Wang, Fei Jin, Xinhong Wang, and Huasheng Hong. Comparative embryotoxicity of phenanthrene and alkyl-phenanthrene to marine medaka (Oryzias melastigma). *Mar. Pollut. Bull.*, 85(2):505, 2014.

[24] Ruth A. McBride, John M. Kelly, and Declan E. McCormack. Growth of well-defined ZnO microparticles by hydroxide ion hydrolysis of zinc salts. *J. Mater. Chem.*, 13:1196, 2003.

[25] Zhuo Wang, Xue feng Qian, Jie Yin, and Zi kang Zhu. Large-Scale Fabrication of Tower-like, Flower-like, and Tube-like ZnO Arrays by a Simple Chemical Solution Route. *Langmuir*, 20(8):3441, 2004.

[26] Umair Manzoor, Do K. Kim, Mohammad Islam, and Arshad S. Bhatti. Removal of Micrometer Size Morphological Defects and Enhancement of Ultraviolet Emission by Thermal Treatment of Ga-Doped ZnO Nanostructures. *PLOS ONE*, 9(1):1, 2014.

[27] M Tzolov, N Tzenov, D Dimova-Malinovska, M Kalitzova, C Pizzuto, G Vitali, G Zollo, and I Ivanov. Vibrational properties and structure of undoped and Al-doped ZnO films deposited by RF magnetron sputtering. *Thin Solid Films*, 379(1):28, 2000.

[28] V. Russo, M. Ghidelli, P. Gondoni, C. S. Casari, and A. Li Bassi. Multi-wavelength Raman scattering of nanostructured Al-doped zinc oxide. *J. Appl. Phys.*, 115(7):073508, 2014.

[29] A. S. Shaporev, V. K. Ivanov, A. E. Baranchikov, O. S. Polezhaeva, and Yu. D. Tret'yakov. ZnO formation under hydrothermal conditions from zinc hydroxide compounds with various chemical histories. *Russ. J. Inorg. Chem.*, 52(12):1811, 2007.

[30] Shan Cong, Yinyin Yuan, Zhigang Chen, Junyu Hou, Mei Yang, Yanli Su, Yongyi Zhang, Liang Li, Qingwen Li, Fengxia Geng, and Zhigang Zhao. Noble metal-comparable SERS enhancement from semiconducting metal oxides by making oxygen vacancies. *Nat. Commun.*, 6:7800, 2015.

[31] Eric C. Le Ru and Pablo G. Etchegoin. Chapter 4 - SERS enhancement factors and related topics. In Eric C. Le Ru, , and Pablo G. Etchegoin, editors, *Principles of Surface-Enhanced Raman Spectroscopy*, pages 185 – 264. Elsevier, Amsterdam, 2009.

[32] E. C. Le Ru, E. Blackie, M. Meyer, and P. G. Etchegoin. Surface Enhanced Raman Scattering Enhancement Factors: A Comprehensive Study. *J. Phys. Chem. C*, 111(37):13794, 2007.

[33] Antoine Kahn. Fermi level, work function and vacuum level. *Mater. Horiz.*, 3:7, 2016.

[34] J. Vancea, G. Reiss, D. Butz, and H. Hoffmann. Thickness-Dependent Effects in the Work Function of Polycrystalline Cu-Films. *EPL*, 9(4):379, 1989.

[35] Mark Turner, Vladimir B. Golovko, Owain P. H. Vaughan, Pavel Abdulkin, Angel Berenguer-Murcia, Mintcho S. Tikhov, Brian F. G. Johnson, and Richard M. Lambert. Selective oxidation with dioxygen by gold nanoparticle catalysts derived from 55-atom clusters. *Nature*, 454:981, 2008.

[36] Luis M. Liz-Marzán, Michael Giersig, and Paul Mulvaney. Synthesis of Nanosized Gold−Silica Core−Shell Particles. *Langmuir*, 12(18):4329, 1996.

[37] M.G. Donoso, A. Méndez-Vilas, J.M. Bruque, and M.L. González-Martin. On the relationship between common amplitude surface roughness parameters and

surface area: Implications for the study of cell–material interactions. *Int. Biodeterior. Biodegrad.*, 59(3):245, 2007.

[38] Mark R. Kagan and Richard L. McCreery. Quantitative Surface Raman Spectroscopy of Physisorbed Monolayers on Glassy Carbon. *Langmuir*, 11(10):4041, 1995.

Chapter 3

Thermal Annealing: A Three-fold Approach to Improving Surface Enhanced Raman Scattering (SERS) Activity of Metal-semiconductor Substrate*

3.1 Abstract

The heat treatment of ZnO crystals with subsequent deposition of Au not only tunes the hydrophobicity as a result of the change of morphology of the system but also modifies the electronic interaction between the analyte and the substrate. Combination of both electromagnetic enhancement (EM) and chemical enhancement (CM) allow to achieve nanomolar detection.

*in preparation for re-submission

3.2 Introduction

Nonpolar polycyclic aromatic hydrocarbons (PAHs) are considered as serious environmental pollutant, [1] because their carcinogenic effects. [2] Surface enhanced Raman scattering (SERS) is an excellent method for detection of analytes at trace concentration. [3] However, trace detection of nonpolar molecules by SERS is quite challenging due to not only the spectral overlap of their Raman peaks but also the non-adsorbing properties of molecules towards the plasmonic metal surface.

This low affinity of PAHs towards the metal surface was greatly improved by several approaches. Functionalization of the metal surface or the introduction of a co-material to bind the PAH molecules can increase the surface adsorption on the metal surface, which magnify the near-field effect. [4,5] In another approach, a hydrophobic organic layer was used to make the metal surface highly hydrophobic to adsorb a nonpolar molecule (pyrene). [6] The thermodynamic driver for the adsorption of the nonpolar molecule on a hydrophobic surface comes from minimizing water–surface and water–nonpolar molecule contact.

A rougher metal surface can be more hydrophobic [7,8] because of the formation of air pockets in the surface cavities. [9] Therefore, the surface morphology can change the hydrophobicity. Furthermore, a rough plasmonic metal surface generates intense electromagnetic hotspots through the coupling of the plasmonic field at the junction of metal clusters, which is the so-called electromagnetic enhancement. [10,11]

In this work, I use thermal annealing of ZnO to both control hydrophobicity and alter the electronic structure of Au/ZnO nanohybrids. The SERS activity of these semiconductor-metal nanohybrids has been well explored, [12,13] linking SERS response to charge transfer at the metal-semiconductor interface and the formation of plasmonic hotspots. [14–16] Herein, I identify the multifold enhancement mechanism arising from a simple annealing treatment by relating the Raman enhancement to

the substrate's material properties. In the case of semiconductor-metal nanohybrids, annealing changes not only the hydrophobicity but also the electronic properties. This impacts the metal–molecule interaction at several levels, and is the focus of my research.

3.3 Experimental

ZnO crystals were synthesized by a sol-gel process using $ZnOAc_2 \cdot 2\,H_2O$ and sodium hydroxide (NaOH) as precursor materials (detailed synthetic approach is described in Appendix B.1). [17] As-prepared ZnO films on glass slides were annealed in a programmable furnace (Thermo Scientific) at two different temperatures (200°C and 400°C) for 2 hours. 35 nm of Au was deposited using an in-lab-built metal evaporator on the unannealed and annealed ZnO layers. A quartz crystal microbalance (QCM, INFICON XTM/2) was used for monitoring Au thickness. For convenience I refer to these three types of Au/ZnO substrates as AZRT (Au on unannealed or room temperature ZnO), AZ200 (Au on ZnO annealed at 200°C) and AZ400 (Au on ZnO annealed at 400°C).

3.4 Results and discussion

Field emission scanning electron microscopy (FESEM) images (details on instrumentation are given in Appendix B.2) of unannealed and annealed ZnO crystals are shown in Figure 3.1. The thermal treatment generates fractures on the ZnO crystal surface, which could be the result of thermal stress or water elimination. These fractures contribute to the formation of a rough surface, and consequently the generation of the hydrophobic surface [8] and plasmonic hotspots [18] after Au deposition. I investigated this further using a range of materials characterization techniques.

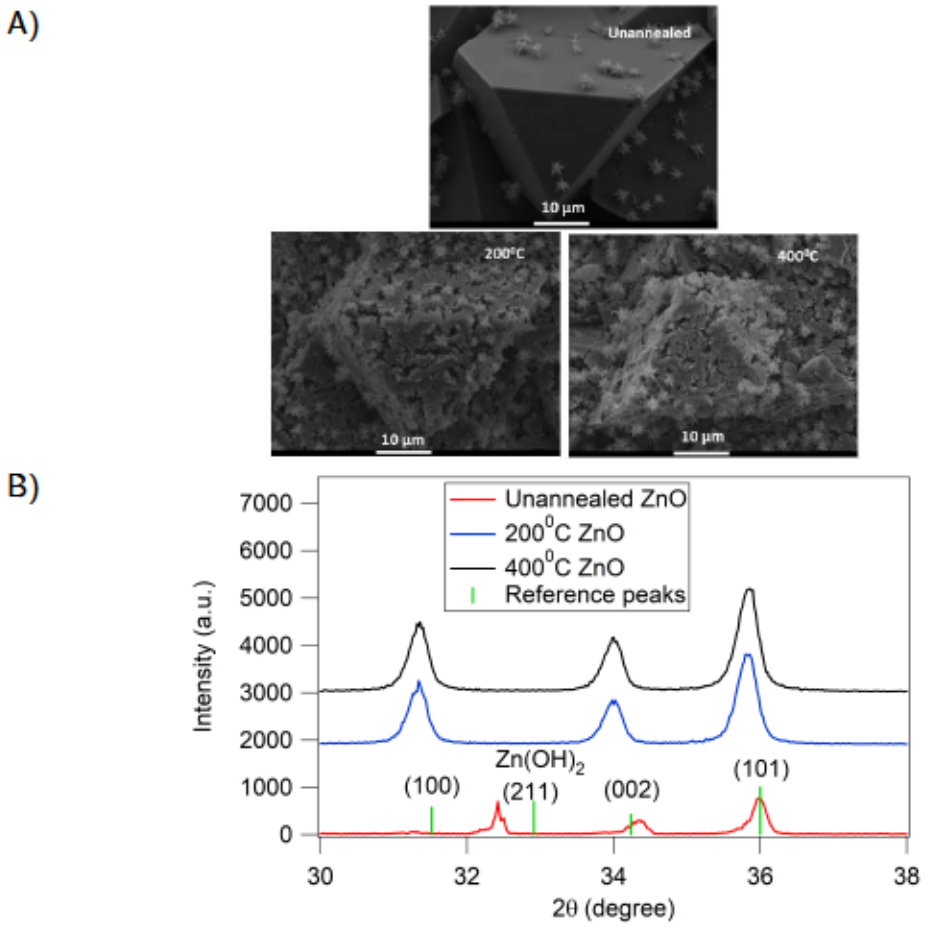

Figure 3.1: A) FESEM images of unannealed and annealed ZnO crystals show the formation of fractures due to annealing. B) XRD data of annealed and unannealed ZnO crystals indicate structural changes with the heat treatment: Unannealed ZnO (red), 200°C annealed (blue) and 400°C annealed (black) (graphs are offset for clarity).

Prepared ZnO substrates were characterized using XRD (Details on instrumentation are given in Appendix B.2). The XRD data confirmed the hexagonal wurtzite structure of ZnO crystals, [17] but the XRD patterns of annealed ZnO crystals show significant shifts in their peak positions relative to the unannealed crystals (Figure 3.1). The shift of the diffraction peaks generally occurs due to chemical composition change or strain in the crystal structure. [19, 20] Both of these play a role in my system, as shown by the XRD data discussed here and the Raman data discussed below. The heat treatment causes thermal stress due to the ZnO/glass thermal coefficient

mismatch. This thermal stress results in a tensile strain, and diffraction peaks shift to a lower 2θ value. Heat-treated ZnO films show sharper diffraction peaks (or decrease in the FWHM) compared to the as-prepared ones, showing an improvement of the crystallinity. Greater crystallinity in ZnO from heat treatment has also been observed by Conchon et al. [21]

AZRT has an additional diffraction peak at 32.5° 2θ, which may be due to the overlap of the ZnO (100) peak [17] and the diffraction peak of $Zn(OH)_2$ [22] (formed during the sol-gel preparation). This peak disappeared after annealing, as would be expected for the $Zn(OH)_2$ phase. This was confirmed by thermogravimetric analysis (TGA). During the TGA experiment, a ZnO sample was heated to 200°C and then held for 2 hours to mimic the annealing treatment. A 13.5% weight loss occurred, primarily between 100°C and 150°C (the appendix, Figure B.2), which is mainly due to the elimination of water. [23] Therefore, it can be concluded that the as-prepared ZnO crystals contain $Zn(OH)_2$ as a secondary phase, which explains the appearance of an extra XRD peak.

The presence of a $Zn(OH)_2$ phase in AZRT was confirmed with Raman characterization of the substrate. The Raman analysis (the appendix, Figure B.1) showed a characteristic ZnO vibrational peak at 438 cm^{-1} after thermal annealing of the ZnO sample, [24] and the corresponding disappearance of the $Zn(OH)_2$ peak at 367 cm^{-1}. [25]

Plasmon absorption spectra (Figure 3.2) of the three types of Au/ZnO nanohybrid substrates were collected using an Ocean Optics USB 2000 spectrophotometer through diffuse reflectance spectroscopy (DRS). [26] This intense surface plasmon field arises from plasmonic hotspots formed due to roughening of the surface as a result of annealing. [3] Additionally, surface roughness also plays a role in tuning the plasmon absorption to the NIR region. [27]

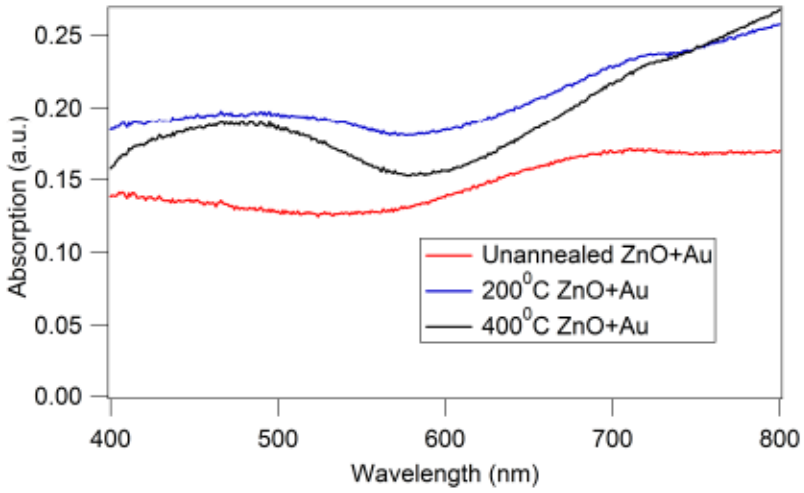

Figure 3.2: Au-covered annealed ZnO yields substrates (AZ200, blue; AZ400, black) with higher plasmonic absorption relative to Au on unannealed ZnO (AZRT, red).

SERS experiments were conducted to detect trace amounts of phenanthrene in water. 1 ppm aqueous solution of phenanthrene provided the test analyte for determining the SERS activity of three types of Au/ZnO substrates. SERS substrates were soaked in the 1 ppm phenanthrene solution in a beaker for 30 minutes and then rinsed well with ultrapure water and air dried. Five different areas on each substrate were scanned during the SERS measurement. Figure 3.3 depicts SERS spectra of phenanthrene on the three substrates, with AZ400 having the highest SERS activity of the three.

The combined C–C stretching and HCC bending vibrational mode at 710 cm^{-1} [28] was taken as the characteristic analyte peak for the enhancement factor calculations. It is worth noting that the enhancement trend is the same for the other phenanthrene modes as well. Enhancement factor calculations were calculated through the analytical method (the appendix, equation B.3). [29] AZ400 was the most effective substrate with an enhancement factor (EF) of 1.2×10^5, which is also higher than the previously reported EF value (10^4) of another super hydrophobic substrate. [6] AZ200 and AZRT have comparable Raman signal enhancements. AZ200 displayed EF of 5.1×10^4 and

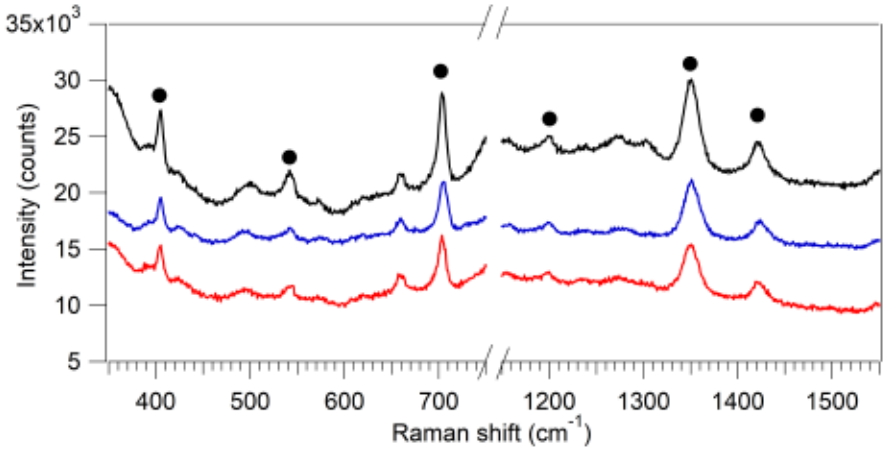

Figure 3.3: SERS spectra of phenanthrene on different Au/ZnO substrates: AZ400 (black) has the highest SERS activity in comparison to AZ200 (blue) and AZRT (red). (Plots are offset for clarity).

AZRT has the EF of 4.7×10^4. This nearly equal enhancement activity of AZRT and AZ200 cannot be explained by the plasmonic absorption study alone. For this I had to study the metal-molecule interaction, as described below.

The hydrophobic nature of these substrates is one of the main features of this study. The hydrophobic character of SERS substrates enhances surface adsorption of PAH (and other nonpolar) molecules from aqueous solution. Contact angle measurements (details on instrumentation are given in Appendix B.7) of water on the substrates confirmed their hydrophobicity. Freshly-prepared Au films on glass showed high water wettability. Au on unannealed ZnO has a contact angle of 122°, while annealing makes the contact angle as high as 146° (AZ400). The photographs of water droplets on the surfaces in Figure 3.4 show directly that thermal annealing led to an increase in the hydrophobicity. [9]

The hydrophobicity of the three types of Au/ZnO nanohybrid substrate is explained by the formation of the rough surface as a result of the annealing treatment. Kelvin probe force microscopy (KPFM) was employed to compare the surface roughness of Au/ZnO substrates. This technique can also probe metal-molecule interactions

Figure 3.4: Photographs or water droplets on Au covered ZnO substrates showing the change in hydrophobicity after thermal treatment.

as described below. Morphology data of 1×1 μm^2 areas of annealed and unannealed Au/ZnO substrates revealed that AZ400 has the highest surface roughness factor (R_q) relative to AZ200 and AZRT (see Appendix B.8 for surface roughness calculations). This rougher surface is able to increase the water–surface contact angle by generating air-pockets, as in the Cassie model, [7] which is explained in more detail in the appendix, section B.7 and equation B.4. The correlation between the roughness factor and the water contact angle is clearly seen in Figure 3.5, with values given in Table 3.1.

Table 3.1: A direct relationship between the surface roughness factor (R_q) and the hydrophobicity (water contact angle).

Au/ZnO Substrate	Contact angle (in °)	R_q (nm)
AZ400	146.1 ±1.8	16.478 ±1.36
AZ200	140.9 ±1.7	14.357 ±0.92
AZRT	122.6 ±3.5	9.171 ±2.03

KPFM data also indicated the degree of the electronic interaction between phenanthrene and Au/ZnO substrates. In KPFM, a contact potential difference (CPD) arises between the conductive tip and the surface of the material under an applied electric field. [30] CPD values are affected by changes in surface charge, which in my case arise from Fermi level equilibrium at the Au/ZnO interface. Changes in electronic

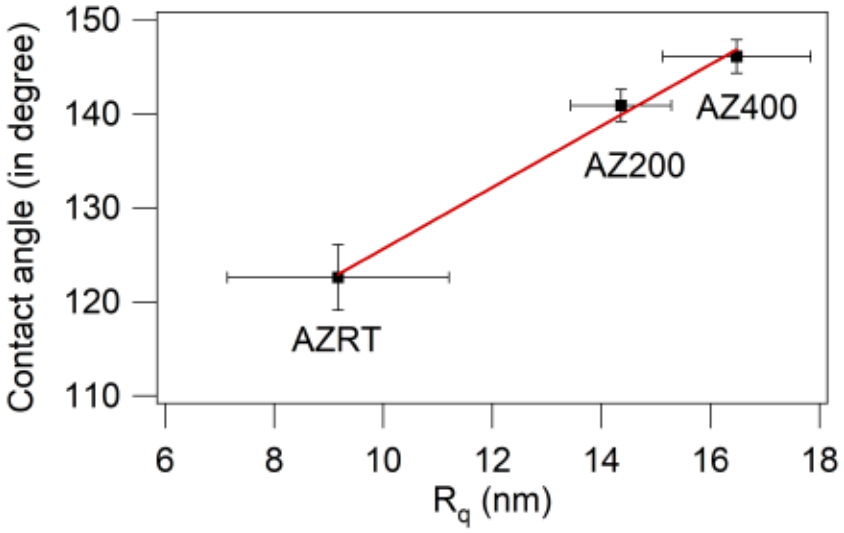

Figure 3.5: Plot showing a linear relationship between the roughness factor and the water contact angle. The r^2 value for the fit (red line) is 0.9973.

structure of the ZnO layer would lead to changes in charge transfer between ZnO and Au, and next between Au and the adsorbed analyte. Cathodoluminescence data (the appendix, Figure B.3) confirm significant changes in ZnO electronic structure upon annealing. [20]

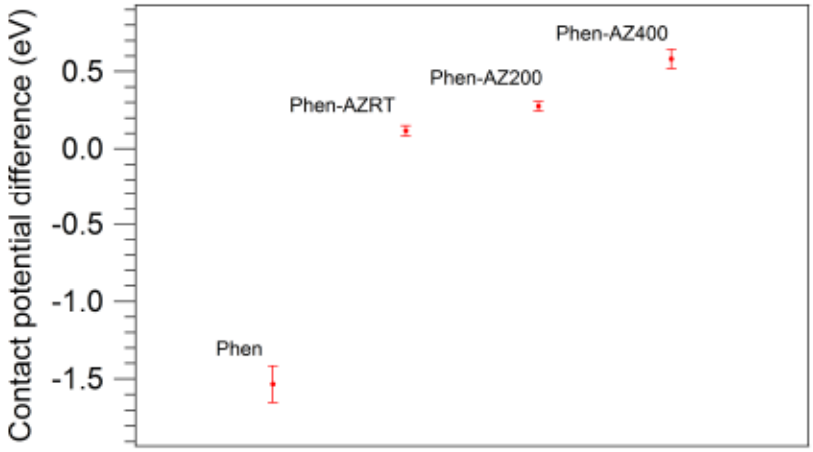

Figure 3.6: A consistent change of CPD of adsorbed phenanthrene on Au covered heat treated ZnO substrate.

Changes in surface charge will impact the degree of substrate–molecule adsorption. Therefore, the CPD value is a measure of the analyte–SERS substrate interaction.

This is important for SERS substrates, because any increase of the metal–molecule interaction can result in a change of the polarizability of the adsorbed molecule, and consequently enhances the Raman response. [31, 32]

CPD values was measured for phenanthrene on glass as well as on Au/ZnO substrates. The sharp difference in CPD between adsorbed phenanthrene on Au/ZnO substrates and phenanthrene on glass (Figure 3.6) demonstrates a change in metal-molecule interaction. Phenanthrene molecule does not have any electronic interaction with glass substrate. [33,34] The strongest interaction between phenanthrene and the AZ400 substrate leads to that substrate's highest SERS activity. The comparable SERS activity of AZRT and AZ200 can be ascribed to their nearly equal metal–molecule interaction strengths.

Detection efficacy for trace concentrations was studied with the substrate with highest SERS activity (AZ400). Nanomolar detection was achieved by AZ400. The intensity of the characteristic Raman signal of phenanthrene (710 cm^{-1} mode) increased with increasing concentration of phenanthrene. This is plotted on a log–linear scale in Figure 3.7 for easy comparison with analogous data in Figures 4.5 and 2.5. However, the relationship is quite linear over a very large concentration range (see inset in Figure 3.7). The linear response indicates that we have not approached saturation in analyte adsorption, made possible by the significantly larger surface area of the AZ400 substrate when compared with substrates from other chapters (see the appendix, Table B.1). Therefore, both quantitative and qualitative detection of phenanthrene can be successfully performed by AZ400.

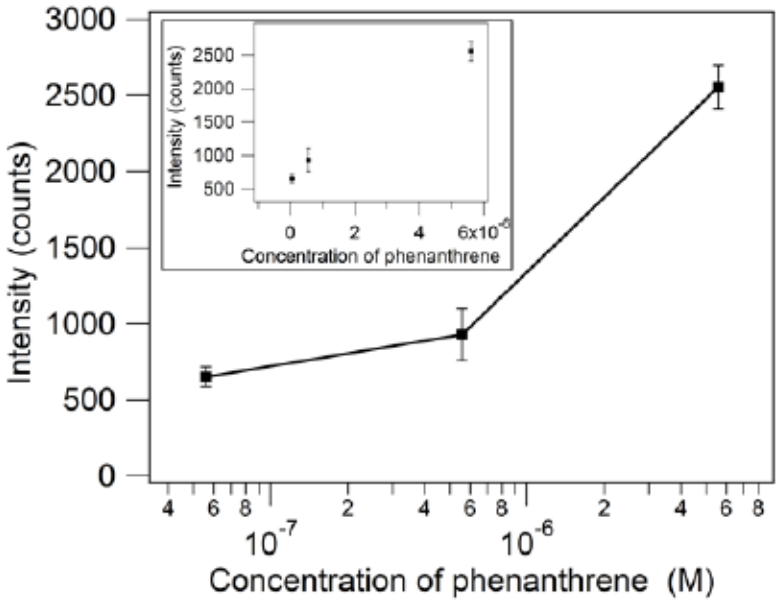

Figure 3.7: Quantitative detection of phenanthrene by SERS. The Raman intensity decreases linearly with the concentration of phenanthrene (see inset, $r^2 = 0.9985$). A log-linear plot shows more clearly the intensities at different concentrations.

3.5 Conclusions

In conclusion, high performing Au/ZnO SERS substrates were fabricated using a simple sol-gel technique and thermal vapor deposition. 0.01 ppm or nanomolar detection of phenanthrene was achieved by the highest performing substrate. It was established that the high temperature annealed ZnO with Au has high SERS activity. Annealing the ZnO underlayer has a three-fold impact on the SERS activity of Au/ZnO substrates. Annealing creates a rough surface, generating electromagnetic hotspots. This roughness also leads to a more hydrophobic surface, which enhances adsorption. In addition, annealing improves the metal–molecule electronic interaction, leading to Raman enhancement. Therefore, this multifunctional thermal annealing approach provides a surprisingly simple route to fabricating SERS substrates with high EFs.

Bibliography

[1] Jingli Mu, Juying Wang, Fei Jin, Xinhong Wang, and Huasheng Hong. Comparative embryotoxicity of phenanthrene and alkyl-phenanthrene to marine medaka (Oryzias melastigma). *Mar. Pollut. Bull.*, 85(2):505, 2014.

[2] M. H. Falahatpisheh, K. C. Donnelly, and K. S. Ramos. Antagonistic interactions among nephrotoxic polycyclic aromatic hydrocarbons. *J Toxicol Environ Health A*, 62(7):543, 2001.

[3] Sebastian Schlücker. Surface-Enhanced Raman Spectroscopy: Concepts and Chemical Applications. *Angew. Chem. Int. Ed.*, 53(19):4756, 2014.

[4] Yunfei Xie, Xu Wang, Xiaoxia Han, Xiangxin Xue, Wei Ji, Zhenhui Qi, Junqiu Liu, Bing Zhao, and Yukihiro Ozaki. Sensing of polycyclic aromatic hydrocarbons with cyclodextrin inclusion complexes on silver nanoparticles by surface-enhanced Raman scattering. *Analyst*, 135:1389, 2010.

[5] Meng Jiang, Zhijiang Qian, Xufeng Zhou, Xing Xin, Jinghua Wu, Chao Chen, Gongjun Zhang, Gaojie Xu, and Yuchuan Cheng. CTAB micelles assisted rGO-AgNP hybrids for SERS detection of polycyclic aromatic hydrocarbons. *Phys. Chem. Chem. Phys.*, 17:21158, 2015.

[6] Hongyue Zhao, Jing Jin, Weijun Tian, Ran Li, Zhi Yu, Wei Song, Qian Cong, Bing Zhao, and Yukihiro Ozaki. Three-dimensional superhydrophobic surface-enhanced Raman spectroscopy substrate for sensitive detection of pollutants in real environments. *J. Mater. Chem. A*, 3:4330, 2015.

[7] Daiming Liu, Qingkang Wang, and Jing Hu. Fabrication and characterization of highly ordered Au nanocone array-patterned glass with enhanced SERS and hydrophobicity. *Appl. Surf. Sci.*, 356:364, 2015.

[8] Lixiao Jing, Yu-e Shi, Jingcheng Cui, Xiaoli Zhang, and Jinhua Zhan. Hydrophobic gold nanostructures via electrochemical deposition for sensitive SERS detection of persistent toxic substances. *RSC Adv.*, 5:13443, 2015.

[9] Yuanyuan Cheng, Shixiang Lu, Wenguo Xu, Huidong Wen, and Juan Wang. Fabrication of superhydrophobic Au-Zn alloy surface on a zinc substrate for roll-down, self-cleaning and anti-corrosion properties. *J. Mater. Chem. A*, 3:16774, 2015.

[10] Christy L. Haynes and Richard P. Van Duyne. Plasmon-Sampled Surface-Enhanced Raman Excitation Spectroscopy. *J. Phys. Chem. B*, 107(30):7426, 2003.

[11] Matthew J. Banholzer, Jill E. Millstone, Lidong Qin, and Chad A. Mirkin. Rationally designed nanostructures for surface-enhanced Raman spectroscopy. *Chem. Soc. Rev.*, 37:885, 2008.

[12] Ruibin Jiang, Benxia Li, Caihong Fang, and Jianfang Wang. Metal/Semiconductor Hybrid Nanostructures for Plasmon-Enhanced Applications. *Adv. Mater.*, 26(31):5274, 2014.

[13] Lingwei Ma, Yu Huang, Mengjing Hou, Zheng Xie, and Zhengjun Zhang. Ag Nanorods Coated with Ultrathin TiO2 Shells as Stable and Recyclable SERS Substrates. *Sci. Rep.*, 5:15442, 2015.

[14] Zhihua Sun, Chunxu Wang, Jingxiu Yang, Bing Zhao, and John R. Lombardi. Nanoparticle Metal−Semiconductor Charge Transfer in ZnO/PATP/Ag Assemblies by Surface-Enhanced Raman Spectroscopy. *J. Phys. Chem. C*, 112(15):6093, 2008.

[15] Limiao Chen, Linbao Luo, Zhenhua Chen, Mingliang Zhang, Juan Antonio Zapien, Chun Sing Lee, and Shuit Tong Lee. ZnO/Au Composite Nanoarrays As Substrates for Surface-Enhanced Raman Scattering Detection. *J. Phys. Chem. C*, 114(1):93, 2010.

[16] Hui He, Huoquan Li, Weiwei Xia, Xiaoshuang Shen, Min Zhou, Jiurong Han, Xianghua Zeng, and Weiping Cai. Electrophoretic fabrication of silver nanostructure/zinc oxide nanorod heterogeneous arrays with excellent SERS performance. *J. Mater. Chem. C*, 3:1724, 2015.

[17] Ruth A. McBride, John M. Kelly, and Declan E. McCormack. Growth of well-defined ZnO microparticles by hydroxide ion hydrolysis of zinc salts. *J. Mater. Chem.*, 13:1196, 2003.

[18] Hu Cang, Anna Labno, Changgui Lu, Xiaobo Yin, Ming Liu, Christopher Gladden, Yongmin Liu, and Xiang Zhang. Probing the electromagnetic field of a 15-nanometre hotspot by single molecule imaging. *Nature*, 469(7330):385, 2011.

[19] Umair Manzoor, Do K. Kim, Mohammad Islam, and Arshad S. Bhatti. Removal of Micrometer Size Morphological Defects and Enhancement of Ultraviolet Emission by Thermal Treatment of Ga-Doped ZnO Nanostructures. *PLOS ONE*, 9(1):1, 2014.

[20] Hong Seong Kang, Jeong Seok Kang, Jae Won Kim, and Sang Yeol Lee. Annealing effect on the property of ultraviolet and green emissions of ZnO thin films. *J. Appl. Phys.*, 95(3):1246, 2004.

[21] F. Conchon, P.O. Renault, E. Le Bourhis, C. Krauss, P. Goudeau, E. Barthel, S. Yu. Grachev, E. Sondergard, V. Rondeau, R. Gy, R. Lazzari, J. Jupille, and

N. Brun. X-ray diffraction study of thermal stress relaxation in ZnO films deposited by magnetron sputtering. *Thin Solid Films*, 519(5):1563, 2010.

[22] A. S. Shaporev, V. K. Ivanov, A. E. Baranchikov, O. S. Polezhaeva, and Yu. D. Tret'yakov. ZnO formation under hydrothermal conditions from zinc hydroxide compounds with various chemical histories. *Russ. J. Inorg. Chem.*, 52(12):1811, 2007.

[23] Mohd Farhan Khan, Akhter H. Ansari, M. Hameedullah, Ejaz Ahmad, Fohad Mabood Husain, Qamar Zia, Umair Baig, Mohd Rehan Zaheer, Mohammad Mezbaul Alam, Abu Mustafa Khan, Zeid A. AlOthman, Iqbal Ahmad, Ghulam Md Ashraf, and Gjumrakch Aliev. Sol-gel synthesis of thorn-like ZnO nanoparticles endorsing mechanical stirring effect and their antimicrobial activities: Potential role as nano-antibiotics. *Sci. Rep.*, 6:27689, 2016.

[24] Arrigo Calzolari and Marco Buongiorno Nardelli. Dielectric properties and Raman spectra of ZnO from a first principles finite-differences/finite-fields approach. *Sci. Rep.*, 3:2999, 2013.

[25] Mingsong Wang, Lingxia Jiang, Eui Jung Kim, and Sung Hong Hahn. Electronic structure and optical properties of $Zn(OH)_2$: LDA+U calculations and intense yellow luminescence. *RSC Adv.*, 5:87496, 2015.

[26] James H Nobbs. Kubelka-Munk Theory and the Prediction of Reflectance. *Rev. Prog. Color. Relat. Top.*, 15(1):66, 1985.

[27] Jia-Han Li, Shih-Wen Chen, Yi Chou, Ming-Chung Wu, Chun-Hway Hsueh, and Wei-Fang Su. Effects of Gold Film Morphology on Surface Plasmon Resonance Using Periodic P3HT:PMMA/Au Nanostructures on Silicon Substrate for Surface-Enhanced Raman Scattering. *J. Phys. Chem. C*, 115(49):24045, 2011.

[28] A.I. Alajtal, H.G.M. Edwards, M.A. Elbagerma, and I.J. Scowen. The effect of laser wavelength on the Raman Spectra of phenanthrene, chrysene, and tetracene: Implications for extra-terrestrial detection of polyaromatic hydrocarbons. *Spectrochim. Acta Mol. Biomol. Spectrosc.*, 76(1):1, 2010.

[29] E. C. Le Ru, E. Blackie, M. Meyer, and P. G. Etchegoin. Surface Enhanced Raman Scattering Enhancement Factors: A Comprehensive Study. *J. Phys. Chem. C*, 111(37):13794, 2007.

[30] Benjamin C. Hoffman, Terry McAfee, Brad R. Conrad, Marsha A. Loth, John E. Anthony, Harald W. Ade, and Daniel B. Dougherty. Intrinsic Charge Trapping Observed as Surface Potential Variations in diF-TES-ADT Films. *ACS Appl. Mater. Interfaces*, 8(33):21490, 2016.

[31] Lasse Jensen, Christine M. Aikens, and George C. Schatz. Electronic structure methods for studying surface-enhanced Raman scattering. *Chem. Soc. Rev.*, 37:1061, 2008.

[32] Eric C. Le Ru and Pablo G. Etchegoin. Quantifying SERS enhancements. *MRS Bull.*, 38(8):631, 2013.

[33] Mark Turner, Vladimir B. Golovko, Owain P. H. Vaughan, Pavel Abdulkin, Angel Berenguer-Murcia, Mintcho S. Tikhov, Brian F. G. Johnson, and Richard M. Lambert. Selective oxidation with dioxygen by gold nanoparticle catalysts derived from 55-atom clusters. *Nature*, 454:981, 2008.

[34] Luis M. Liz-Marzán, Michael Giersig, and Paul Mulvaney. Synthesis of Nanosized Gold−Silica Core−Shell Particles. *Langmuir*, 12(18):4329, 1996.

Chapter 4

SERS Detection Using Metal-insulator Multilayers: Effect of Insulator on Plasmonic Enhancement*

4.1 Abstract

Metal on polymer on metal oxide substrates are tested for use as a SERS substrate for detection of polycyclic aromatic hydrocarbons (PAHs), an important class of organic pollutants. The thickness of the insulating PMMA polymer has a significant impact on the strength of the plasmonic field. The role of the insulating PMMA interlayer is to prevent plasmon loss. Through understanding and optimization of the polymer thickness, the highest performing substrate was able to detect phenanthrene, an example PAH, at ppb concentrations.

*in revision, *ACS Applied Material and Interfaces*

4.2 Introduction

Raman spectroscopy is generally nondestructive and a non interfering analytical tool for qualitative and quantitative analysis of molecules. However, trace detection of a molecule is quite challenging by Raman, as it is a scattering method and hence produces low signal. [1] Discovery of surface enhanced Raman spectroscopy (SERS) has overcome this limitation. [2]

SERS has great potential in environmental pollution monitoring, as it can achieve trace detection of an analyte ranging from carcinogenic metals to organic pollutants. [3, 4] Polycyclic aromatic hydrocarbons (PAHs) are marked as serious environmental pollutants, even at low concentration, due to their carcinogenic effects. [5] The negative biological effects of phenanthrene, selected as an example PAH analyte, range from skin irritation, to initiation of tumors. [6]

SERS mechanism relies upon the collective oscillation of surface electrons of plasmonic materials. This collective oscillation, or plasmon, generates an electromagnetic field, which greatly increases the Raman signal by enhancing the polarizability change of an adsorbed analyte. [7–10] While not necessary, [11] the plasmon absorption wavelength (λ_{max}) should be comparable to that of the Raman laser in order to achieve maximum plasmonic enhancement. [12]

In this work, I used 830 nm as a good laser wavelength for analyte detection in order to avoid fluorescence interference produced by aromatic components such as phenanthrene. [13] Reaching 830 nm plasmonic absorption by metal nanoparticles is quite challenging, because Au and Ag films have their plasmon absorption between 400 and 500 nm. [14, 15] Gold-coated micro and nanostructures show red shifted plasmon absorption as a result of the confined oscillation of surface electrons at the grooves of the structured surface. [16, 17] Here I demonstrate that the dielectric properties of the supporting microstructures can also be used to control the Au plasmonic activ-

ity. In this study, I optimize the poly(methyl methacrylate) (PMMA) thickness in Au-PMMA-SiO_2 microstructures, achieving ppb-level detection of phenanthrene by SERS.

4.3 Experimental details

4.3.1 Materials

SiO_2 spheres of 750 nm diameter (Fiber Optics Center) were suspended in 2-butanone (99%, Sigma Aldrich). The PMMA layers were created from PMMA A2 (495 MW poly(methyl methacrylate) in 2% anisole, Micro Chem). Gold foil (99.9% metal basis) was acquired from Alfa Aesar for Au deposition. Ultrapure water (18.2 MΩ·cm, Barnstead) was used for all aqueous solutions. Phenanthrene (98+%, Aldrich) is the test PAH analyte. Glass microscope slides (Pearl, 1.0 mm-1.2 mm thick) form the base for the SERS substrate. These slides were cleaned by acid treatment and then washed with ultrapure water and air dried. The acid treatment involved cleaning glass slides sequentially with hot concentrated hydrochloric and sulfuric acids to eliminate organic and inorganic contamination.

4.3.2 Synthesis of SERS substrate

Various sample types are listed in Table 4.1.

Firstly, 750 nm SiO_2 spheres were oven dried and then 2-butanone solvent was added to make a 15% (by mass) suspension. Sonication (Fischer Scientific, FS20) for 3 hrs provided complete dispersion of spheres in the solvent. Dispersed spheres were spin coated (WS400, Laurell Technologies) on glass slides at 3000 rpm for 1 minute. A field emission scanning electron microscopy (FESEM) image of the sphere coated substrate is shown in Figure 4.1.

Table 4.1: List of SERS substrates. All consist of Au on PMMA on SiO_2 spheres on glass.

Sample tag	PMMA deposition speed (rpm)	Au thickness (nm)
A1	1000	15
A2	1000	25
A3	1000	35
B1	2500	15
B2	2500	25
B3	2500	35
C1	5000	15
C2	5000	25
C3	5000	35

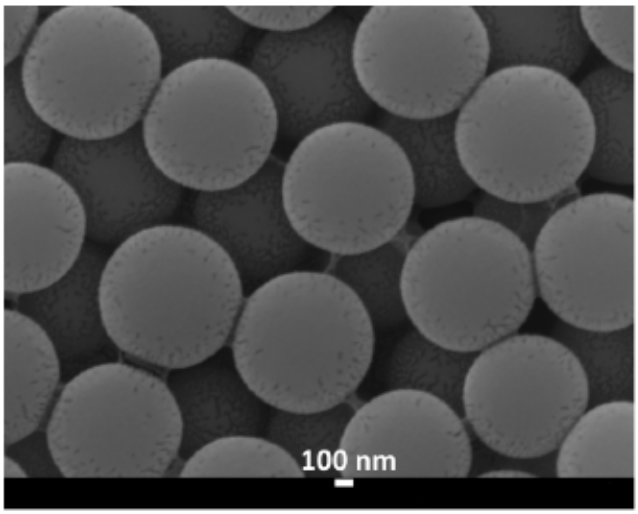

Figure 4.1: FESEM image of a sphere coated substrate.

PMMA was spin coated onto the spheres at 1000, 2500 or 5000 rpm for 1 minute. Higher spin speeds lead to thinner layers of PMMA on SiO_2 spheres. [18] 15, 25 or 35 nm of Au film were then deposited by thermal evaporation. The chamber in an in-house-built metal evaporator was maintained at a pressure of 10^{-4} torr during deposition; the Au foil was kept in a tungsten wire basket (Kurt J. Lesker). The metal thickness was monitored using a quartz crystal microbalance (INFICON XTM/2).

4.3.3 SERS measurement

1.07 mg of phenanthrene was dissolved in 1 Liter of ultrapure water to make the concentration 1 ppm. The whole solution was then sonicated for 4 hrs to promote complete dissolution of phenanthrene. SERS substrates were dipped into the 1 ppm of phenanthrene solution for 30 minutes. Then substrates were rinsed with ultrapure water and air dried. SERS spectra of the adsorbed phenanthrene on the substrate were recorded using a Renishaw inVia Raman microscope with 830 nm laser, equipped with a CCD detector and Leica microscope with 50× objective. 3 ± 0.3 mW laser power with a 40 seconds of exposure time was applied for each Raman measurement. The scan was performed on five different spots on each substrate.

The 710 cm^{-1} vibrational peak (C–C stretching, HCC bending) [19] was selected as a characteristic peak of phenanthrene for the enhancement factor calculation. The EF value is calculated by comparing the SERS intensity of 1 ppm and the normal Raman intensity of 0.1 M of phenanthrene. The different concentrations are accounted for as follows: [20]

$$\mathrm{EF} = \frac{\mathrm{I}_{SERS}}{\mathrm{C}_{SERS}} \times \frac{\mathrm{C}_{Normal}}{\mathrm{I}_{Normal}} \tag{4.1}$$

I_{SERS} and I_{Normal} are the intensities of the surface enhanced Raman mode and the normal Raman mode, respectively. C_{SERS} and C_{Normal} are the concentrations of analyte in the SERS experiment and the normal Raman experiment, respectively.

4.4 Results and discussion

4.4.1 SERS performance

The SERS substrates were tested for 1 ppm phenanthrene detection. Five major peaks of phenanthrene were notably enhanced: 410, 540, 710, 1350 and 1440 cm^{-1}. Figure 4.2 compares the normal Raman spectrum (glass slide substrate) to the SERS spectrum of sample A2. It is worth mentioning that the phenanthrene peak at 1440 cm^{-1}, which corresponds to the combined C–C stretching and C–H rocking mode, experienced a significant shift to 1425 cm^{-1} in the SERS spectrum. This shifting of the Raman peak to a lower wave number can be attributed to a charge transfer process between Au and phenanthrene. [21]

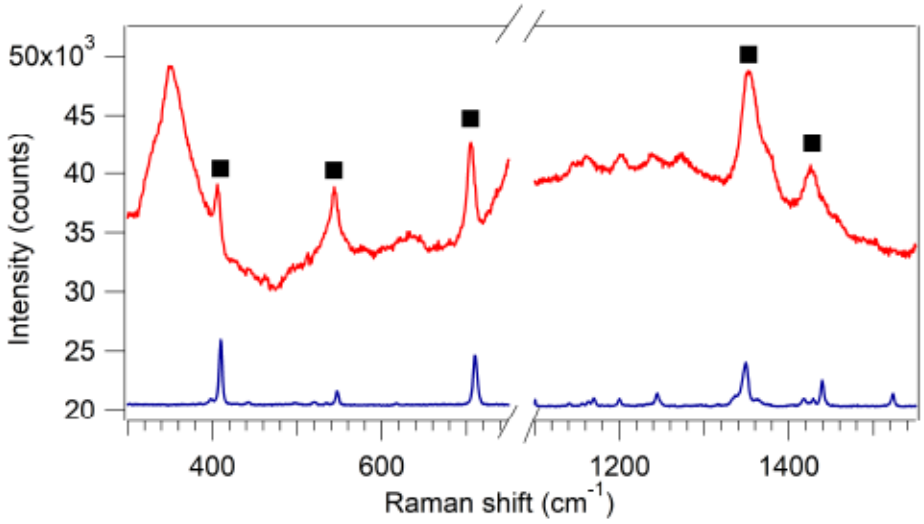

Figure 4.2: The SERS spectrum (red, 1 ppm phenanthrene solution on an A2 substrate) and the normal Raman spectrum (blue, 0.1 M phenanthrene solution on a glass slide). Graphs are offset for a clear view.

The enhancement of SERS substrates is significantly impacted by the thickness of the PMMA layer as well as the thickness of Au, as seen in Figure 4.3. Remarkably, a substrate with a thick PMMA layer (A2) provides just as much enhancement as a substrate with the thickest Au layer (C3). The different trends with PMMA thickness

for 25 nm thick Au layers *vs.* 35 nm thick Au layers is also quite striking, and it suggests different mechanisms are at play.

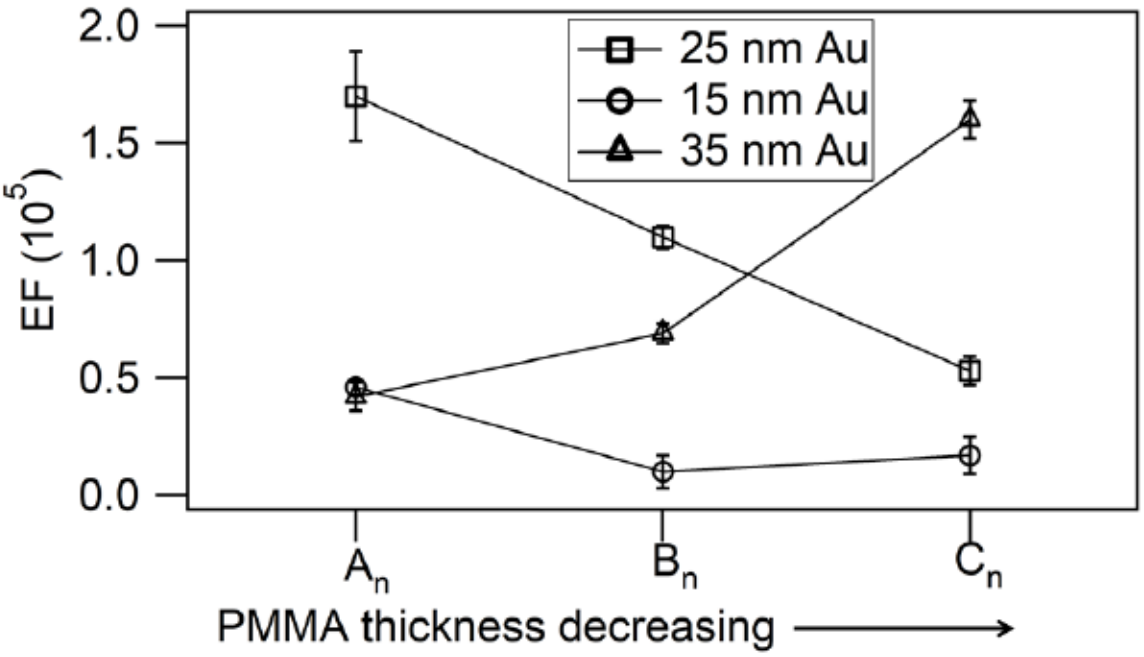

Figure 4.3: PMMA-thickness dependent SERS activity of substrates. The PMMA layer thickness decreases from left (A_n) to right (C_n). EFs of 15 and 25 nm thick Au layers decrease with decreasing PMMA thickness. In contrast, 35 nm thick Au layer shows opposite trend.

4.4.2 The role of the PMMA layer: a comparison between A_n, B_n, and C_n substrates

In reducing the thickness of the PMMA layer, most of the substrates showed lower SERS activity. For a Au layer on SiO_2, there is some probability that excited Au electrons can be injected into the SiO_2. This is called hot electron injection, which with these materials results in a reduction of the plasmonic field ("plasmon loss"). An additional, intermediate insulating layer (PMMA in this case) will reduce the probability of plasmon loss. [22] Therefore, varying the thickness of the polymer layer

has a major impact on the enhancement activity.

PMMA has a high dielectric constant ($\kappa = 3.15$) [23] compared to other organic polymers, because the extended delocalization of π electrons leads to an increase in polarizability. [24] SiO_2 has a similar dielectric constant to that of PMMA ($\kappa = 3.9$) [25], so one might think that the SiO_2 alone would also prevent hot electron injection and hence reduce plasmon loss. An earlier study reported that PMMA–SiO_2 has a higher dielectric constant compared to SiO_2 or PMMA alone, which supports the unique insulating property of PMMA-SiO_2 as an organic–inorganic hybrid dielectric material. [26] Another investigation confirmed that PMMA as an additive insulator on SiO_2 performed as a better gate dielectric material in electronics with lower leakage current. [27]

It is evident that the SERS performance for 15 and 25 nm of Au on PMMA covered SiO_2 is controlled by the thickness of the insulating (PMMA) layer. However, the 35 nm Au samples show the opposite trend (triangle in Figure 4.3): C_3 has the highest EF and A_3 has the lowest. This observation can be ascribed to the effect of the thickness of the Au layer, which diminishes the need for the PMMA layer to prevent plasmon loss. A previous theoretical study predicted that increasing the plasmonic metal thickness on a metal oxide layer suppresses hot electron injection from metal to metal oxide. [28] Hence, at a higher thickness of Au, plasmon loss becomes less significant. Surface roughness is the dominating factor in optimizing enhancement for the substrates with a 35 nm thick Au layer, as seen in Table C.1 in the appendix. (Surface roughness was measured using scanning probe microscopy and instrumental details in Appendix C.2.2.)

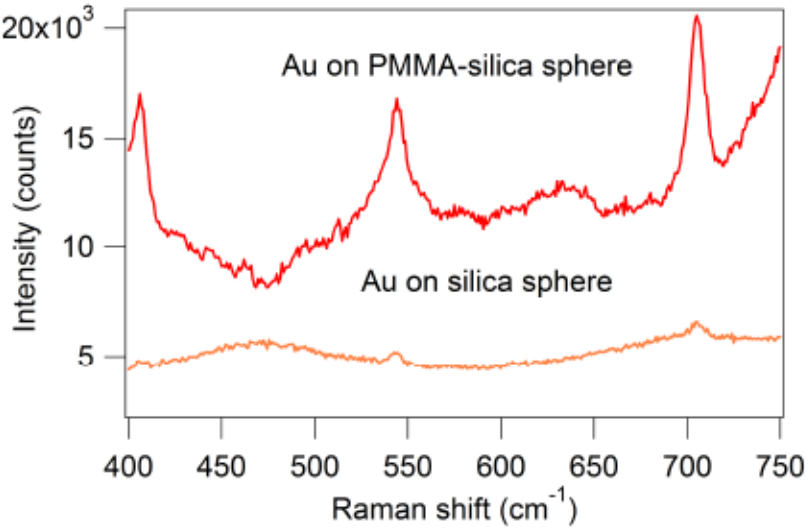

Figure 4.4: Poor SERS activity of 25 nm of Au on PMMA-free SiO_2 spheres compared to 25 nm of Au on PMMA-coated SiO_2 spheres. Spectra are offset for clarity.

Substrates without PMMA

A comparison of substrates with and without PMMA further confirms the importance of this insulating layer. A 25 nm Au film (the highest performing thickness) on SiO_2 spheres, without any PMMA interlayer, shows very poor SERS performance (Figure 4.4), which further supports the importance of PMMA layer on the plasmon loss. Note that no SERS activity was achieved with a thick Au layer on glass (the appendix, Figure A.6). Tests with PMMA-free, PMMA-coated SiO_2 sphere, and only PMMA substrates do not show any SERS activity either (the appendix, Figure C.2).

4.4.3 Detection at environmentally-relevant levels.

A2 was chosen to test lower analyte concentrations because of its highest enhancement factor. These analyte concentrations reach levels at which PAHs are present in Produced Water (PW), [29] a byproduct industrial water stream that is an important target for environmental monitoring. Figure 4.5 illustrates that the SERS activity, as measured at 710 cm^{-1} (the most intense characteristic peak of phenanthrene),

strongly depends on the analyte concentration. Our substrate is able to detect 0.001 ppm (1 ppb) or 10^{-9} M phenanthrene in aqueous solution, which is lower than the previously reported PAH detection limit by SERS. [29]

The consistent relation between the concentration of the analyte and the Raman intensity confirms the quantitative detection ability of SERS. One cannot expect a linear relationship between solution concentration and SERS signal over a wide range of concentrations. As explained in section 1.4.3, the SERS signal indicates the number of *adsorbed* analytes, a quantity which is not linearly related to their concentration in solution.

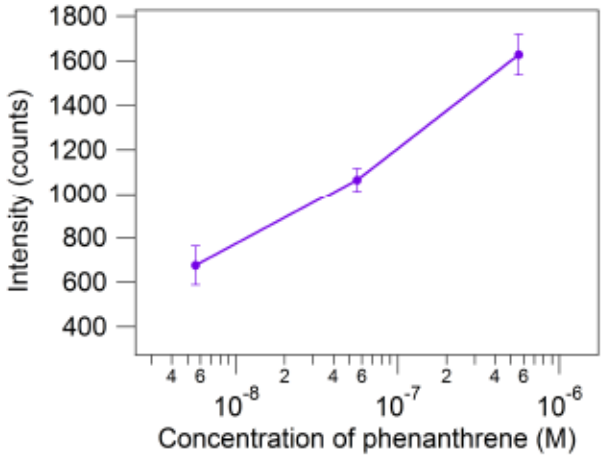

Figure 4.5: The Raman signal intensity increases with increasing phenanthrene concentration. The log-linear plot emphasizes the broad range of detectable concentrations.

4.5 Conclusions

A SERS substrate based on PMMA-coated SiO_2 spheres delivered the desired morphology and dielectric support for the plasmonic gold film, yielding significant Raman enhancement for adsorbed analytes. The presence of PMMA as an insulator layer led to an increase in the plasmonic field of the Au film by preventing plasmon loss to the

SiO_2 underlayer. This enabled the use of a thinner Au film which still obtaining a very high EF for detecting phenanthrene in water. Our most efficient substrate (25 nm of Au on thick PMMA on SiO_2 spheres) achieved an EF of 10^5 with ppb detection ability.

Bibliography

[1] Shuo Chen, Xiaoqian Lin, Clement Yuen, Saraswathi Padmanabhan, Roger W. Beuerman, and Quan Liu. Recovery of Raman spectra with low signal-to-noise ratio using Wiener estimation. *Opt. Express*, 22(10):12102, 2014.

[2] M. Fleischmann, P.J. Hendra, and A.J. McQuillan. Raman spectra of pyridine adsorbed at a silver electrode. *Chem. Phys. Lett.*, 26(2):163, 1974.

[3] Hai-Xin Gu, Kai Hu, Da-Wei Li, and Yi-Tao Long. SERS detection of polycyclic aromatic hydrocarbons using a bare gold nanoparticles coupled film system. *Analyst*, 141:4359, 2016.

[4] Jumin Hao, Mei-Juan Han, Songman Han, Xiaoguang Meng, Tsan-Liang Su, and Qingwu K. Wang. SERS detection of arsenic in water: A review. *J. Environ. Sci.*, 36:152, 2015.

[5] Jingli Mu, Juying Wang, Fei Jin, Xinhong Wang, and Huasheng Hong. Comparative embryotoxicity of phenanthrene and alkyl-phenanthrene to marine medaka (Oryzias melastigma). *Mar. Pollut. Bull.*, 85(2):505, 2014.

[6] Sudip K Samanta, Om V Singh, and Rakesh K Jain. Polycyclic aromatic hydrocarbons: environmental pollution and bioremediation. *Trends Biotechnol.*, 20(6):243, 2002.

[7] Sebastian Schlücker. Surface-Enhanced Raman Spectroscopy: Concepts and Chemical Applications. *Angew. Chem. Int. Ed.*, 53(19):4756, 2014.

[8] Bhavya Sharma, Renee R. Frontiera, Anne-Isabelle Henry, Emilie Ringe, and Richard P. Van Duyne. SERS: Materials, applications, and the future. *Mater. Today*, 15(1–2):16, 2012.

[9] Martin J. Mulvihill, Xing Yi Ling, Joel Henzie, and Peidong Yang. Anisotropic Etching of Silver Nanoparticles for Plasmonic Structures Capable of Single-Particle SERS. *J. Am. Chem. Soc.*, 132(1):268, 2010.

[10] Soumen Dutta, Chaiti Ray, Sougata Sarkar, Mukul Pradhan, Yuichi Negishi, and Tarasankar Pal. Silver Nanoparticle Decorated Reduced Graphene Oxide (rGO) Nanosheet: A Platform for SERS Based Low-Level Detection of Uranyl Ion. *ACS Appl. Mater. Interfaces*, 5(17):8724, 2013.

[11] Jian Ye, James Andell Hutchison, Hiroshi Uji-i, Johan Hofkens, Liesbet Lagae, Guido Maes, Gustaaf Borghs, and Pol Van Dorpe. Excitation wavelength dependent surface enhanced Raman scattering of 4-aminothiophenol on gold nanorings. *Nanoscale*, 4:1606, 2012.

[12] Fathima S. Ameer, Yadong Zhou, Shengli Zou, and Dongmao Zhang. Wavelength-Dependent Correlations between Ultraviolet–Visible Intensities and Surface Enhanced Raman Spectroscopic Enhancement Factors of Aggregated Gold and Silver Nanoparticles. *J. Phys. Chem. C*, 118(38):22234, 2014.

[13] Xiao-Ye Wang, Jie-Yu Wang, and Jian Pei. BN Heterosuperbenzenes: Synthesis and Properties. *Chem. Eur. J.*, 21(9):3528, 2015.

[14] El-Brolossy, T. A., Abdallah, T., Mohamed, M. B., Abdallah, S., Easawi, K., Negm, S., and Talaat, H. Shape and size dependence of the surface plasmon

resonance of gold nanoparticles studied by Photoacoustic technique. *Eur. Phys. J. Special Topics*, 153:361, 2008.

[15] Vincenzo Amendola, Osman M. Bakr, and Francesco Stellacci. A Study of the Surface Plasmon Resonance of Silver Nanoparticles by the Discrete Dipole Approximation Method: Effect of Shape, Size, Structure, and Assembly. *Plasmonics*, 5(1):85, 2010.

[16] Jia-Han Li, Shih-Wen Chen, Yi Chou, Ming-Chung Wu, Chun-Hway Hsueh, and Wei-Fang Su. Effects of Gold Film Morphology on Surface Plasmon Resonance Using Periodic P3HT:PMMA/Au Nanostructures on Silicon Substrate for Surface-Enhanced Raman Scattering. *J. Phys. Chem. C*, 115(49):24045, 2011.

[17] Scott K. Cushing, Lawrence A. Hornak, Jessica Lankford, Yuxin Liu, and Nianqiang Wu. Origin of localized surface plasmon resonances in thin silver film over nanosphere patterns. *Appl. Phys. A*, 103(4):955, 2011.

[18] S Niza Mohammad Bajuri, Nur Hamidah Abdul Halim, Mohammad Nuzaihan Md Nor, and Uda Hashim. PMMA characterization and optimization for nano structure formation. In *Proc. of 1st National Conference on Electronic Design*, page 81, 2005.

[19] A.I. Alajtal, H.G.M. Edwards, M.A. Elbagerma, and I.J. Scowen. The effect of laser wavelength on the Raman Spectra of phenanthrene, chrysene, and tetracene: Implications for extra-terrestrial detection of polyaromatic hydrocarbons. *Spectrochim. Acta Mol. Biomol. Spectrosc.*, 76(1):1, 2010.

[20] E. C. Le Ru, E. Blackie, M. Meyer, and P. G. Etchegoin. Surface Enhanced Raman Scattering Enhancement Factors: A Comprehensive Study. *J. Phys. Chem. C*, 111(37):13794, 2007.

[21] X. F. Wang, R. H. Liu, Z. Gui, Y. L. Xie, Y. J. Yan, J. J. Ying, X. G. Luo, and X. H. Chen. Superconductivity at 5 K in alkali-metal-doped phenanthrene. *Nat. Commun.*, 2:507, 2011.

[22] Hossein Shokri Kojori, Ju-Hyung Yun, Younghun Paik, Joondong Kim, Wayne A. Anderson, and Sung Jin Kim. Plasmon Field Effect Transistor for Plasmon to Electric Conversion and Amplification. *Nano Lett.*, 16(1):250, 2016.

[23] Moonkyong Na and Shi-Woo Rhee. Electronic characterization of Al/P-MMA[poly(methyl methacrylate)]/p-Si and Al/CEP(cyanoethyl pullulan)/p-Si structures. *Org. Electron.*, 7(4):205, 2006.

[24] M.D. Morales-Acosta, C.G. Alvarado-Beltrán, M.A. Quevedo-López, B.E. Gnade, A. Mendoza-Galván, and R. Ramírez-Bon. Adjustable structural, optical and dielectric characteristics in sol–gel PMMA–SiO_2 hybrid films. *J. Non-Cryst. Solids*, 362:124, 2013.

[25] Gorur Govinda Raju. *Dielectrics in electric fields.* CRC press, Boca Raton, 2016.

[26] M. D. Morales-Acosta, M. A. Quevedo-López, Bruce E. Gnade, and R. Ramírez-Bon. PMMA-SiO_2 organic–inorganic hybrid films: determination of dielectric characteristics. *J. Sol-Gel Sci. Technol.*, 58(1):218, 2011.

[27] Xiang Liu, Yu Bai, Wen-Qing Zhu, Xue-Yin Jing, and Zhi-Lin Zhang. Organic thin film transistors with PMMA modified insulator. *Optoelectron Lett.*, 3(6):435, 2007.

[28] Chathurangi S. Kumarasinghe, Malin Premaratne, Sarath D. Gunapala, and Govind P. Agrawal. Theoretical analysis of hot electron injection from metallic nanotubes into a semiconductor interface. *Phys. Chem. Chem. Phys.*, 18:18227, 2016.

[29] Hongyue Zhao, Jing Jin, Weijun Tian, Ran Li, Zhi Yu, Wei Song, Qian Cong, Bing Zhao, and Yukihiro Ozaki. Three-dimensional superhydrophobic surface-enhanced Raman spectroscopy substrate for sensitive detection of pollutants in real environments. *J. Mater. Chem. A*, 3:4330, 2015.

Chapter 5

Effect of ZnO Defects on SERS Activity of Au/ZnO Hybrid Films

5.1 Abstract

Different thicknesses of gold are deposited on triangular ZnO crystals, yielding surface enhanced Raman scattering (SERS)-active substrates (enhancement factors of 10^5), as tested by sensing ppm levels of phenanthrene in water. The Au coatings change both the structural and electronic properties of the ZnO film, as supported by a range of material characterization techniques.

5.2 Introduction

ZnO is a complex material. There are various ways to change the electronic structure of ZnO. The electronic band gap of ZnO can be tuned by varying the shape, size of crystals, and dopants. This tuning could be achieved with different synthetic parameters. [1] The use of capping agents, [2] varying the film thickness, [3] or tailoring

the nanostructure [4] can change the electronic properties of ZnO.

ZnO–metal hybrids are used as surface enhanced Raman scattering (SERS) substrates. [5–7] SERS is based on the enhancement of the Raman signal intensity of a molecule adsorbed onto or in the vicinity of a plasmonic metal surface. [8,9] The high plasmonic absorption by the SERS substrate at the Raman laser excitation wavelength generates an intense plasmonic electromagnetic field and, consequently, high SERS activity. [10, 11]

Changing the electronic structure of the ZnO can make a big difference in SERS activity, primarily through charge transfer between the ZnO and the plasmonic metal. [12] Surface charge on the metal coating arises from Fermi level equilibrium with the ZnO. [13, 14] Depending on the Fermi level of the ZnO, one can observe electron transfer from metal to ZnO [13] (as seen in Chapter 2) or ZnO to metal. [15]

Thiourea has been used to synthesize different shapes and sizes of ZnO crystals. [16] The size of ZnO nanoparticle can be varied with the concentration of thiourea in the photoelectrochemical deposition. [17] Thiourea can also generate nanoporous ZnO films. [18] The synthesis of different shapes and sizes of ZnO nanoparticles are gaining much attention. Triangular shaped ZnO crystals can be synthesized generally using a chemical approach, which includes the methanol solution process, [19] thermal decomposition, [20], and amine-mediated reaction [21].

This chapter presents a detailed analysis of the electronic structure of a defect-rich ZnO in a Au/ZnO SERS substrate. (SERS activity is measured through detection of phenanthrene, a molecule of environmental concern. [22]) I study several parameters which impact ZnO–metal interactions and hence SERS activity, including crystal structure, [23] defects [24] and local bonding [25] in the crystal, band gap and luminescence, [26] work function, [27] and surface charge [28–30]. I also contrast these results with those found in Chapter 2, which studies Au/ZnO SERS substrates prepared with

similar thicknesses of Au on a different type of ZnO.

5.3 Experimental

5.3.1 Materials

Zinc acetate dihydrate ($ZnOAc_2 \cdot 2H_2O$; ≥99.0%) was purchased from J. T. Baker. Sodium hydroxide (NaOH, 99.0%) and thiourea (CH_4N_2S, ≥99.0%) were obtained from Sigma-Aldrich. Ultrapure water (18.2 MΩ·cm, Barnstead) was used for all aqueous solutions and for rinsing. Gold (Au) wire (Alfa Aesar, 99.9% metal basis purity) was the source for metal film deposition. Phenanthrene (98+%) was acquired from Aldrich. Microscope glass slides (Pearl, 1.0 mm-1.2 mm thick) formed the support for the synthesized thin films. Glass slides were cut to 2×2 cm^2 before cleaning with hot concentrated hydrochloric acid and then hot concentrated sulfuric acid. Finally, slides were rinsed well with ultrapure water and then air dried.

5.3.2 Au/ZnO film synthesis

The sol-gel technique was used to synthesize triangular ZnO crystals, which then formed a thin film on the glass slide. [31] Solid thiourea was mixed with 100 ml of 0.10 M of aqueous solution of zinc acetate. Then 50 ml of 1.125 M NaOH aqueous solution was added to the zinc acetate-thiourea solution. Afterwards, the solution was stirred well, and then cleaned glass slides were immersed and left horizontally on the bottom of the container. The reaction mixture was heated to 40°C for 35 minutes. A turbid appearance in the reaction solution indicated formation of ZnO. Then, the reaction solution was cooled down to room temperature for 2 hours. A white film of ZnO formed on the glass slide, which was rinsed vigorously with ultrapure water and then air dried. 10, 20 or 30 nm-thick Au films were deposited on those ZnO

films by thermal vapor deposition. The metal evaporation was conducted with an in-lab built vacuum evaporator. ZnO-glass slides were attached to a circular plate and placed facing the molybdenum boat (Kurt J. Lesker) containing a Au wire. 10^{-4} torr pressure was maintained during deposition. A quartz crystal microbalance (QCM, INFICON XTM/2 deposition monitor) was utilized to monitor gold film thickness.

5.3.3 Characterization methods and instrumentation

X-ray diffraction (XRD) characterization of samples was done using the Rigaku Ultima-IV instrument with a Cu K-α source (at 40 kV and 44 mA). Field emission scanning electron microscopy (FESEM) images were taken using a JEOL Jsm-7100F equipped with a field emission source at 15 kV. Cathodoluminescence (CL) data was collected with JEOL JXA-8230 electron probe microanalyzer (EPMA) equipped with a tungsten filament.

Raman characterization of ZnO and Au/ZnO samples was carried out using the SERS parameters described below.

Optical absorption was conducted with an Ocean Optics USB 2000 spectrophotometer with the diffuse reflectance mode as described in the appendix, equation A.1. [32]

Electron paramagnetic resonance (EPR) spectra were obtained using a Magnettech MS 300 EPR spectrometer. All spectra were collected under ambient conditions, with 10 mg of sample held in a quartz tube.

X-ray photoelectron spectroscopy (XPS) was carried out on a ThermoVG Scientific Multilab 2000 (CTRI, Dalhousie University) with an Al source (1486.6 eV) operating at 14.6 kV and 20 mA. The energy scale was calibrated with the C1s peak. Each spectrum is an average of 6 scans.

Kelvin probe force microscopy (KPFM) was employed to determine surface rough-

ness and measure surface potential of substrates. KPFM was conducted using a MFP-3D (Asylum Research) atomic force microscope in KPFM mode. A Pt/Ti coated tip (Mikromasch, NSC35/Pt) with a resonance frequency of 130 kHz was used as the conductive probe. A scan size of 5×5 μm^2 was collected with 256 points per line over 256 lines at a 0.5 Hz scan rate. Five spots on each of the samples were scanned in order to address any sample heterogeneity. Surface roughness and surface potential were measured using 1 μm^2 masked areas (5 masked area per scan, so 25 masked area in total). Then an average value and standard deviation were calculated for each sample (masking procedure is described in Appendix A.7). The work function of the Pt/Ti tip was calibrated using highly ordered pyrolytic graphite (HOPG) as a reference ($\Phi = 4.6$ eV). [13]

Electrostatic force microscopy (EFM) was also conducted with the Pt/Ti coated tip on three Au/ZnO samples. EFM scans were performed at a tip-sample distance of 50 nm with three tip voltages (–3 V, 0 V and +3 V). At the distance of 50 nm, short range van der Waals forces are minimized, allowing for the extraction of the electrostatic interaction between the tip and the sample. [33] No voltage was applied on the sample; the Au surface possesses partial surface charge due to electron transfer at the Au/ZnO interfaces. Three locations on each Au covered ZnO sample were mapped. The phase shift ($\Delta\varphi$) was calculated using the following equation,

$$\Delta\varphi = \varphi_{bias} - \varphi_{0V} \tag{5.1}$$

A decrease in $\Delta\varphi$ indicates a repulsive electrostatic interaction between the tip and the sample, and an increase in $\Delta\varphi$ occurs due to an attractive interaction. [34]

5.3.4 SERS experiment

SERS sensing of phenanthrene was carried out with a Renishaw inVia Raman microscope equipped with a laser source (830 nm). Each Raman scan was collected with 3 ± 0.3 mW power, under a $50\times$ objective with an exposure time of 40 s. 1 ppm phenanthrene was prepared in ultrapure water and sonicated for 3 hours. A Au/ZnO SERS substrate was submerged into the 1 ppm solution for 30 minutes. The substrate was then removed, rinsed with ultrapure water, and air dried. Afterwards, Raman measurements were performed on the dried substrates.

5.4 Results and discussion

5.4.1 ZnO crystallite and film morphology

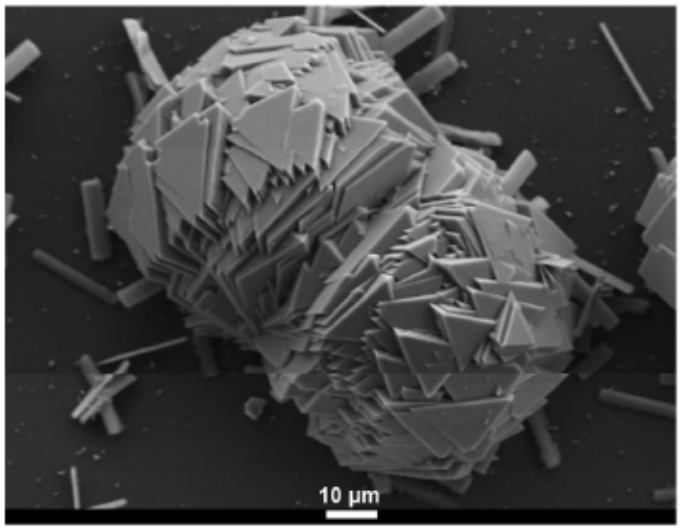

Figure 5.1: FESEM image of a ZnO film shows the packing of triangular crystals into a dumbbell-shaped cluster.

The FESEM image (Figure 5.1) of the ZnO film shows triangular microcrystals overlaying together to form large dumbbell shaped clusters. These individual clusters then form the film.

5.4.2 ZnO crystallographic analysis

XRD characterization of the ZnO film (red line in Figure 5.2) confirmed a wurtzite crystal structure. [31] The peak at 32.4° lies between the (100) peak for ZnO and the (211) peak for $Zn(OH)_2$ suggesting the possibility of some $Zn(OH)_2$ impurity. [35]

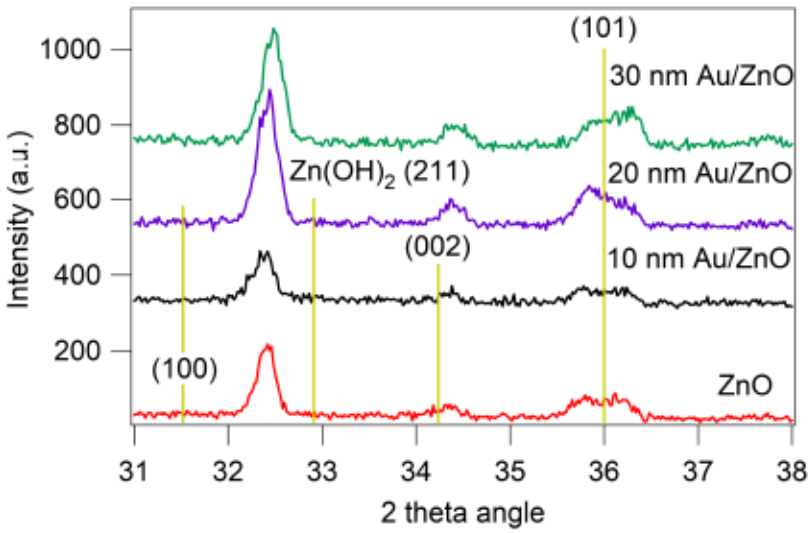

Figure 5.2: XRD data confirms the wurtzite crystal structure. Peak positions and peak widths change with the addition of a Au layer.

5.4.3 ZnO electronic structure

Fermi level and surface charge

The Fermi level equilibration at the Au/ZnO interface leads to electron transfer between Au and ZnO. [13] Due to a high Fermi level of Au relative to ZnO, electron transfer should occur from Au to ZnO. As a consequence, Au would carry a partial positive surface charge. With increasing the thickness of Au on ZnO, one would expect a higher degree of electron transfer and consequently a higher work function value of the Au surface (see Chapter 2). [13] However, in this case, I observed a different direction of electron transfer (Table 5.1).

EFM shows negative charge on Au, in contrast to the Au on the ZnO from Chapter 2 (Table 5.1). The phase shift ($\Delta\varphi$) is larger with a positive applied voltage (+3 V), indicating attraction, which implies a negative surface charge. Therefore, electron transfer occurs in the opposite direction in this Au/ZnO nanohybrid unlike the Au/ZnO substrates in Chapter 2. The EFM data for both chapters is compared in the appendix, Table D.2.

Table 5.1: EFM phase shift ($\Delta\varphi$) determines the surface charge of the gold surface on Au/ZnO substrate.

Au thickness on ZnO	$\Delta\varphi$ (+3 V)	$\Delta\varphi$ (–3 V)	Surface charge
10	7.36 ±1.30	3.23 ±0.40	Negative
20	4.15 ±0.85	1.07 ±0.21	Negative
30	6.91 ±0.76	2.91 ±0.98	Negative

The KPFM data confirmed the negative surface charge. Figure 5.3 shows a decrease of work function with increasing Au thickness on ZnO (red circles). Because the Au Fermi level doesn't change significantly (under same fabrication parameters), even with thin films and nanoparticles, [36] this electron transfer from ZnO to Au arises from a higher Fermi level of ZnO. A semiconductor's Fermi level is very sensitive to crystal shape and size, [4] and the ZnO crystallites in this chapter (see Figure 5.1) have a different size and shape than those in Chapter 2 (see Figure 2.1).

CL data also confirmed the negative surface charge formation on the Au surface of Au/ZnO substrates (Appendix, Figure D.7).

Fermi level and band gap

Optical measurements also point to differences in the electronic structure of the two types of ZnO, where the defect-rich ZnO produced here shows a smaller optical band gap than the ZnO from Chapter 2 (see Figure D.2 in the appendix). [37, 38] The smaller band gap arises from the higher Fermi level of this defect-rich ZnO when

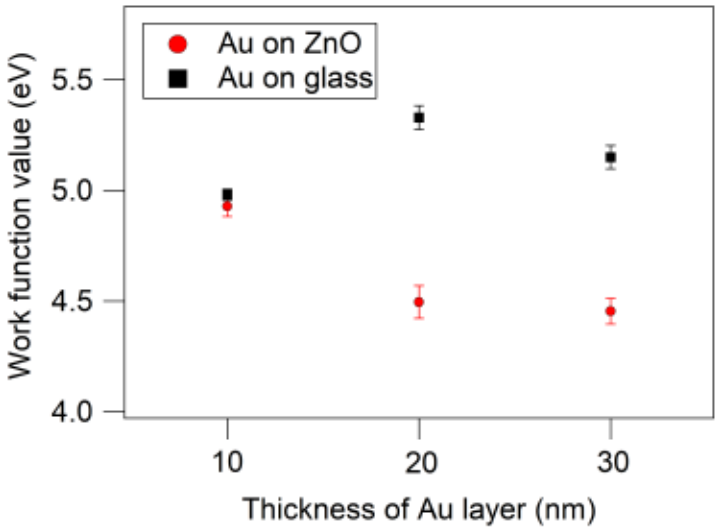

Figure 5.3: Work function of Au/ZnO vs Au/glass, shows negative surface charge formation on Au surface in Au/ZnO.

compared with that from Chapter 2.

5.4.4 SERS activity

Figure 5.4 depicts significant SERS performance of 20 and 30 nm of Au on ZnO, with enhancement factors (EFs) of 1.6×10^5 and 1.4×10^5, respectively, when measuring phenanthrene in an aqueous solution. The EF calculation was conducted by the analytical method (Appendix equation D.2). [39]

The 10 nm of Au on ZnO has a significantly smoother surface (see Figure D.5 in the appendix), which evidently is not sufficiently rough to generate hotspots. The film also shows lower plasmonic absorption than the other films at the laser excitation wavelength, as seen in Figure 5.5. [8] On the other hand, comparable SERS activity of 20 and 30 nm of Au on ZnO can be ascribed to a similar plasmonic absorption at the laser excitation wavelength.

Although a similar Au thickness dependent SERS activity is seen in Chapter 2, the EFs, which still high, are lower here. In Chapter 2 the positive surface charge

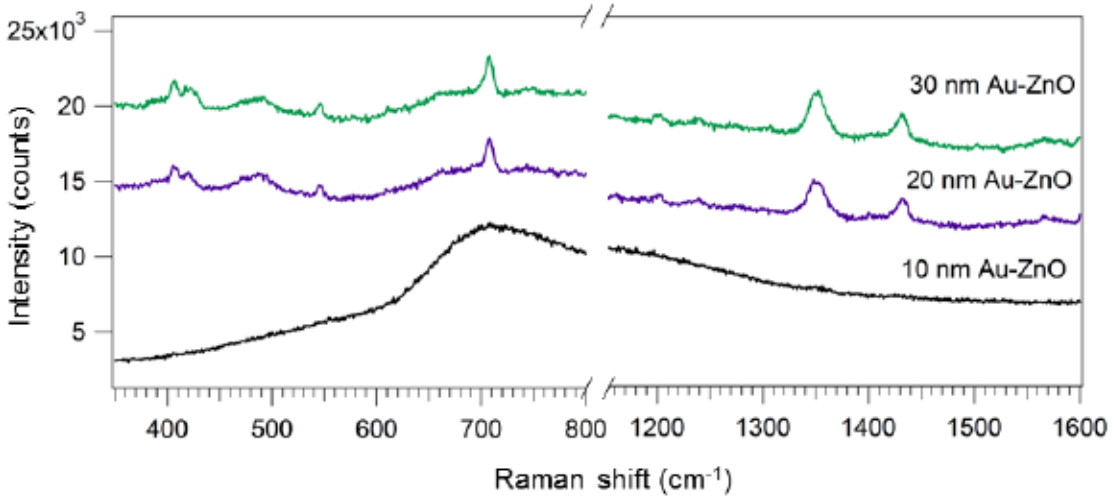

Figure 5.4: SERS activity of Au/ZnO substrates towards phenanthrene. 30 nm Au/ZnO and 20 nm Au/ZnO show considerable SERS activity of phenanthrene detection. 10 nm Au/ZnO is SERS inactive. Spectra are offset for clarity.

facilitates PAH adsorption through a Coulombic attraction, since PAHs are π electron-rich. [40] (Though nonpolar, PAHs have a quadrupole moment. [41]) The Au surfaces in these Au/ZnO nanohybrids are negatively charged, unlike in Chapter 2. Therefore, the EFs are lower than those in Chapter 2. I expect that these substrates will perform even better for positively-charged analytes. [42]

5.5 Conclusions

Defect-rich ZnO results in complex Au/ZnO hybrid films that show reverse electron transfer from ZnO to Au, forming a negative surface charge on the Au surface. This leads to lower EFs than in Chapter 2, but these SERS substrates should find application in sensing of positively-charged analytes, as their 10^5 EFs could be improved further through enhanced analyte adsorption.

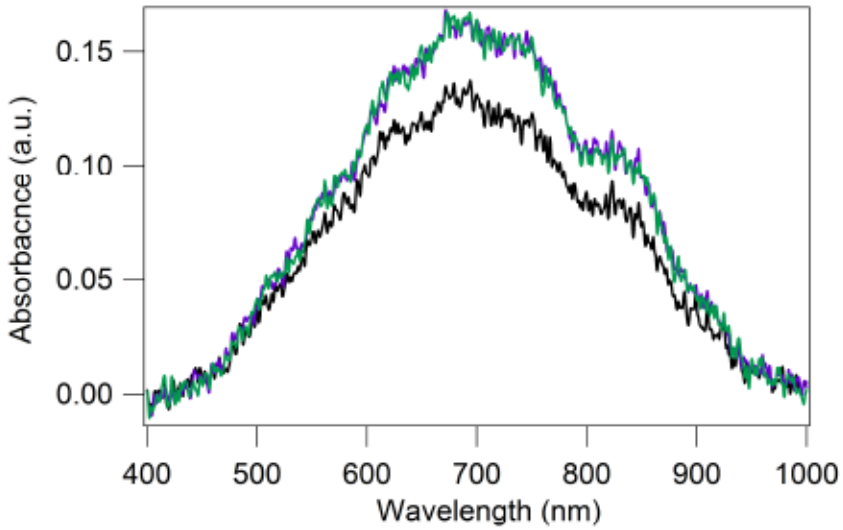

Figure 5.5: Plasmonic absorption spectra of 10 nm Au/ZnO (black), 20 nm Au/ZnO (violet) and 30 nm Au/ZnO (green). 10 nm of Au film on ZnO shows significantly lower plasmonic response at the laser excitation wavelength (830 nm).

Bibliography

[1] Aleksandra B. Djurišić and Yu Hang Leung. Optical Properties of ZnO Nanostructures. *Small*, 2(8-9):944, 2006.

[2] Shashi B. Rana, Vimal K. Bhardwaj, Satbir Singh, Amarpal Singh, and Navneet Kaur. Synthesis and optical characterization of ZnO nanoparticles capped with 2-aminothiols. *J. Mater. Sci. Mater. Electron.*, 24(1):20, 2013.

[3] R.E. Marotti, D.N. Guerra, C. Bello, G. Machado, and E.A. Dalchiele. Bandgap energy tuning of electrochemically grown ZnO thin films by thickness and electrodeposition potential. *Sol. Energy Mater Sol. Cells*, 82(1):85, 2004.

[4] Jianhui Zhang, Guanjun Dong, Aaron Thurber, Yayi Hou, Dmitri A. Tenne, Charles B. Hanna, Min Gu, Zhongda Pan, Kaiyu Wang, Youwei Du, and Alex Punnoose. Tuning the Bandgap and Cytotoxicity of ZnO by Tailoring the Nanostructures. *Part. Part. Syst. Char.*, 32(5):596, 2015.

[5] Gregory Barbillon, Vinod E. Sandana, Christophe Humbert, Benoit Belier, David J. Rogers, Ferechteh H. Teherani, Philippe Bove, Ryan McClintock, and Manijeh Razeghi. Study of Au coated ZnO nanoarrays for surface enhanced Raman scattering chemical sensing. *J. Mater. Chem. C*, 5:3528, 2017.

[6] Ping She, Kongliang Xu, Qinrong He, Shan Zeng, Hang Sun, and Zhenning Liu. Controlled preparation and visible light photocatalytic activities of corn cob-like Au–ZnO nanorods. *J. Mater. Sci.*, 52(6):3478, 2017.

[7] Anil Kumar Pal and D. Bharathi Mohan. Label free detection of DNA on Au/ZnO/Ag hybrid structure based SERS substrate. *AIP Conf. Proc.*, 1724(1):020101, 2016.

[8] Sebastian Schlücker. Surface-Enhanced Raman Spectroscopy: Concepts and Chemical Applications. *Angew. Chem. Int. Ed.*, 53(19):4756, 2014.

[9] Martin J. Mulvihill, Xing Yi Ling, Joel Henzie, and Peidong Yang. Anisotropic Etching of Silver Nanoparticles for Plasmonic Structures Capable of Single-Particle SERS. *J. Am. Chem. Soc.*, 132(1):268, 2010.

[10] N. M. B. Perney, F. J. García de Abajo, J. J. Baumberg, A. Tang, M. C. Netti, M. D. B. Charlton, and M. E. Zoorob. Tuning localized plasmon cavities for optimized surface-enhanced Raman scattering. *Phys. Rev. B*, 76:035426, 2007.

[11] Masahiko Shioi, Kristof Lodewijks, Liesbet Lagae, Tatsuro Kawamura, and Pol Van Dorpe. Tuning plasmonic interaction between gold nanorings and a gold film for surface enhanced Raman scattering. *Appl. Phys. Lett.*, 97(16):163106, 2010.

[12] Liping Liu, Haitao Yang, Xiao Ren, Jin Tang, Yongfeng Li, Xiangqun Zhang, and Zhaohua Cheng. Au-ZnO hybrid nanoparticles exhibiting strong charge-

transfer-induced SERS for recyclable SERS-active substrates. *Nanoscale*, 7:5147, 2015.

[13] Wan-Hsien Lin, Jih-Jen Wu, Mitch M. C. Chou, Yu-Ming Chang, and Masahiro Yoshimura. Charge Transfer in Au Nanoparticle–Nonpolar ZnO Photocatalysts Illustrated by Surface-Potential-Derived Three-Dimensional Band Diagram. *J. Phys. Chem. C*, 118(34):19814, 2014.

[14] M. Bieletzki, T. Hynninen, T. M. Soini, M. Pivetta, C. R. Henry, A. S. Foster, F. Esch, C. Barth, and U. Heiz. Topography and work function measurements of thin MgO(001) films on Ag(001) by nc-AFM and KPFM. *Phys. Chem. Chem. Phys.*, 12:3203, 2010.

[15] Yiqiang Sun, Bo Xu, Qi Shen, Lifeng Hang, Dandan Men, Tao Zhang, Huilin Li, Cuncheng Li, and Yue Li. Rapid and Efficient Self-Assembly of Au@ZnO Core–Shell Nanoparticle Arrays with an Enhanced and Tunable Plasmonic Absorption for Photoelectrochemical Hydrogen Generation. *ACS Appl. Mater. Interfaces*, 9(37):31897, 2017.

[16] Zhuo Wang, Xue feng Qian, Jie Yin, and Zi kang Zhu. Large-Scale Fabrication of Tower-like, Flower-like, and Tube-like ZnO Arrays by a Simple Chemical Solution Route. *Langmuir*, 20(8):3441, 2004.

[17] S. Gallanti, E. Chassaing, M. Bouttemy, A. Etcheberry, D. Lincot, and N. Naghavi. Photoelectrochemical deposition of ZnO films via nitrate ions reduction in the presence of thiourea on p-type Cu(In,Ga)Se2 semiconducting electrodes for photovoltaic applications. *J. Appl. Electrochem.*, 47(12):1283, 2017.

[18] S. Gallanti, E. Chassaing, D. Lincot, and N. Naghavi. Influence of thiourea addition on the electrodeposition of ZnO from zinc nitrate aqueous solutions. *Electrochim. Acta*, 178(Supplement C):225, 2015.

[19] Selin Pıravadılı Mucur, Tülay Aslı Tumay, Selçuk Birdoğan, Sait Eren San, and Emine Tekin. Triangular-shaped zinc oxide nanoparticles enhance the device performances of inverted OLEDs. *Nano-Structures & Nano-Objects*, 1(Supplement C):7, 2015.

[20] C.W. Yao, H.P. Wu, M.Y. Ge, L. Yang, Y.W. Zeng, Y.W. Wang, and J.Z. Jiang. Triangle-shape ZnO prepared by thermal decomposition. *Mater. Lett.*, 61(16):3416, 2007.

[21] Zhihua Zhang, Meihua Lu, Hairuo Xu, and Wee-Shong Chin. Shape-Controlled Synthesis of Zinc Oxide: A Simple Method for the Preparation of Metal Oxide Nanocrystals in Non-aqueous Medium. *Chem. Eur. J*, 13(2):632, 2007.

[22] Hussein I. Abdel-Shafy and Mona S.M. Mansour. A review on polycyclic aromatic hydrocarbons: Source, environmental impact, effect on human health and remediation. *Egypt. J. Pet.*, 25(1):107, 2016.

[23] Fatma Kayaci, Sesha Vempati, Inci Donmez, Necmi Biyikli, and Tamer Uyar. Role of zinc interstitials and oxygen vacancies of ZnO in photocatalysis: a bottom-up approach to control defect density. *Nanoscale*, 6:10224, 2014.

[24] Adersh Asok, Sougata Ghosh, Piyush A. More, Balu A. Chopade, Mayuri N. Gandhi, and Ajit R. Kulkarni. Surface defect rich ZnO quantum dots as antioxidants inhibiting α-amylase and α-glucosidase: a potential anti-diabetic nanomedicine. *J. Mater. Chem. B*, 3:4597, 2015.

[25] C Kranert, R Schmidt-Grund, and M Grundmann. Surface- and point-defect-related Raman scattering in wurtzite semiconductors excited above the band gap. *New J. Phys.*, 15(11):113048, 2013.

[26] Z. Q. Chen, S. Yamamoto, M. Maekawa, A. Kawasuso, X. L. Yuan, and T. Sekiguchi. Postgrowth annealing of defects in ZnO studied by positron annihilation, x-ray diffraction, Rutherford backscattering, cathodoluminescence, and Hall measurements. *J. Appl. Phys.*, 94(8):4807–4812, 2003.

[27] B. Eren, U. Gysin, L. Marot, Th. Glatzel, R. Steiner, and E. Meyer. Work function of few layer graphene covered nickel thin films measured with Kelvin probe force microscopy. *Appl. Phys. Lett.*, 108(4), 2016.

[28] Jinliang He, Chenlu Cheng, and Jun Hu. Electrical degradation of double-Schottky barrier in ZnO varistors. *AIP Advances*, 6(3):030701, 2016.

[29] P. M. Bridger, Z. Z. Bandić, E. C. Piquette, and T. C. McGill. Measurement of induced surface charges, contact potentials, and surface states in GaN by electric force microscopy. *Appl. Phys. Lett.*, 74(23):3522, 1999.

[30] Xiaodong Cui, Marcus Freitag, Richard Martel, Louis Brus, and Phaedon Avouris. Controlling Energy-Level Alignments at Carbon Nanotube/Au Contacts. *Nano Lett.*, 3(6):783, 2003.

[31] Ruth A. McBride, John M. Kelly, and Declan E. McCormack. Growth of well-defined ZnO microparticles by hydroxide ion hydrolysis of zinc salts. *J. Mater. Chem.*, 13:1196, 2003.

[32] James H Nobbs. Kubelka-Munk Theory and the Prediction of Reflectance. *Rev. Prog. Color. Relat. Top.*, 15(1):66, 1985.

[33] Paul Girard. Electrostatic force microscopy: principles and some applications to semiconductors. *Nanotechnology*, 12(4):485, 2001.

[34] Sibel Ebru Yalcin, Joelle A. Labastide, Danielle L. Sowle, and Michael D. Barnes. Spectral Properties of Multiply Charged Semiconductor Quantum Dots. *Nano Lett.*, 11(10):4425, 2011.

[35] A. S. Shaporev, V. K. Ivanov, A. E. Baranchikov, O. S. Polezhaeva, and Yu. D. Tret'yakov. ZnO formation under hydrothermal conditions from zinc hydroxide compounds with various chemical histories. *Russ. J. Inorg. Chem.*, 52(12):1811, 2007.

[36] Antoine Kahn. Fermi level, work function and vacuum level. *Mater. Horiz.*, 3:7, 2016.

[37] N.L. Tarwal, R.S. Devan, Y.R. Ma, R.S. Patil, M.M. Karanjkar, and P.S. Patil. Spray deposited localized surface plasmonic Au–ZnO nanocomposites for solar cell application. *Electrochim. Acta*, 72:32, 2012.

[38] N. Naseri, R. Azimirad, O. Akhavan, and A.Z. Moshfegh. Improved electrochromical properties of sol–gel WO_3 thin films by doping gold nanocrystals. *Thin Solid Films*, 518(8):2250, 2010.

[39] E. C. Le Ru, E. Blackie, M. Meyer, and P. G. Etchegoin. Surface Enhanced Raman Scattering Enhancement Factors: A Comprehensive Study. *J. Phys. Chem. C*, 111(37):13794, 2007.

[40] Shuichi Hashimoto, Sigeru Ikuta, Tsuyoshi Asahi, and Hiroshi Masuhara. Fluorescence Spectroscopic Studies of Anthracene Adsorbed into Zeolites: From the Detection of Cation$-\pi$ Interaction to the Observation of Dimers and Crystals. *Langmuir*, 14(15):4284, 1998.

[41] Kwan Ming Ng, Ngai Ling Ma, and Chun Wai Tsang. Cation–aromatic π interaction in the gas phase: an experimental study on relative silver (I) ion affinities of polyaromatic hydrocarbons. *Rapid Commun Mass Spectrom*, 12(22):1679, 1998.

[42] Meikun Fan, Feng-Ju Lai, Hung-Lung Chou, Wan-Ting Lu, Bing-Joe Hwang, and Alexandre G. Brolo. Surface-enhanced Raman scattering (SERS) from Au:Ag bimetallic nanoparticles: the effect of the molecular probe. *Chem. Sci.*, 4:509, 2013.

Chapter 6

Direct Evidence of Surface Charge Controlled SERS Activity in a Bilayer Metal Film by EFM*

6.1 Abstract

Electron transfer in a bilayer metal film generates a surface charge, and thus affects the surface plasmonic enhancement response. This surface charge can induce adsorption of an analyte molecule by electrostatic interactions. In this report, surface charge is mapped in Ag-Au and Au-Ag bimetallic films supported on a dielectric, studying the impact of surface charge on SERS sensing of pyrene, a serious environmental pollutant. Electrostatic force microscopy is employed to determine the surface charge formation. This force microscopy scan also yields the morphological features of the film. This new approach to the study of surface charge mediated Raman enhancement enables the optimization of the films, leading to an enhancement factor of 10^5 for the

*In re-submission for *Nanoscale*

detection of the pyrene molecule in aqueous solution.

6.2 Introduction

Bilayer metallic films carry a surface charge as a result of Fermi level equilibrium at the metal-metal interface. For the case of Ag and Au, Ag possesses a partial positive surface charge, and Au gains a negative surface charge, because Ag has a higher Fermi level compared to Au. [1] The surface plasmon electromagnetic field is surface charge sensitive. [2, 3] Plasmon absorption tuning with the variation of Au:Ag proportion in a Ag-Au bilayer system impacts SERS activity. [4] As a result, bimetallic Ag-Au systems have been employed for charge-selective SERS sensing. [5]

Surface charge can have the further benefit of enhancing adsorption of analytes for SERS detection. [6] PAHs often need that additional drive for adsorption, [7] and they are of particular interest for trace detection in water because of their carcinogenicity. [8] While functionalized [9, 10] or hydrophobic [7] substrates help to enhance adsorption and hence SERS signal, this chapter presents a simpler approach based on surface charge alone. Earlier report suggested that cation-π interaction can lead to increase the adsorption of PAHs on the surface with the cationic charge. [11]

Here I show a new application of electrostatic force microscopy (EFM) to quantify surface charge, and its impact on SERS mechanisms. EFM determines the electrical property of a material surface by measuring the surface charge density. [12] In the EFM scan, a biased tip electrically interacts with the charged sample surface. In tapping mode EFM, a phase shift occurs because of the electrostatic interaction between the sample surface and the tip. At the sub-nanometer gap between the tip and the sample surface, the van der Waals force dominates. However, at a greater distance (generally, above 40 nm) the van der Waals force between the tip and the sample surface is

negligible, and here one can measure other forces. For example, electrostatic forces arise from an electrically biased tip over an electrically charged sample surface. [13] This method has already been applied to a range of systems, including quantum dots, [14] charged spheres, [15] and even dielectric materials. [16]

6.3 Experimental procedure

6.3.1 Materials

Suspension of 750 nm diameter SiO_2 spheres (Fiber Optics Center Inc.) was made with 2-butanone (99%, Sigma Aldrich) as a solvent. The PMMA layers were developed using "PMMA A2" (495 MW poly(methyl methacrylate) in 2% anisole, Micro Chem). Gold wire (99.9% metal basis) and silver shot (99.9% metal basis) were both acquired from Alfa Aesar. Pyrene (95%) was obtained from Aldrich. Microscope glass slides (1.0 mm-1.2 mm thick) were obtained from Pearl. Glass slides were cut into 2×2 cm^2 size. Glass slides were cleaned in hot concentrated sulfuric and hot hydrochloric acid, and then washed with ultrapure water.

6.3.2 Synthesis of SERS substrate

A bimetallic film was deposited on a PMMA/SiO_2 dielectric support which has previously been shown to promote SERS activity (see Chapter 4). 750 nm of SiO_2 spheres were air dried in an oven and then 2-butanone solvent was added to make the concentration of 15%. Then the sphere suspension was sonicated for several hours for complete dispersion. Afterwards, this sonicated suspension was spin coated on clean glass slides. Next, a polymer (PMMA A2) was spin coated on the spheres. Then 15 nm Ag and/or Au were deposited as in Table 6.1. To test for consistency, analogous

samples with 25 nm thick metal layers were prepared; that data is found in Appendix E.

Table 6.1: List of monometallic and bilayer metallic SERS substrates

Sample tag	Sample description
M1	15 nm Ag
M2	15 nm Au
B1	15 nm Ag on 15 nm Au
B2	15 nm Au on 15 nm Ag

Metal deposition was performed using an in-laboratory-built thermal metal evaporator. Metal evaporation was carried out with a molybdenum boat (Kurt J. Lesker) and with a pressure of 10^{-4} torr inside the evaporator chamber. Metal thickness was controlled by a quartz crystal microbalance with a deposition monitor (INFICON XTM/2). Each sample type was prepared two times over.

6.3.3 Characterization methods

Electrostatic force microscopy

MFP-3D AFM (Asylum Research) was employed for conducting the EFM scan. All measurements were made in ambient conditions. EFM was performed using a Au-coated conductive tip (Mikromasch, NSC35/Cr-Au, nominal resonant frequency of 147 kHz). A conductive holder (ORCA, Asylum Research) was used to control the electrical interaction between the sample and the tip.

An EFM scan involves first approaching the tip to the surface while monitoring the amplitude of the oscillating tip. When the amplitude is damped by a preset amount (70%), a stable tip-surface interaction is established. After each scan line of the surface topography, the tip is raised above the surface to minimize the short range van der Waals forces. A bias is applied to the tip relative to ground, and an EFM

scan of that same line is performed at constant tip-sample separation. The resultant data set ("image") maps height, amplitude, and phase for the oscillating tip.

Each scan covered a 5×5 μm^2 area with 256 points per line, 256 lines, at a scan rate of 0.5 Hz. For each line, after acquiring an appropriate surface topography scan, the tip was lifted to a height of 50 nm above the sample surface. At that specific height, the tip was biased, and then it retraced the topography of the line to maintain a 50 nm distance throughout the scan.

The phase shift ($\Delta\varphi$) due to the applied voltage was calculated through the subtraction of the phase data at 0 V from the phase data at 3 V or –3 V:

$$\Delta\varphi = \varphi_{bias} - \varphi_{0V} \tag{6.1}$$

$\Delta\varphi$ as defined in equation 6.1 is always positive: whether attractive or repulsive, the electrostatic interaction between tip and sample always leads to damping. An attractive force has a higher phase shift than a repulsive interaction. [17] It was observed higher voltage (3 V or –3 V) has high phase response compared to other voltages (Figure 6.1). Therefore, 3 V or –3 V was employed to determine surface charge of bimetallic film.

In order to optimized the tip voltage to achieve charge sensitive phase response, several applied voltages were also compared (1 V, 2 V, 3V, –1 V, or –2 V, –3V) to a bimetallic sample. A large enough voltage must be applied so that electrostatic interactions dominate the phase shift. Otherwise, contributors to phase shift such as van der Waals and other non-polar interactions may arise in the phase map.

EFM scans were performed on three locations of each duplicate sample. Three scans were performed at each location, with the tip biased at 0 V, 3 V, or –3 V with respect to ground. It is worth mentioning that the bias was applied to the tip, and no

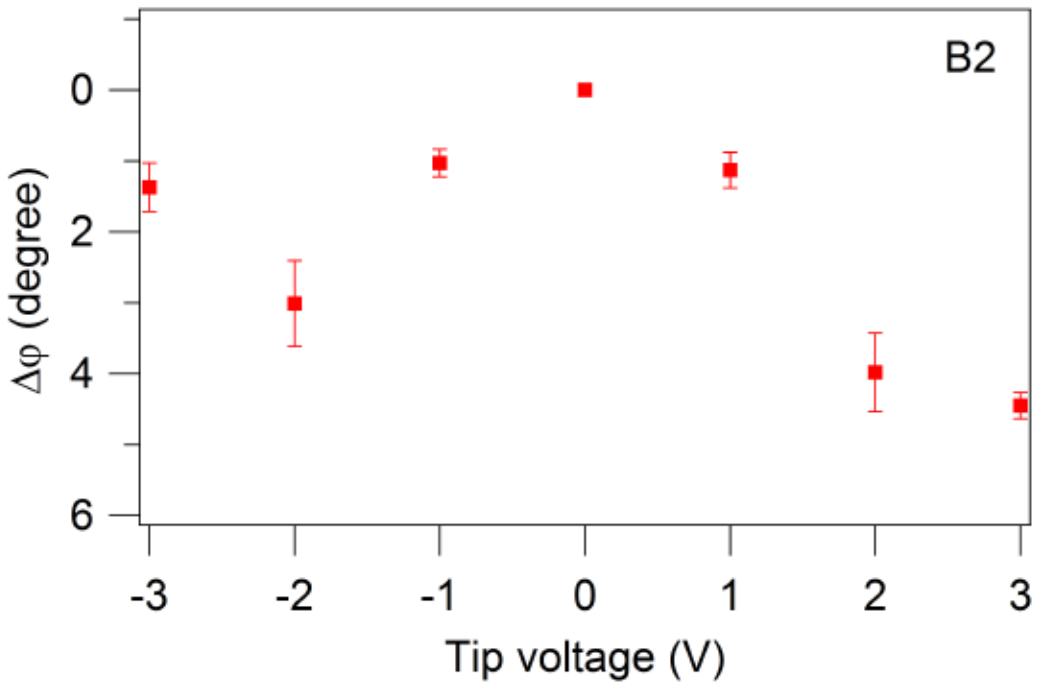

Figure 6.1: Phase shift differences between 3 V and –3 V is highest compared to 2 V/–2 V and 1 V/–1 V revealing higher voltage can lead to higher amount of tip-sample Coulombic interaction to determine surface charge more accurately.

bias was applied to the sample. The bilayer films have an inherently charged surface due to Fermi level equilibration, [5] which is absent in monometallic films.

SERS experiment

0.1 mg of pyrene crystals were dissolved in ultrapure water to make a 0.1 ppm solution. The ultrapure water was obtained from a Barnstead purifier with a resistivity of 18.2 MΩ·cm. The solution was sonicated (Fischer Scientific, FS20) to promote complete dissolution of the analyte. Metal SERS substrates were dipped into the analyte solution for 30 minutes and then washed with ultrapure water and air dried. Five Raman scans were performed on each substrate on different spots, using a Renishaw inVia Raman spectrometer coupled to a Leica microscope. Each spectrum was acquired using 830 nm excitation, a 50× objective, and a 40 s exposure at 3 ±0.3 mW.

6.4 Results and discussion

6.4.1 SERS study

A silver film alone (sample M1) on the polymer/sphere substrate shows poor SERS activity toward the detection of pyrene, while a gold film (M2) exhibits notable SERS activity (Figure 6.2). One contributor could be the different electronic interactions between the analyte and the metals. Benzene, a molecule similar to the analyte, and Ag interactions are from dispersion, while benzene binds with Au through a charge transfer interaction. [18] Hence, one can expect that polycyclic aromatic hydrocarbons should also undergo charge transfer interaction with Au, which impacts the polarizability of the analyte [19] and consequently the SERS response (see equation 1.8).

The different SERS activity of M1 and M2 can further be explained by the different surface morphologies of these films. The Au film (M2) has a higher surface area than the Ag film (M1), but the additional analyte adsorption sites on a higher surface area film cannot explain the entire 10^2 enhancement of M2 over M1 (Table 6.2). M2 also has substantially higher roughness that can lead to hotspot formation [20] and hence significantly higher enhancement. The detailed morphological analysis of the monometallic films is given in the appendix, Table E.1, with additional confirmation in Figure E.1, a plot showing the relationship between roughness and EF for a wider range of monometallic samples.

Figure 6.3 shows the Raman enhancement of different bimetallic combinations, where it can be seen that B1 (silver on top) has notable SERS activity, while B2 is SERS inactive. The enhancement factor calculations were performed using equation as below, [21]

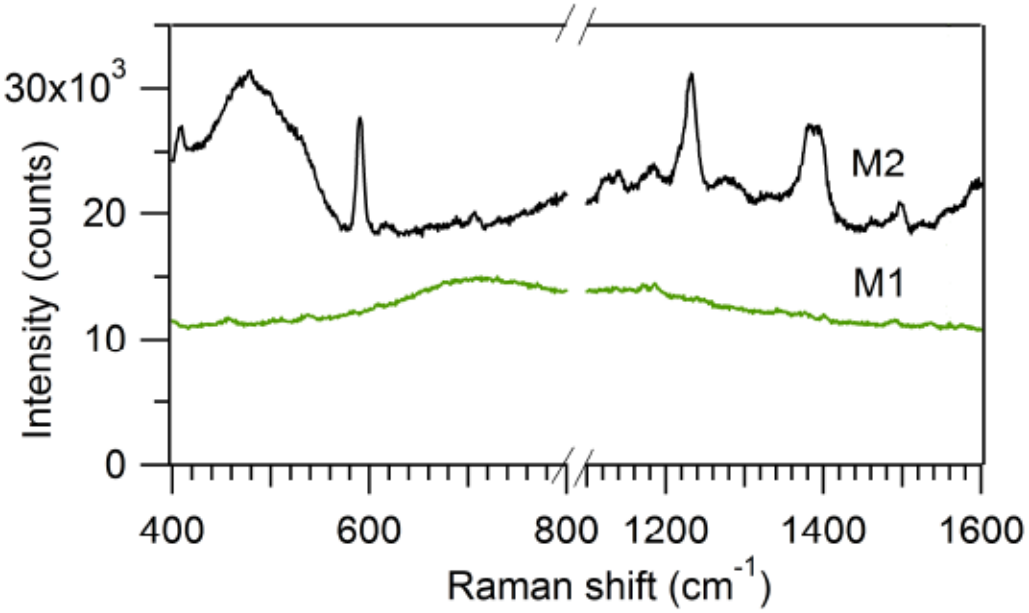

Figure 6.2: SERS response of pyrene with Au (black) and Ag (green). In this case, monometallic Au has higher SERS activity than Ag. Spectra are offset for clarity.

$$\mathrm{EF} = \frac{\mathrm{I}_{SERS}}{\mathrm{C}_{SERS}} \times \frac{\mathrm{C}_{Normal}}{\mathrm{I}_{Normal}} \tag{6.2}$$

I_{SERS} and I_{Normal} are the intensity of the surface enhanced Raman mode and the intensity of the normal Raman mode, respectively. C_{SERS} and C_{Normal} are the concentration of the analyte in SERS experiment and the concentration of the analyte in the normal Raman experiment (0.1 M), respectively. The normal Raman experiment was conducted with the PMMA-SiO_2 substrate (without a metallic layer).

For pyrene, 1395 cm^{-1} mode (C-C stretching) was selected for EF calculation. It is worth noting that 1395 cm^{-1} mode shifted on Ag-Au substrate (B1), which can be ascribed to the binding interaction between analyte and the surface charge of Ag. [5, 22, 23] Table 6.2 shows the comparison of EFs of different monometallic and bimetallic substrates.

Table 6.2: EF of monometallic and bimetallic films for pyrene sensing

Sample tag	EF ($\times 10^5$)
M1	0.09 ± 0.06
M2	1.75 ± 0.18
B1	1.95 ± 0.08
B2	not detectable

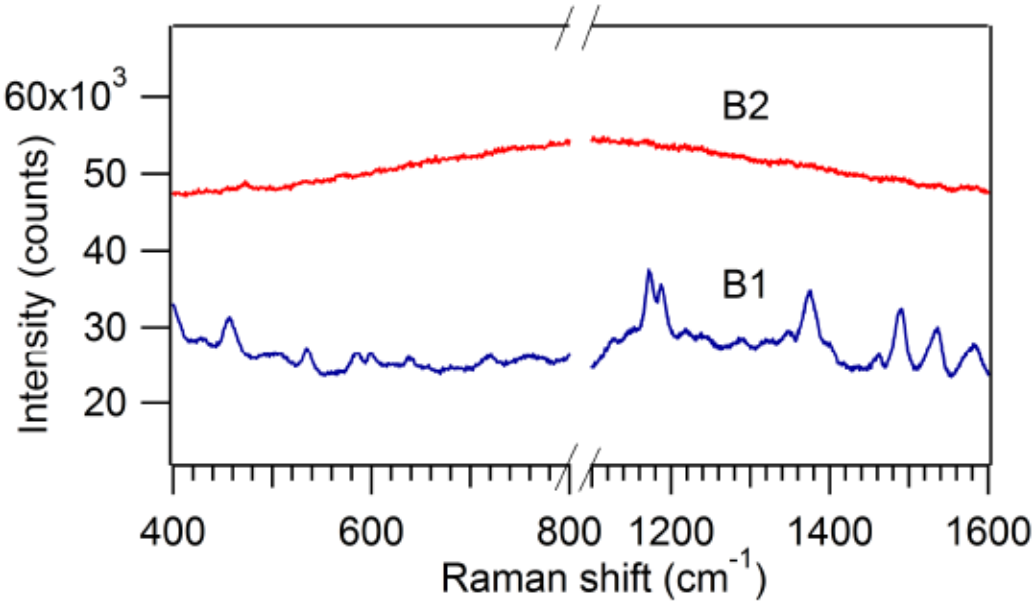

Figure 6.3: SERS response of pyrene with Ag on top of Au (B1, blue) and Au on top of Ag (B2, red). Ag on top of Au demonstrates high SERS activity relative to Au on Ag. Spectra are offset for clarity.

6.4.2 EFM study

Surface charge determination by EFM

Typical $\Delta\varphi$ images of the system with Ag on top of Au (B1) are shown in Figure 6.4. The average and standard deviation of all pixels in an image yields one $\Delta\varphi$ point in graphs such as Figure 6.5.

The bilayer system with Ag on top (B1) shows a higher $\Delta\varphi$ with a negative tip voltage of –3 V, indicating an attractive interaction. Similarly, the smaller $\Delta\varphi$ with the tip at a positive voltage of 3 V meaning a repulsive interaction. Thus, a positive

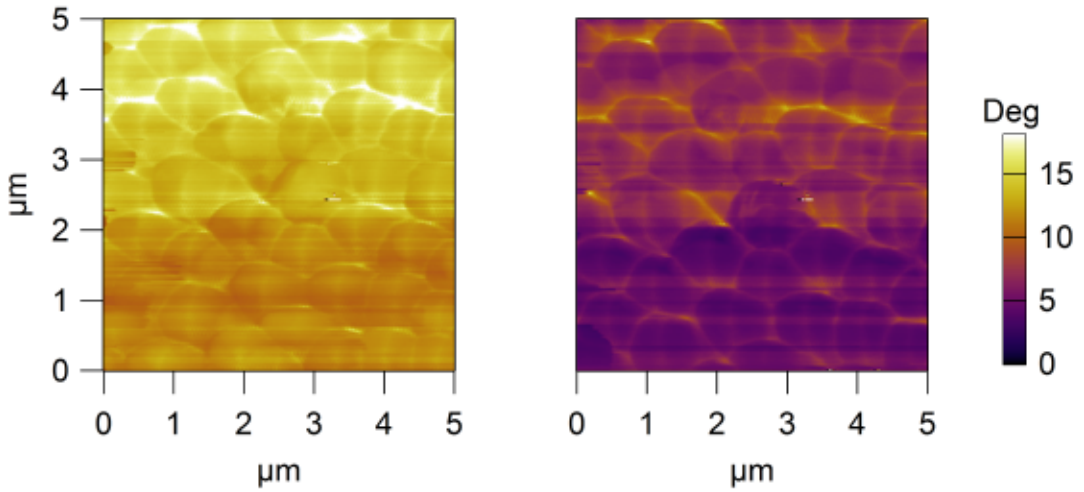

Figure 6.4: Phase shift of Ag on Au system (B1). Phase shifts from –3 V (left) and 3 V (right).

surface charge can be ascribed to B1, the sample with Ag on top.

An opposite situation in $\Delta\varphi$ is seen in the case of B2 (Au as a top layer). Since the positively biased tip generated a larger phase shift, that bias must produce attraction, meaning that there is a negative surface charge when the Au layer is on top. This is consistent with Au having a lower Fermi energy than Ag. [1]

EFM data showed no significant change in $\Delta\varphi$ (Figure 6.6) upon changing the tip bias over the Ag or Au films. This indicates that no surface charge forms on the monometallic film. This is not surprising, given that the sample is not biased and there is no inherent charge formation from inter-layer electron transfer in the monometallic films.

The results here are consistent over two replicate samples made in separate batches. These results apply for other thicknesses of metal as well. The relationship between surface charge and SERS activity for all thicknesses is shown in the appendix, Table E.2.

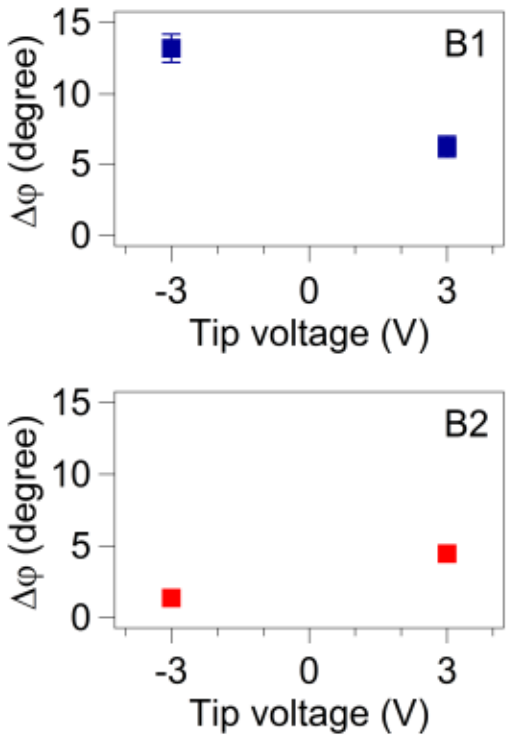

Figure 6.5: Phase shift ($\Delta\varphi$) of Ag on Au (B1, top) and Au on Ag (B2, bottom). This data indicates a positive surface charge with Ag on top and a negative surface charge for Au as the top layer in the bilayer metallic films. In some cases, the error bars are smaller than the symbol.

6.5 Conclusions

In this study I explored how a metallic bilayer can dramatically change the SERS activity of the top metallic film. As a consequence of the electron transfer in the bimetallic Ag-Au system, the Ag surface gained a partial positive charge. Therefore, Ag as a top layer in the Ag-Au system performed better as a SERS active substrate for a PAH analyte due to attractive metal–molecule interactions. The electrostatic force microscopy revealed the different surface charge in the bimetallic system. EFM scans also illustrated the surface morphology of substrates.

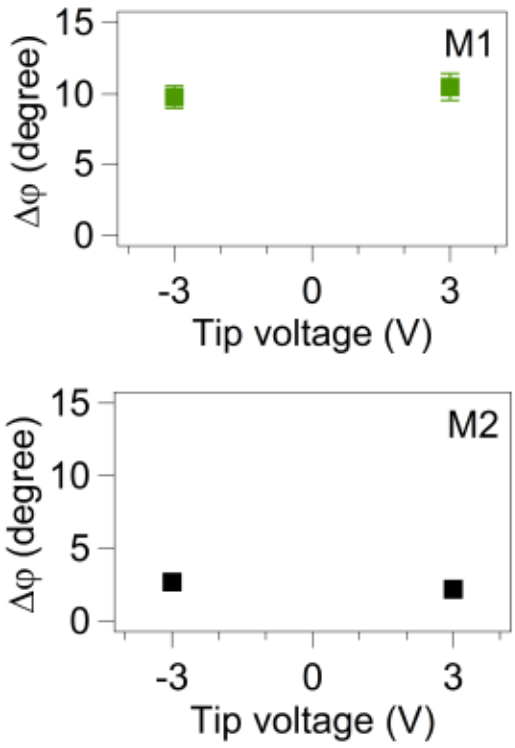

Figure 6.6: Phase shift of Ag film (M1, top) and Au film (M2, bottom). No considerable deviation of $\Delta\varphi$ between +3 V and –3 V, which supports a neutral surface charge on the monometallic films. The error bars are smaller than the symbol.

Bibliography

[1] Pekka Peljo, José A. Manzanares, and Hubert H. Girault. Contact Potentials, Fermi Level Equilibration, and Surface Charging. *Langmuir*, 32(23):5765, 2016.

[2] Jean Lermé. Size Evolution of the Surface Plasmon Resonance Damping in Silver Nanoparticles: Confinement and Dielectric Effects. *J. Phys. Chem. C*, 115(29):14098, 2011.

[3] Jean Lermé, Hatim Baida, Christophe Bonnet, Michel Broyer, Emmanuel Cottancin, Aurélien Crut, Paolo Maioli, Natalia Del Fatti, Fabrice Vallée, and Michel Pellarin. Size Dependence of the Surface Plasmon Resonance Damping in Metal Nanospheres. *J. Phys. Chem. Lett.*, 1(19):2922, 2010.

[4] M. Vinod and K.G. Gopchandran. Au, Ag and Au:Ag colloidal nanoparticles synthesized by pulsed laser ablation as SERS substrates. *Prog. Nat. Sci.: Materials International*, 24(6):569, 2014.

[5] Meikun Fan, Feng-Ju Lai, Hung-Lung Chou, Wan-Ting Lu, Bing-Joe Hwang, and Alexandre G. Brolo. Surface-enhanced Raman scattering (SERS) from Au:Ag bimetallic nanoparticles: the effect of the molecular probe. *Chem. Sci.*, 4:509, 2013.

[6] Limei Tian, Sirimuvva Tadepalli, Mikella E. Farrell, Keng-Ku Liu, Naveen Gandra, Paul M. Pellegrino, and Srikanth Singamaneni. Multiplexed charge-selective surface enhanced Raman scattering based on plasmonic calligraphy. *J. Mater. Chem. C*, 2:5438, 2014.

[7] Hongyue Zhao, Jing Jin, Weijun Tian, Ran Li, Zhi Yu, Wei Song, Qian Cong, Bing Zhao, and Yukihiro Ozaki. Three-dimensional superhydrophobic surface-enhanced Raman spectroscopy substrate for sensitive detection of pollutants in real environments. *J. Mater. Chem. A*, 3:4330, 2015.

[8] Hussein I. Abdel-Shafy and Mona S.M. Mansour. A review on polycyclic aromatic hydrocarbons: Source, environmental impact, effect on human health and remediation. *Egypt. J. Pet.*, 25(1):107, 2016.

[9] Luca Guerrini, José V. Garcia-Ramos, Concepción Domingo, and Santiago Sanchez-Cortes. Sensing Polycyclic Aromatic Hydrocarbons with Dithiocarbamate-Functionalized Ag Nanoparticles by Surface-Enhanced Raman Scattering. *Anal. Chem.*, 81(3):953, 2009.

[10] Jingjing Du and Chuanyong Jing. Preparation of Thiol Modified Fe_3O_4@Ag Magnetic SERS Probe for PAHs Detection and Identification. *J. Phys. Chem. C*, 115(36):17829, 2011.

[11] Shuichi Hashimoto, Sigeru Ikuta, Tsuyoshi Asahi, and Hiroshi Masuhara. Fluorescence Spectroscopic Studies of Anthracene Adsorbed into Zeolites: From the Detection of Cation$-\pi$ Interaction to the Observation of Dimers and Crystals. *Langmuir*, 14(15):4284, 1998.

[12] J. W. Hong, Sang il Park, and Z. G. Khim. Measurement of hardness, surface potential, and charge distribution with dynamic contact mode electrostatic force microscope. *Rev. Sci. Instrum.*, 70(3):1735, 1999.

[13] Paul Girard. Electrostatic force microscopy: principles and some applications to semiconductors. *Nanotechnology*, 12(4):485, 2001.

[14] Sibel Ebru Yalcin, Joelle A. Labastide, Danielle L. Sowle, and Michael D. Barnes. Spectral Properties of Multiply Charged Semiconductor Quantum Dots. *Nano Lett.*, 11(10):4425, 2011.

[15] Guicun Qi, Yanlian Yang, Hao Yan, Li Guan, Yibao Li, Xiaohui Qiu, and Chen Wang. Quantifying Surface Charge Density by Using an Electric Force Microscope with a Referential Structure. *J. Phys. Chem. C*, 113(1):204, 2009.

[16] Florian Johann and Elisabeth Soergel. Quantitative measurement of the surface charge density. *Appl. Phys. Lett.*, 95(23):232906, 2009.

[17] Sibel Ebru Yalcin, Joelle A. Labastide, Danielle L. Sowle, and Michael D. Barnes. Spectral Properties of Multiply Charged Semiconductor Quantum Dots. *Nano Lett.*, 11(10):4425, 2011.

[18] Jaroslav Granatier, Petr Lazar, Michal Otyepka, and Pavel Hobza. The Nature of the Binding of Au, Ag, and Pd to Benzene, Coronene, and Graphene: From Benchmark CCSD(T) Calculations to Plane-Wave DFT Calculations. *J. Chem. Theory Comput.*, 7(11):3743, 2011.

[19] Eric C. Le Ru and Pablo G. Etchegoin. Quantifying SERS enhancements. *MRS Bull.*, 38(8):631, 2013.

[20] Christy L. Haynes and Richard P. Van Duyne. Plasmon-Sampled Surface-Enhanced Raman Excitation Spectroscopy. *J. Phys. Chem. B*, 107(30):7426, 2003.

[21] E. C. Le Ru, E. Blackie, M. Meyer, and P. G. Etchegoin. Surface Enhanced Raman Scattering Enhancement Factors: A Comprehensive Study. *J. Phys. Chem. C*, 111(37):13794, 2007.

[22] Kwan Kim, Kyung Lock Kim, and Seung Joon Lee. Surface enrichment of Ag atoms in Au/Ag alloy nanoparticles revealed by surface enhanced Raman scattering spectroscopy. *Chem. Phys. Lett.*, 403(1):77, 2005.

[23] Linyou Cao, Peng Diao, Lianming Tong, Tao Zhu, and Zhongfan Liu. Surface-Enhanced Raman Scattering of p-Aminothiophenol on a Au(core)/Cu(shell) Nanoparticle Assembly. *ChemPhysChem*, 6(5):913, 2005.

Chapter 7

Kelvin Probe Force Microscopy to Probe Metal–molecule Interactions: A Comparative SERS Sensing of Phenanthrene and Pyrene

7.1 Abstract

The metal–molecule interaction leads to the change of the polarizability of the molecule and thus Raman enhancement. In this study, I measure the degree of metal–molecule interaction by Kelvin probe force microscopy (KPFM). Phenanthrene and pyrene both are detected on a gold–SiO_2 sphere substrate. The markedly different enhancement factors (EFs) from pyrene to phenanthrene is linked to the metal–molecule interaction. A notable EF (10^5) for pyrene is achieved.

7.2 Introduction

Surface enhanced Raman spectroscopy (SERS) is gaining tremendous attention due to its fingerprint detection ability and sensitivity at the single molecular level. [1] There are many research studies on understanding the mechanisms behind SERS. [2–6] The primary source of enhancement is the plasmon oscillation at the metal surface during photo-irradiation. [7] In order to experience the plasmonic field, molecules must be close to the metal surface. (The plasmonic field decays exponentially.) [8] Hence, adsorption plays an important role, which can combine with the electromagnetic field to enhance the Raman signal significantly. [9]

Adsorption is affected by and impacts the electronic structure of the molecule as well as the metal surface. [10] The adsorption process can change the polarizability of the molecule and thus its Raman activity. For example, several studies describe how different adsorption orientations influence the SERS activity of the adsorbate. [4, 11] While new and/or shifted peaks arise from the resultant break in symmetry, [12,13] the adsorption effect is more complicated and can include electronic modifications to the adsorbate through binding, electrostatic interactions, or dispersion interactions. [2] Thus, I also see orientation-independent shifts in SERS peaks relative to the normal Raman (unadsorbed) spectrum. [14] This can lead to situations where the same substrate shows different degrees of Raman enhancement for different analytes. [15]

In this chapter I provide direct experimental evidence of the link between the electronic interaction of the molecule adsorbed on the metal surface and the SERS enhancement. Although this metal–molecule interaction is clearly a significant component of enhancement, its contributions to the SERS enhancement mechanism has been mostly explained by computational simulation. [4,16,17] I introduce Kelvin probe force microscopy (KPFM) as a powerful tool to measure the magnitude of the static charge transfer between the analyte molecule and Au metal.

KPFM is an electrical force microscopy that measures the work function of the material using a conductive tip. [18, 19] In KPFM, a conductive tip interacts with the sample surface electronically, and the contact potential difference (CPD) value determines the work function of the material, Φ_{sample} using the known work function of the tip, Φ_{tip} as follows,

$$\text{CPD} = \Phi_{tip} - \Phi_{sample} \tag{7.1}$$

The work function of the tip can be calibrated using highly ordered pyrolytic graphite (HOPG) as a reference ($\Phi = 4.6$ eV). [20]

Beyond the electronic structure of material surfaces, the method can give information about the electronic structure of molecular adsorbates. Recent examples include KPFM evidence for charge-trapping in an organic film [21], surface charge alteration in adsorbed tautomers [19] and for charge transfer between adsorbates and surfaces [22].

In this work, KPFM is used to measure the strength of the metal–molecule interaction through the change in the work function of the molecule upon adsorption on the metal. [22,23] The work function shift arises from charge transfer between the adsorbate and the surface, [24,25] which is also a part of the adsorption contribution to SERS enhancement. The method is demonstrated and validated with a model SERS detection system for phenanthrene and pyrene, two polycyclic aromatic hydrocarbons (PAHs) considered as serious environmental pollutants. [26–30]

7.3 Experimental details

7.3.1 Materials

2-butanone solvent (99%) was obtained from Sigma Aldrich. SiO_2 spheres with a diameter of 1 micron were acquired from Fiber Optics Center Inc. Gold wire (99.9%

metal basis) was obtained from Alfa Aesar. Phenanthrene (98+%) and pyrene (95%) were purchased from Aldrich as PAH analytes. Microscope glass slides (purchased from Pearl, 1.0 mm-1.2 mm thick) were used as a base. 2×2 cm^2 of glass slides were used to prepare substrate. Glass slides were cleaned by both hot concentrated hydrochloric (HCl) and sulfuric (H_2SO_4) acids, and then washed with ultrapure water (18.2 MΩ·cm, Barnstead).

7.3.2 Synthesis of SERS substrate

First, SiO_2 spheres were oven dried and then were dispersed in 2-butanone to a concentration of 15% w/w. 40 μL of dispersed spheres suspension were spin coated (WS400, Laurell Technologies) on glass slides at 3000 rpm for 1 minute. 10 nm or 20 nm of Au were thermally deposited on the sphere coated glass slides. The metal film deposition was conducted with an in-lab-built thermal evaporator operating at a pressure of 10^{-4} torr. A tungsten boat (Kurt J. Lesker) held the Au source, and Au thickness was monitored using a quartz crystal microbalance (QCM, INFICON XTM/2).

7.3.3 Characterization methods

Electrical parameters of each scan were obtained by the work function (Φ) measurement. A MFP-3D (Asylum Research) instrument was used to perform KPFM analysis, with a conductive Au coated tip (Mikromasch, NSC35/Cr-Au, nominal frequency of 140 KHz). A $5 \times 5\,\mu m^2$ area of the sample surface was mapped with 256 points per line, 256 lines, at a scan rate of 0.5 Hz. KPFM measurements were performed in room temperature under atmospheric pressure.

7.3.4 SERS measurement

0.1 mg of phenanthrene or pyrene was dissolved in 1 liter of ultrapure water to make the concentration 0.1 ppm. The whole solution was then sonicated for 4 hrs to promote complete dissolution of the analyte. SERS substrates were soaked into the analyte solution for 30 minutes and then washed with ultrapure water to ensure adsorption efficiency of the analyte onto the metal surface. A Renishaw inVia Raman microscope (a laser source of 830 nm) was used for SERS detection, which is equipped with a charge couple device and a Leica confocal microscope. A laser power of 3 ± 0.3 mW was used for each run with a 40 second exposure time. A $50\times$ (highest magnification) objective was applied to focus the laser on the sample.

7.3.5 Computational details

Computational modeling was performed using GAMESS (US) program package. [31] Full geometry optimization and normal Raman mode calculation of pyrene and phenanthrene were completed using density functional theory (DFT) and with the functional and the basis set combination of B97-1/cc-pVDZ, which has excellent agreement with my experimental normal Raman spectra of PAHs. [32, 33] The calculation of the Raman spectrum was performed on an individual, isolated molecule (i.e., the gas phase).

7.4 Results and discussion

7.4.1 SERS performance

SERS detection was carried out of both analytes (phenanthrene and pyrene) on the 20 nm Au covered SiO_2 sphere coated glass substrates. It is worth noting that no enhancement of PAHs was observed by only Au on glass slides. Raman modes of

phenanthrene were poorly enhanced by the Au-sphere substrate, while those of pyrene were significantly enhanced by the same type of substrate (Figure 7.1). In the case of phenanthrene, three peaks are predominately enhanced: 410 cm^{-1}, 710 cm^{-1} and 1350 cm^{-1}. Enhanced modes of pyrene are 410 cm^{-1}, 594 cm^{-1}, 1236 cm^{-1}, 1395 cm^{-1} and 1609 cm^{-1}. These peaks are also predominant in regular Raman spectra, which are assigned by comparison with the computed spectrum (Appendix Figure F.2 and F.3).

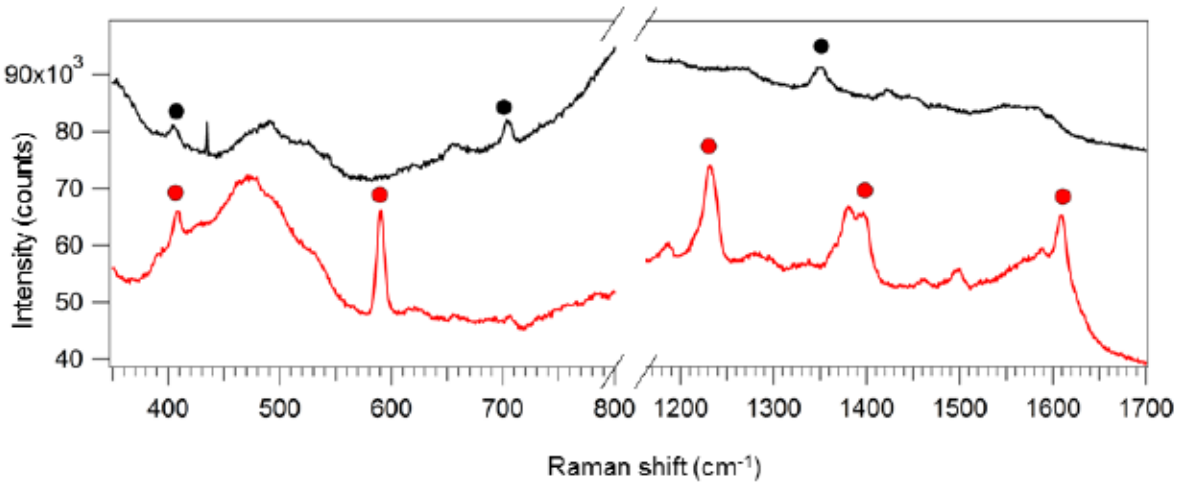

Figure 7.1: SERS spectra of phenanthrene (black) and pyrene (red). Pyrene shows notable Raman enhancement compared to phenanthrene. Dots indicate principal peaks. Spectra are offset for clarity.

Enhancement factor calculations was carried out with the analytical method: [34]

$$\mathrm{EF} = \frac{\mathrm{I}_{SERS}}{\mathrm{C}_{SERS}} \times \frac{\mathrm{C}_{Normal}}{\mathrm{I}_{Normal}} \tag{7.2}$$

I_{SERS} and I_{Normal} are the intensity of the surface enhanced Raman mode and the intensity of the normal Raman mode, respectively. C_{SERS} and C_{Normal} are the concentration of the analyte in SERS experiment and the concentration of the analyte in the normal Raman experiment (0.1 M), respectively. Sphere coated glass (without

the Au layer) was used for the normal Raman measurement.

For the EF calculations, I selected the peak at 410 cm^{-1}, a C-C-C bending mode for both pyrene and phenanthrene as identified computationally (Appendix F.2). The resulting EFs are 7.1×10^5 with pyrene and 1.3×10^5 with phenanthrene.

7.4.2 KPFM study

The strength of the metal–molecule interaction can be directly probed by measuring the perturbation on the molecule electronic structure by the metal. KPFM provides a quantification of that perturbation by measuring the change of the work function (Φ) of the molecule upon adsorption on the metal. The shift of Φ for pyrene and phenanthrene, on the Au SERS substrate and on a plain glass slide, are compared in Table 7.1, which also shows the EFs. The glass slide was chosen as a reference substrate because the molecules show no significant interaction with the glass. [35,36] For example, the lack of adhesion of molecules to the glass slide was clear in the disappearance of Raman signal of the molecules after one rinse with water.

The shift of the Φ ($\Delta\Phi$) was calculated by subtracting:

$$\Delta\Phi = \Phi_{PAH} - \Phi_{PAH-M} \tag{7.3}$$

with Φ_{PAH} being for the PAH analyte on a plain glass slide, and Φ_{PAH-M} being measured for the PAH analyte on the Au/SiO_2 sphere SERS substrate. Table 7.1 lists the $\Delta\Phi$ for both pyrene and phenanthrene.

The amount of metal–molecule interaction is reflected in the magnitude of the Φ, with a larger $\Delta\Phi$ indicating a larger influence by the SERS substrate on that analyte. At the metal–molecule interface, if the molecule undergoes a higher degree of charge transfer with the metal, then the work function of the molecule changes

significantly. [22, 24] Therefore, the higher $\Delta\Phi$ of pyrene on gold supports the higher amount of charge transfer between pyrene and gold, which is reflected in the larger SERS performance for the substrate toward that analyte.

Therefore, I have demonstrated that KPFM can measure the degree of metal–molecule interactions due to charge transfer, which links to the different enhancement performance of a SERS substrate toward different molecules. The KPFM data shows that $\Delta\Phi$ can indicate the perturbation on electronic structure and consequently the polarizability (chemical enhancement).

Table 7.1: Link between $\Delta\Phi$ and EF for two PAHs.

PAH	$\Delta\Phi$ (eV)	EF ($\times 10^5$)
Pyrene	1.106 $\pm$0.09	7.1 $\pm$0.8
Phenanthrene	0.905 $\pm$0.03	1.3 $\pm$0.5

7.5 Conclusions

This investigation was conducted to determine the degree of electronic interaction between Au and PAHs (phenanthrene and pyrene) and its effect on the SERS response. Pyrene was observed to be highly enhanced compared to phenanthrene, with an EF of 7.1×10^5 for the pyrene versus 1.3×10^5 for the phenanthrene. This was due to a higher degree of electron transfer between pyrene and Au, which also leads to changes in the work function. These differences were quantified using KPFM. The higher $\Delta\Phi$ for pyrene upon adsorption to the SERS substrate confirmed the higher degree of metal–molecule interaction compared to phenanthrene. This approach offers a direct link between the metal–molecule interaction and SERS performance.

Bibliography

[1] Sebastian Schlücker. Surface-Enhanced Raman Spectroscopy: Concepts and Chemical Applications. *Angew. Chem. Int. Ed.*, 53(19):4756, 2014.

[2] Lasse Jensen, Christine M. Aikens, and George C. Schatz. Electronic structure methods for studying surface-enhanced Raman scattering. *Chem. Soc. Rev.*, 37:1061, 2008.

[3] Kwan Kim, Jeong-Yong Choi, Hyang Bong Lee, and Kuan Soo Shin. Raman scattering of 4-aminobenzenethiol sandwiched between Ag nanoparticle and macroscopically smooth Au substrate: Effects of size of Ag nanoparticles and the excitation wavelength. *J. Chem. Phys.*, 135(12):124705, 2011.

[4] Zhao, Lasse Jensen, and George C. Schatz. Pyridine–Ag_{20} Cluster: A Model System for Studying Surface-Enhanced Raman Scattering. *J. Am. Chem. Soc.*, 128(9):2911, 2006.

[5] Arthur Losquin, Luiz F. Zagonel, Viktor Myroshnychenko, Benito Rodríguez-González, Marcel Tencé, Leonardo Scarabelli, Jens Förstner, Luis M. Liz-Marzán, F. Javier García de Abajo, Odile Stéphan, and Mathieu Kociak. Unveiling Nanometer Scale Extinction and Scattering Phenomena through Combined Electron Energy Loss Spectroscopy and Cathodoluminescence Measurements. *Nano Lett.*, 15(2):1229, 2015.

[6] Gerard Macias, Maria Alba, Lluis F. Marsal, and Agustin Mihi. Surface roughness boosts the SERS performance of imprinted plasmonic architectures. *J. Mater. Chem. C*, 4:3970, 2016.

[7] Katherine A. Willets and Richard P. Van Duyne. Localized Surface Plasmon Resonance Spectroscopy and Sensing. *Annu. Rev. Phys. Chem.*, 58(1):267, 2007.

[8] P. G. Etchegoin and E. C. Le Ru. A perspective on single molecule SERS: current status and future challenges. *Phys. Chem. Chem. Phys.*, 10:6079, 2008.

[9] Nicholas Valley, Nathan Greeneltch, Richard P. Van Duyne, and George C. Schatz. A Look at the Origin and Magnitude of the Chemical Contribution to the Enhancement Mechanism of Surface-Enhanced Raman Spectroscopy (SERS): Theory and Experiment. *J. Phys. Chem. Lett.*, 4(16):2599, 2013.

[10] Meikun Fan, Feng-Ju Lai, Hung-Lung Chou, Wan-Ting Lu, Bing-Joe Hwang, and Alexandre G. Brolo. Surface-enhanced Raman scattering (SERS) from Au:Ag bimetallic nanoparticles: the effect of the molecular probe. *Chem. Sci.*, 4:509, 2013.

[11] Sho Suzuki, Satoshi Kaneko, Shintaro Fujii, Santiago Marqués-González, Tomoaki Nishino, and Manabu Kiguchi. Effect of the Molecule–Metal Interface on the Surface-Enhanced Raman Scattering of 1,4-Benzenedithiol. *J. Phys. Chem. C*, 120(2):1038, 2016.

[12] Jun Hee Yoon, Jung Shin Park, and Sangwoon Yoon. Time-Dependent and Symmetry-Selective Charge-Transfer Contribution to SERS in Gold Nanoparticle Aggregates. *Langmuir*, 25(21):12475, 2009.

[13] A. Alyami, D. Saviello, M. A. P. McAuliffe, A. Mirabile, L. Lewis, and D. Iacopino. Metal nanoinks as chemically stable surface enhanced scattering (SERS) probes for the analysis of blue BIC ballpoint pens. *Phys. Chem. Chem. Phys.*, 19:14652, 2017.

[14] Semion K. Saikin, Yizhuo Chu, Dmitrij Rappoport, Kenneth B. Crozier, and Alán Aspuru-Guzik. Separation of Electromagnetic and Chemical Contributions

to Surface-Enhanced Raman Spectra on Nanoengineered Plasmonic Substrates. *J. Phys. Chem. Lett.*, 1(18):2740, 2010.

[15] Matthew Rycenga, Moon Ho Kim, Pedro H. C. Camargo, Claire Cobley, Zhi-Yuan Li, and Younan Xia. Surface-Enhanced Raman Scattering: Comparison of Three Different Molecules on Single-Crystal Nanocubes and Nanospheres of Silver. *J. Phys. Chem. A*, 113(16):3932, 2009.

[16] Maurizio Muniz-Miranda, Francesco Muniz-Miranda, and Alfonso Pedone. Raman and DFT study of methimazole chemisorbed on gold colloidal nanoparticles. *Phys. Chem. Chem. Phys.*, 18:5974, 2016.

[17] Nguyen Thi Thai An, Duy Quang Dao, Pham Cam Nam, Bui The Huy, and Hong Nhung Tran. Surface enhanced Raman scattering of melamine on silver substrate: An experimental and DFT study. *Spectrochim. Acta, Part A*, 169(Supplement C):230, 2016.

[18] Zeno Schumacher, Yoichi Miyahara, Andreas Spielhofer, and Peter Grutter. Measurement of Surface Photovoltage by Atomic Force Microscopy under Pulsed Illumination. *Phys. Rev. Applied*, 5:044018, 2016.

[19] Fabian Mohn, Leo Gross, Nikolaj Moll, and Gerhard Meyer. Imaging the charge distribution within a single molecule. *Nat. Nano*, 7(4):227, 2012.

[20] Wan-Hsien Lin, Jih-Jen Wu, Mitch M. C. Chou, Yu-Ming Chang, and Masahiro Yoshimura. Charge Transfer in Au Nanoparticle–Nonpolar ZnO Photocatalysts Illustrated by Surface-Potential-Derived Three-Dimensional Band Diagram. *J. Phys. Chem. C*, 118(34):19814, 2014.

[21] Benjamin C. Hoffman, Terry McAfee, Brad R. Conrad, Marsha A. Loth, John E. Anthony, Harald W. Ade, and Daniel B. Dougherty. Intrinsic Charge Trapping

Observed as Surface Potential Variations in diF-TES-ADT Films. *ACS Appl. Mater. Interfaces*, 8(33):21490, 2016.

[22] Christian Loppacher. *Electronic Properties of Metal/Organic Interfaces*, page 221. Springer Berlin Heidelberg, Berlin, Heidelberg, 2012.

[23] Appan Merari Masillamani, Silvio Osella, Andrea Liscio, Oliver Fenwick, Federica Reinders, Marcel Mayor, Vincenzo Palermo, Jerome Cornil, and Paolo Samori. Light-induced reversible modification of the work function of a new perfluorinated biphenyl azobenzene chemisorbed on Au (111). *Nanoscale*, 6:8969, 2014.

[24] Gregor Witte, Simon Lukas, Paul S. Bagus, and Christof Wöll. Vacuum level alignment at organic/metal junctions: "Cushion" effect and the interface dipole. *Appl. Phys. Lett.*, 87(26):263502, 2005.

[25] Norbert Koch. Organic Electronic Devices and Their Functional Interfaces. *ChemPhysChem*, 8(10):1438, 2007.

[26] Hongyue Zhao, Jing Jin, Weijun Tian, Ran Li, Zhi Yu, Wei Song, Qian Cong, Bing Zhao, and Yukihiro Ozaki. Three-dimensional superhydrophobic surface-enhanced Raman spectroscopy substrate for sensitive detection of pollutants in real environments. *J. Mater. Chem. A*, 3:4330, 2015.

[27] Jingjing Du, Jianwei Xu, Zhenli Sun, and Chuanyong Jing. Au nanoparticles grafted on Fe_3O_4 as effective SERS substrates for label-free detection of the 16 EPA priority polycyclic aromatic hydrocarbons. *Anal. Chim. Acta*, 915:81, 2016.

[28] Hai-Xin Gu, Kai Hu, Da-Wei Li, and Yi-Tao Long. SERS detection of polycyclic aromatic hydrocarbons using a bare gold nanoparticles coupled film system. *Analyst*, 141:4359, 2016.

[29] Meng Jiang, Zhijiang Qian, Xufeng Zhou, Xing Xin, Jinghua Wu, Chao Chen, Gongjun Zhang, Gaojie Xu, and Yuchuan Cheng. CTAB micelles assisted rGO-AgNP hybrids for SERS detection of polycyclic aromatic hydrocarbons. *Phys. Chem. Chem. Phys.*, 17:21158, 2015.

[30] Hussein I. Abdel-Shafy and Mona S.M. Mansour. A review on polycyclic aromatic hydrocarbons: Source, environmental impact, effect on human health and remediation. *Egypt. J. Pet.*, 25(1):107, 2016.

[31] Michael W. Schmidt, Kim K. Baldridge, Jerry A. Boatz, Steven T. Elbert, Mark S. Gordon, Jan H. Jensen, Shiro Koseki, Nikita Matsunaga, Kiet A. Nguyen, Shujun Su, Theresa L. Windus, Michel Dupuis, and John A. Montgomery. General atomic and molecular electronic structure system. *J. Comput. Chem.*, 14(11):1347, 1993.

[32] Fred A. Hamprecht, Aron J. Cohen, David J. Tozer, and Nicholas C. Handy. Development and assessment of new exchange-correlation functionals. *J. Chem. Phys.*, 109(15):6264, 1998.

[33] Thom H. Dunning Jr. Gaussian basis sets for use in correlated molecular calculations. I. The atoms boron through neon and hydrogen. *J. Chem. Phys.*, 90(2):1007, 1989.

[34] E. C. Le Ru, E. Blackie, M. Meyer, and P. G. Etchegoin. Surface Enhanced Raman Scattering Enhancement Factors: A Comprehensive Study. *J. Phys. Chem. C*, 111(37):13794, 2007.

[35] Mark Turner, Vladimir B. Golovko, Owain P. H. Vaughan, Pavel Abdulkin, Angel Berenguer-Murcia, Mintcho S. Tikhov, Brian F. G. Johnson, and Richard M.

Lambert. Selective oxidation with dioxygen by gold nanoparticle catalysts derived from 55-atom clusters. *Nature*, 454:981, 2008.

[36] Luis M. Liz-Marzán, Michael Giersig, and Paul Mulvaney. Synthesis of Nanosized Gold−Silica Core−Shell Particles. *Langmuir*, 12(18):4329, 1996.

Chapter 8

Conclusions and Future Direction

8.1 Conclusions

8.1.1 Fundamental advances

The main objective of this thesis is to deliver an innovative approach towards understanding surface enhanced Raman scattering (SERS) mechanisms for multicomponent substrates. Metal-semiconductor, bimetallic, metal-insulator substrates were tested for polycyclic aromatic hydrocarbon (PAH) detection and observed to be highly efficient. Phenanthrene and pyrene, my test PAHs, were detected in as low as sub-nanomolar concentrations with an enhancement factor of 10^6.

My work has also demonstrated the versatility of scanning probe microscopy (SPM) in the study of SERS mechanisms. Atomic force microscopy (AFM), Kelvin probe force microscopy (KPFM), and electrical force microscopy (EFM) provided key data on both surface morphology and electronic properties of SERS substrates. By mapping these properties, I could distinguish between competing effects contributing toward Raman enhancement. The relation between the plasmonic absorption and the surface properties of the metallic substrate also illustrated the enhancement mecha-

nisms.

While focused on Au coated ZnO substrates, this thesis includes an examination of ZnO crystals of different size and shape as well as different thickness of Au coatings. Rod-like, hexagonal pyramid and triangular ZnO crystals, produced with simple sol-gel techniques, showed different electronic structure and SERS response.

Rod-like ZnO crystals coated with Au achieved significant Raman enhancement of phenanthrene as a PAH analyte. The generation of surface charge on gold (Au) as a result of the Fermi level equilibrium between Au and ZnO was demonstrated by KPFM. The measurement of the work function values of Au films on ZnO explained the positive surface charge on the gold film, which was the main promoter of analyte adsorption. The surface roughness of these Au/ZnO films also accounted for the enhancement, as explained in Chapter 2.

The thermal treatment of hexagonal pyramidal crystal ZnO films modified both the surface and electronic properties of ZnO. After Au was deposited on these ZnO films, the Au surface reflected the roughness of the underlying annealed ZnO layer, with roughness controlled by annealing temperature. This roughness of the Au/ZnO hybrid yielded a hydrophobic surface, which facilitated the adsorption of non-polar phenanthrene from its aqueous solution. Furthermore, the rough metal surface also produced electromagnetic hot-spots, with the result that Au on the roughest ZnO film displayed the highest SERS activity. The metal–molecule interaction study using KPFM also demonstrated the tuning of the phenanthrene–Au interaction due to the annealing of ZnO. In Chapter 3, the perturbation of the phenanthrene electronic structure through strong metal–molecule interactions, combined with the roughness and hydrophobicity control the SERS response.

The deposition of gold onto triangular ZnO crystals had a significant impact on the SERS performance of the substrates studied in Chapter 5. The ZnO used in this

chapter was defect rich, leading to different EFs than for Au/ZnO samples in Chapter 2, because of the different enhancement mechanisms for different types of ZnO. The addition of the Au layer modifies the crystal and electronic properties of the ZnO, thus affecting the SERS activity. This chapter provides a new approach in considering the role of the plasmonic metal, with an example of a different way in which metal layers can impact SERS activity.

As analyte adsorption is a key step in SERS sensing, metal–molecule (M–m) interactions are important to study the chemical enhancement effect on SERS response. Chapter 7 introduces KPFM to measure the extent of the interaction between the analyte molecule and the metal surface, using the test case of phenanthrene and pyrene on a gold film. With this KPFM data, I can ascribe a notable Raman enhancement of pyrene, compared to phenanthrene, to its higher degree of M–m interaction.

Dielectric interlayers can also tune the SERS activity of a substrate. The insulating layer prevents the plasmonic hot electron injection into the co-material, which results in the confinement of the intense plasmonic field on the metal surface. As a result, SERS activity of, *e.g.*, Au-coated PMMA covered SiO_2 sphere substrates was greatly affected by the thickness of the insulating (PMMA) layer, which is described in Chapter 4. A comparative study between Au-PMMA-SiO_2 sphere and Au-sphere substrates confirmed notable SERS activity with PMMA interlayer, thus supporting the role of the insulating layer on the enhancement of the plasmonic field.

Different metals will naturally interact differently with analytes, but they also interact differently with any underlying layers. In PMMA-sphere substrates coated with bimetallic Ag-Au films, I have the further possibility of tuning the metal-metal interaction. Due to the Fermi level difference between Ag and Au, at the bimetallic interface an electron transfer occurs and Ag possesses a positive surface charge, while the Au surface becomes negatively charged. The adsorption of π electron rich

pyrene was controlled by the metallic surface charge. As a result, the substrate with Ag as the top layer showed considerable SERS activity due to its positive surface charge. In addition to illustrating surface charge controlled SERS activity, Chapter 6 also demonstrated the use of EFM to detect and map surface charge generation in multilayer systems.

In summary, my experiments identify and demonstrate both electromagnetic and chemical Raman enhancement mechanisms. Both EFM and KPFM data provide the link between the surface electronic properties of the substrate and its SERS response. The surface charge generated by metal-semiconductor and bimetallic substrates impacted analyte adsorption. The composition and thickness of the underlayers can tune the electronic response, while the metal thickness controls surface morphology, which also impacts analyte adsorption (chemical mechanism) but also plasmon absorption and hotspot generation (electromagnetic mechanism).

8.1.2 Practical applications

These fundamental findings have enabled practical advancement of sensing materials. Using the understanding of the SERS mechanisms in composite materials, we have designed new SERS substrates for which we are seeking patent protection for further commercialization. These have been tested with field samples of produced water (PW) provided by industrial partners through Petroleum Research Newfoundland and Labrador (PRNL).

8.2 Future Direction

An important next step to understand the impact of excitation wavelength on SERS response is described here. Future study on the electronic excitation in these mul-

ticomponent systems will establish the mechanism for laser excitation wavelength-controlled SERS activity.

8.2.1 Background

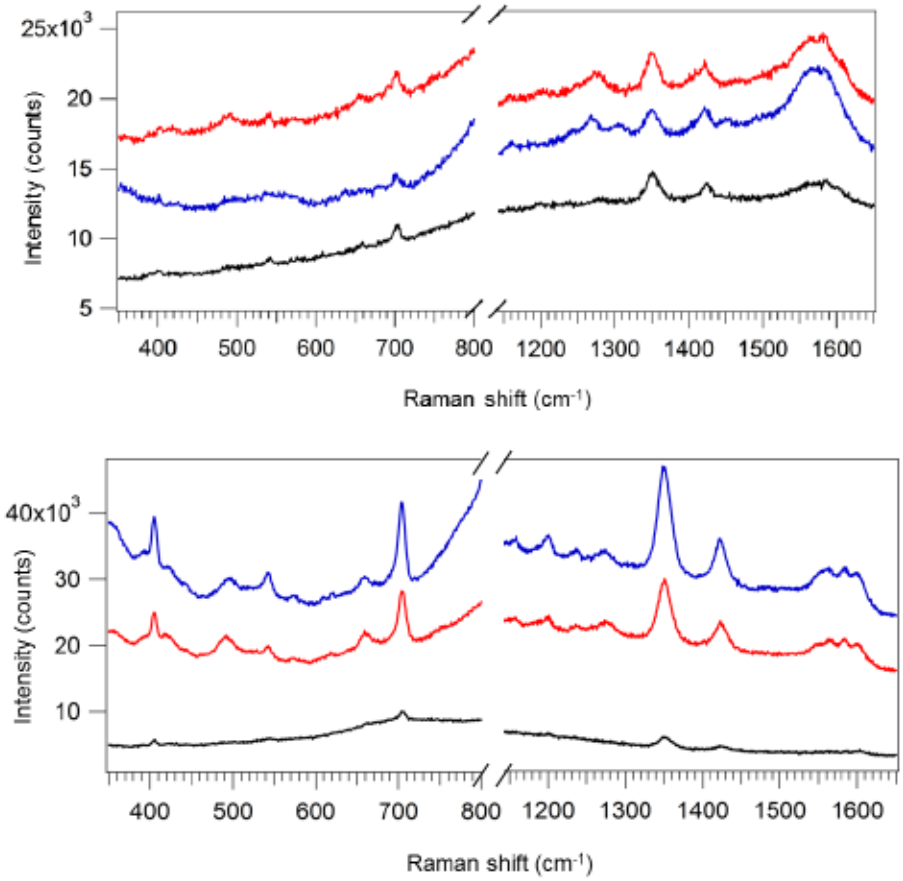

Figure 8.1: SERS spectra of phenanthrene under exposure of 633 nm (top) and 830 mm (bottom) of Raman laser wavelengths. Au 35 nm (red), Au 25 nm (black) and Au 15 nm (blue) on ZnO film. The laser wavelength dependent SERS activity is demonstrated here. 15 nm of Au on ZnO shows highest SERS activity under 830 nm of Raman laser exposure, while 35 nm of Au on ZnO is the superior one with 633 nm of Raman laser. Graphs are offset for clarity.

SERS relies on both electromagnetic and chemical enhancement. Both of these mechanisms are impacted by the laser excitation wavelength. [1] Hence, the Raman laser excitation wavelength is a crucial factor for the enhancement mechanism. The

surface plasmon absorption should be comparable with the Raman laser excitation wavelength in order to generate an intense plasmonic field. [2]

On the other hand, in the case of metal-semiconductor hybrid materials, hot electron injection occurs from the metal to the semiconductor as a result of laser exposure, which ultimately reduces the plasmonic field. This electron injection process solely depends on the energy gap (Schottky barrier height) between the metal Fermi level and the conduction band of the semiconductor, which should be same as the energy of the laser. [3]

8.2.2 Experimental approach

In a preliminary experiment, I have tested the SERS activity of Au-ZnO substrates towards phenanthrene with two different laser wavelengths (830 and 633 nm). As seen in Figure 8.1, the SERS response and the trends in enhancement with Au thickness are quite different depending on the laser wavelength.

To better understand the link between excitation wavelength and substrate performance, I propose the use of photo-KPFM [4,5] as well as plasmon absorption spectroscopy. The plasmon absorption study will illustrate the plasmon field generation in different substrates at each laser excitation. Photo-KPFM will also demonstrate the change of electronic properties of substrates with laser exposure and consequently the magnitude of the hot electron injection from the metal to the semiconductor. [4]

With this approach, I will be able to design new classes of substrates for the particular excitation lasers required for various applications. For example, as explained in Chapter 4, some analytes fluoresce and therefore require a lower energy excitation laser.

Bibliography

[1] Paul L. Stiles, Jon A. Dieringer, Nilam C. Shah, and Richard P. Van Duyne. Surface-Enhanced Raman Spectroscopy. *Annu. Rev. Anal. Chem.*, 1(1):601, 2008.

[2] Sebastian Schlücker. Surface-Enhanced Raman Spectroscopy: Concepts and Chemical Applications. *Angew. Chem. Int. Ed.*, 53(19):4756, 2014.

[3] Hossein Shokri Kojori, Ju-Hyung Yun, Younghun Paik, Joondong Kim, Wayne A. Anderson, and Sung Jin Kim. Plasmon Field Effect Transistor for Plasmon to Electric Conversion and Amplification. *Nano Lett.*, 16(1):250, 2016.

[4] Liam D Whelan. Determining the electronic properties of surface enhanced raman spectroscopy substrates. Master's thesis, Memorial University of Newfoundland, Canada, 2014.

[5] Ming-Chung Wu, Hseuh-Chung Liao, Yu-Cheng Cho, Geza Toth, Yang-Fang Chen, Wei-Fang Su, and Krisztian Kordas. Photo-Kelvin probe force microscopy for photocatalytic performance characterization of single filament of TiO2 nanofiber photocatalysts. *J. Mater. Chem. A*, 1:5715, 2013.

Appendix A

Supporting Information: Chapter 2

A.1 ZnO film synthesis

100 mL of 0.05 M zinc acetate, dihydrate ($ZnOAc_2 \cdot 2\,H_2O$ $\geq$99.0%, J T Baker) solution and 100 mL of 1.5 M NaOH (99%, Sigma Aldrich) solution were prepared in ultrapure water (Barnstead, 18.2 MΩ·cm). The NaOH solution was then added to the zinc acetate solution, which generated zinc hydroxide. Afterwards, acid cleaned glass slides cut to 2×2 cm^2 were placed horizontally at the bottom of the solution beaker. The solution was then heated for 30 minutes at 35°C, which resulted in a white turbid appearance. After the heating process, the solution was kept at room temperature for 6 hours, while generating a ZnO thin film on the glass slides. The coated slides were washed with ultrapure water and air dried. A quartz crystal microbalance (INFICON XTM/2 deposition monitor) was used to monitor metal thickness during gold vapor deposition (locally-built instrument).

The data presented here comes from samples prepared in two separate batches. In all cases the SERS performance is consistent (see standard deviations in Table 2.1 or Figure 2.4), and another researcher has also been able to achieve comparable results

by following this method. Therefore, I am confident that the method is reproducible.

A.2 XRD and SEM instrumental details

X-ray diffraction (XRD) characterization of samples was conducted using the Rigaku Ultima-IV instrument with a Cu K-α source at 40 kV and 44 mA.

Field emission scanning electron microscopy (FESEM) images were acquired using a JEOL JSM-7100F equipped with a field emission source at 15 kV.

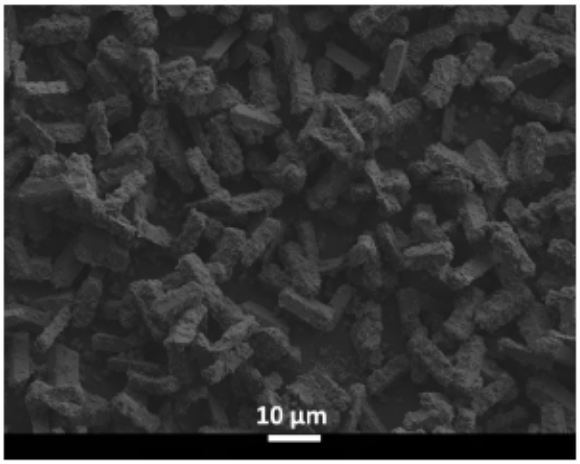

Figure A.1: FESEM image of a film of rod shaped ZnO crystals, taken at lower magnification than the image in Figure 1 in Chapter 2.

A.3 Raman analysis

All Raman spectra were collected with a Renishaw inVia Raman microscope using 20× magnification and 40 seconds of exposure time of the 830 nm laser source at 3.0 ± 0.3 mW power. Figure A.2 shows a Raman spectrum of a ZnO sample.

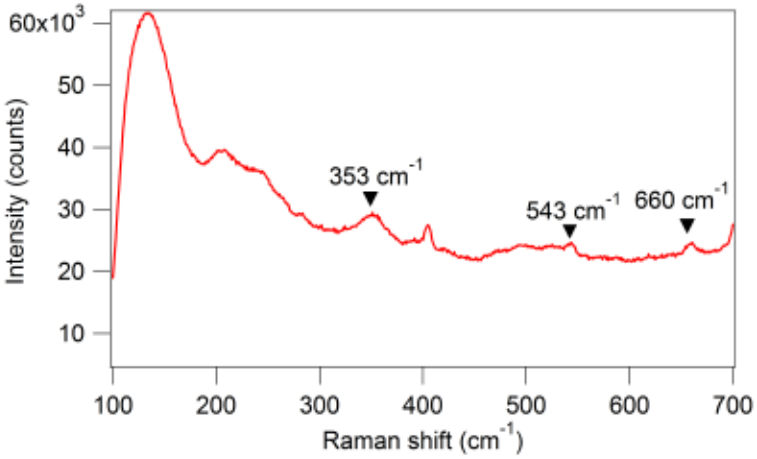

Figure A.2: Raman spectrum of ZnO shows three characteristic ZnO Raman peaks.

The Raman spectrum (Figure A.2) of as-prepared ZnO shows a shift in the A_1(LO) mode at 543 cm^{-1}. A shift in the Raman spectrum could arise from oxygen deficiency, strain due to crystal lattice mismatch, or the presence of dopants or contaminants. This red shift of A_1(LO) mode in ZnO arises from oxygen deficiencies. [1–3] The other Raman peaks at 353 cm^{-1} and 660 cm^{-1} correspond to (E_2-E_1) and Zn sublattice vibration modes, respectively. [4]

A.4 Plasmon absorption of different substrates

Plasmon optical absorption was measured with an Ocean Optics USB 2000 spectrophotometer using diffuse reflectance. Absorption intensity was calculated from the

percent reflectance (%R) using the Kubelka-Munk equation. [5]

$$\frac{K}{S} = \frac{(1-R)^2}{2R} \tag{A.1}$$

where K is the absorption coefficient and S is the scattering coefficient.

The plasmon appears in the UV-visible absorption spectrum as a broad peak. Comparable excitation wavelength and plasmon absorption wavelength could contribute to signal enhancement, [6] and I do see plasmon absorption in the near-IR region in Figure A.3. Nevertheless, although the plasmon absorption intensity changes with thickness, the changes are not enough to explain the difference in SERS activity.

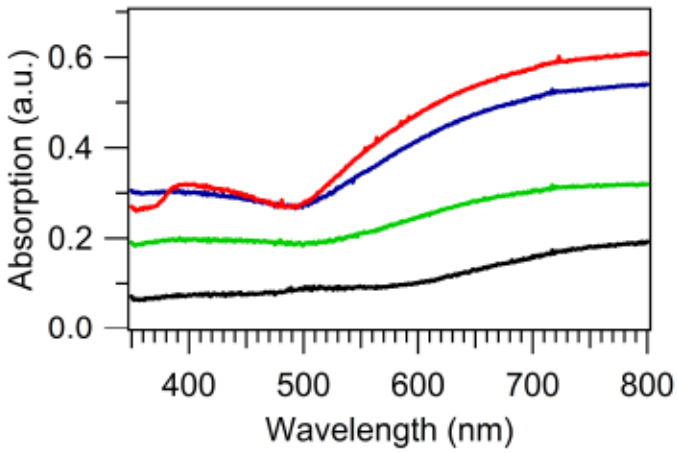

Figure A.3: Optical absorption of different thicknesses of Au covered ZnO shows higher plasmon absorption of A45 (red) and A35 (blue) over A15 (green) and A25 (black).

A.5 Enhancement factor (EF) calculations

For the enhancement factor calculation, [7] the reference substrate for the normal Raman measurement was a glass slide exposed to a 0.1 M aqueous phenanthrene solution for thirty minutes. Because of the weak adsorption of phenanthrene to glass, the an-

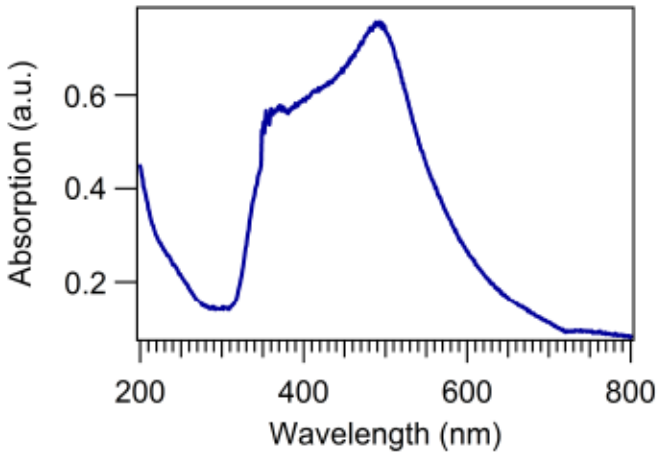

Figure A.4: The plasmon absorption spectrum of a 35 nm thick Au film on glass alone does not show any absorption near the Raman excitation wavelength. This spectrum was recorded using a transmission geometry since Au on glass generates a relatively transparent film.

alyte was no longer detectable after rinsing even at such high concentrations. Therefore, the reference samples were not rinsed before drying, and may be *under*estimating enhancement factors.

The enhancement factor calculation used the vibrational mode at 710 cm^{-1} due to its high intensity.

$$EF = \frac{I_{SERS}}{C_{SERS}} \times \frac{C_{Normal}}{I_{Normal}} \tag{A.2}$$

I_{SERS} and I_{Normal} are the intensities of the surface enhanced Raman mode and the normal Raman mode, respectively. C_{SERS} and C_{Normal} are the concentrations of the analyte in the SERS and the normal Raman measurements, respectively.

The Raman spectra for phenanthrene adsorbed from various concentration solutions are shown in Figure A.5, using the A35 substrate. Raman signal intensity (peak height relative to baseline) decreases when lowering the phenanthrene concentration. Nevertheless, the peak is still detectable even at a concentration of 0.001 ppm (or 1 ppb).

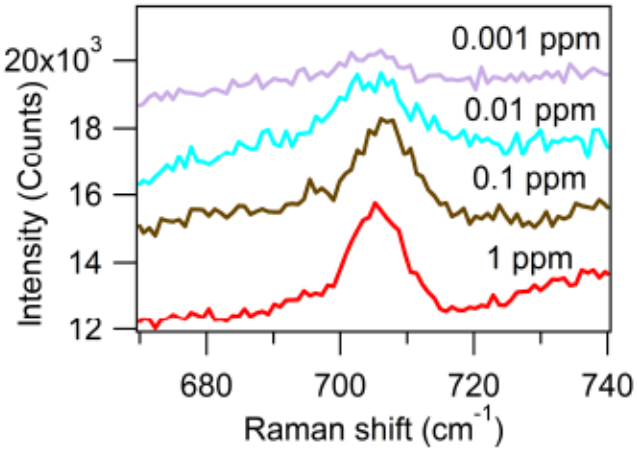

Figure A.5: A comparison of Raman signal at 710 cm^{-1} for phenanthrene solutions of 1 ppm, 0.1 ppm, 0.01 ppm and 0.001 ppm (1 ppb). The spectra are offset for clarity.

A.6 SERS activity of only Au and only ZnO

The Raman spectra from control experiments with a 35 nm thick Au film or ZnO film (on glass) show no SERS activity (no analyte peaks after exposure to 1 ppm of phenanthrene). The spectra are shown in Figure A.6.

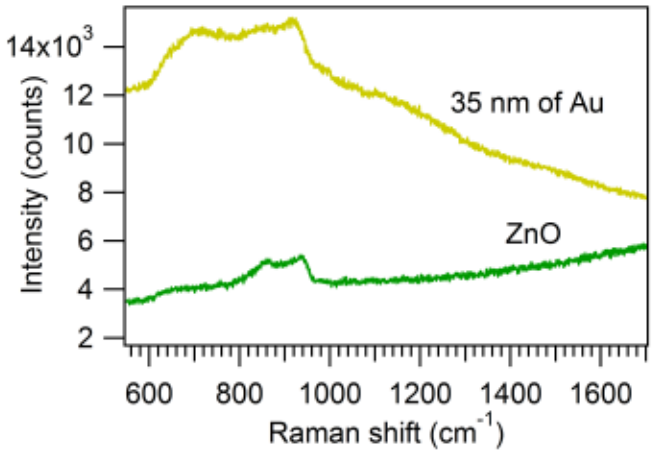

Figure A.6: Both Au and ZnO films alone are SERS inactive.

A.7 Surface area, roughness, and work function measurements

A Pt coated tip (Mikromasch NSC35/Pt; resonance frequency = 300 kHz and force constant = 16 N/m) was used for KPFM with the MFP-3D (Asylum Research) instrument. All scans were performed with 256 points per line and 256 lines per image at a 0.5 Hz scan rate.

The samples involved Au deposited on top of a film of ZnO nanorod film; the Au layer is not conformal. Therefore, during the scan the tip interacts with gold, but it also encounters bare ZnO at crystal edges. This is consistent with the significant difference between the work functions near the center and at the edges of the crystals (Figure 2.3 in Chapter 2). Six different 1 μm^2 areas were selected on top of a Au covered nanorod to calculate the work function as well as the surface area (Figure A.7). By avoiding the very edges but considering several regions, we were truly measuring the work function of Au on ZnO in each case, while still capturing the possible variation in work function across a Au-covered ZnO rod.

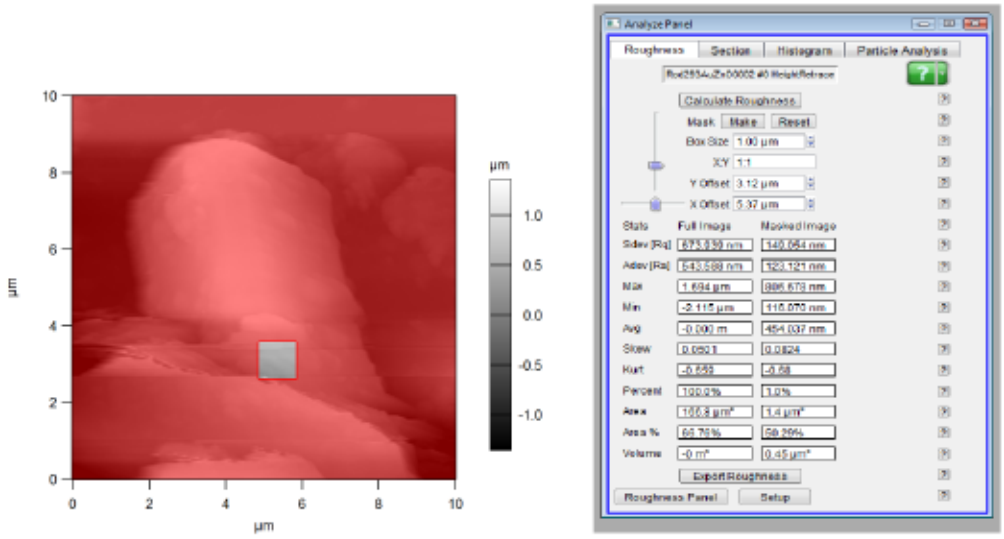

Figure A.7: Masking procedure to calculate surface area of Au covered ZnO nanorods. The screen capture is from the Asylum Research procedures within IGOR. In this example, the 1 μm^2 small gray box in the image at left has a surface area of 1.4 μm^2. This approach was used to select data for the work function calculations as well, selecting areas near the centers of crystals.

The roughness factor R_q calculation used the following equation [8],

$$R_q = \sqrt{\frac{1}{n}\sum_{i=1}^{n} Z_i^2} \tag{A.3}$$

Here Z is the height deviation from the mean surface (xy plane) of the sample and n is number of points per area. This height data provides the Z values for the above equation. The roughness factors plotted in Chapter 2 (Figure 2.4) are also presented in Table A.1.

Table A.1: Roughness factors of different thicknesses of Au on ZnO.

Sample tag	R_q (nm)
A45	109 ± 9
A35	157 ±16
A25	207 ± 8
A15	138 ±10

Appendix B

Supporting Information: Chapter 3

B.1 ZnO film synthesis

100 mL of 0.05 M zinc acetate, dihydrate ($ZnOAc_2 \cdot 2\,H_2O$, $\geq$99.0%, J T Baker) aqueous solution was prepared with ultrapure water (18.2 MΩ·cm, Barnstead). Then 100 mL of 1.5 M NaOH (99%, Sigma Aldrich) aqueous solution was added and mixed well. Acid cleaned glass slides were placed horizontally on the bottom of the reaction container (500 mL glass beaker) and heated for 1 hour at 40°C. Afterwards, the heated solution was cooled down to room temperature through overnight settling. A thick, white ZnO film appeared on the glass slide, which was rinsed further with ultrapure water and then air dried. [9] The chemical reaction for the formation of ZnO is [9]

$$Zn(OAc)_2 + 2\,NaOH \rightarrow Zn(OH)_2 + 2\,NaOAc \rightarrow ZnO + H_2O \qquad (B.1)$$

B.2 XRD and SEM instrumental details

X-ray diffraction (XRD) characterization of samples was conducted using the Rigaku Ultima-IV instrument with a Cu K-α source at 40 kV and 44 mA.

Field emission scanning electron microscopy (FESEM) images were acquired using a JEOL Jsm-7100F equipped with a field emission source at 15 kV.

B.3 Raman microscopy

Raman spectra were collected with a Renishaw inVia Raman microscope equipped with an 830 nm laser source with 3.0 ± 0.3 mW power, under $50\times$ magnification with a 40 s exposure time. Figure B.1 shows the change of Raman vibrational modes of ZnO with annealing treatment.

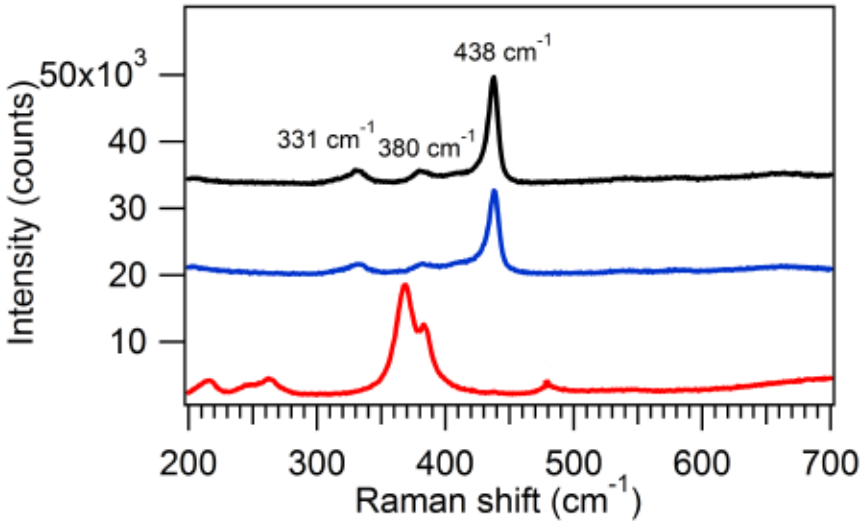

Figure B.1: Raman spectra of different types of ZnO films (unannealed ZnO (red), 200°C ZnO (blue) and 400°C ZnO (black); Spectra are offset for clarity.). Annealed ZnO spectra have the characteristic 438 cm^{-1} peak.

B.4 Thermogravimetric analysis

Thermogravimetric analysis on the TGA Q500 signalled changes during thermal treatment. A 10.96 mg ZnO sample was heated to 200°C and kept at that temperature for 2 hours, mimicking the annealing program for AZ200 sample preparation. The

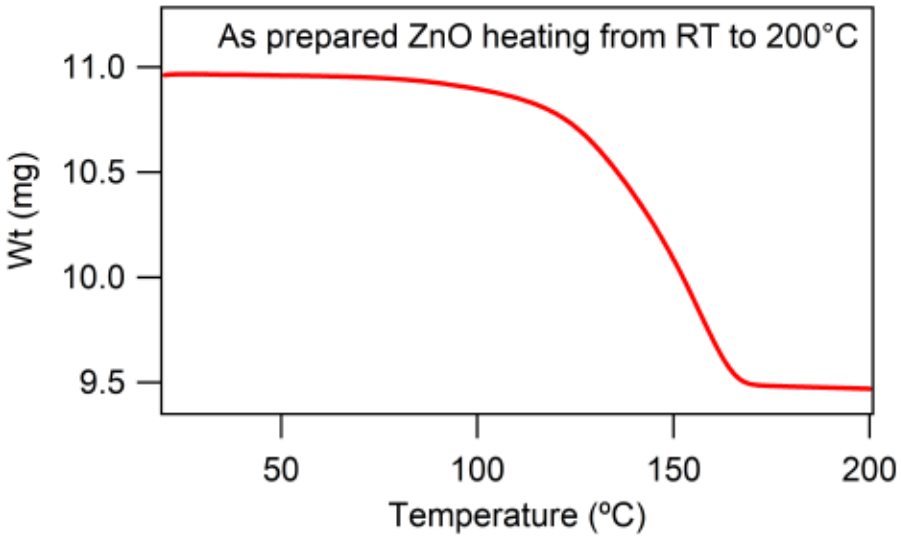

Figure B.2: Thermogravimetric analysis of ZnO film shows the water elimination process during heat treatment.

data, plotted in Figure B.2 indicates a mass loss between 100°C and 150°C, due to the water elimination process. [10]

B.5 DRS technique

The diffuse reflectance spectroscopy was used to measure the plasmon absorption of Au/ZnO films using the Kubelka-Munk equation, [5]

$$\frac{K}{S} = \frac{(1-R)^2}{2R} \tag{B.2}$$

Here, K is absorption coefficient, S is scattering coefficient and R is the reflectance.

B.6 Enhancement factor calculation

The enhancement factor calculation was calculated as below,

$$\mathrm{EF} = \frac{\mathrm{I}_{SERS}}{\mathrm{C}_{SERS}} \times \frac{\mathrm{C}_{Normal}}{\mathrm{I}_{Normal}} \tag{B.3}$$

I_{SERS} and I_{Normal} are the intensity of the surface enhanced Raman mode and the intensity of the normal Raman mode, respectively. C_{SERS} and C_{Normal} are the concentrations of the analyte in the SERS experiment and the normal Raman experiment (0.1 M), respectively.

B.7 Contact angle measurement

Contact angle measurements involved placing 5 μL of ultrapure water on the sample surface. An image was captured after aligning a digital camera with the sample surface plane. Five samples for each Au/ZnO substrate were measured using the OCA 15EC contact angle measurement instrument.

The relation between the water contact angle (θ^*) on the rough surface with surface fraction of the substrate (f_1) and air pockets ($1–f_1$) can be expressed as [11]

$$\cos\theta^* = f_1 \cos\theta - (1 - f_1) \tag{B.4}$$

where θ is the water contact angle on the smooth surface.

B.8 Atomic force microscopy

KPFM and topographical data were acquired concurrently using a MFP-3D (Asylum Research) atomic force microscope. The conductive tip (Mikromasch, NSC35/Cr-Au)

had a resonance frequency of about 120 kHz. A 1×1 μm^2 scan area was mapped with a scan rate of 0.5 Hz. 5 spots were imaged on each duplicate sample. The surface area was calculated for each 1×1 μm^2 scan. The roughness factor and CPD were calculated on masked areas of 0.25×0.25 μm^2, using the same masking procedure as in section A.7.

The roughness factor R_q calculation used the following equation: [8],

$$R_q = \sqrt{\frac{1}{n}\sum_{i=1}^{n} Z_i^2} \tag{B.5}$$

Here Z represents height deviation from the mean surface (xy plane) of the sample and n is the total number of points per area.

Table B.1 collects the surface area for the highest-performing SERS substrates from three different chapters. The high surface area for the substrates from Chapter 3 allows for a larger linear detection range compared to the substrates from other chapters.

Table B.1: Surface area (per μm^2) for different SERS substrates.

Chapter	Sample details	Surface area (μm^2)
2	35 nm Au on rod shaped ZnO	1.33 ± 0.17
3	35 nm Au on annealed hexagonal prism ZnO	1.59 ± 0.09
4	25 nm Au on PMMA-SiO_2 spheres	1.09 ± 0.13

B.9 Cathodoluminescence (CL) analysis

CL spectra were collected using the JEOL JXA-8230 electron probe microanalyzer (EPMA) equipped with a tungsten filament. As a result of the thermal treatment, the electronic properties of the material changed, as well as their crystal properties analyzed with other methods described above. From Figure B.3 I can see that the

band gap (peak maximum) shifts upon annealing. This shift is linked to a change in the Fermi level of ZnO. [12]

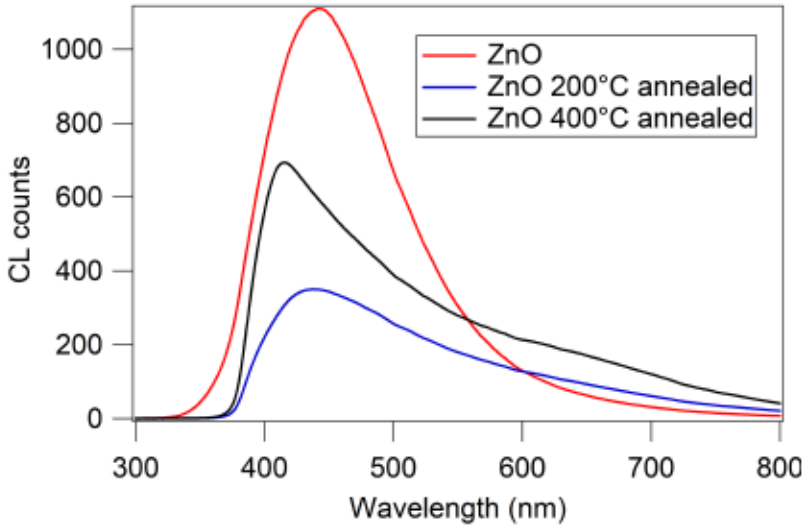

Figure B.3: CL spectra show the change of band gap of ZnO with annealing.

Appendix C

Supporting Information: Chapter 4

C.1 Substrate fabrication

.

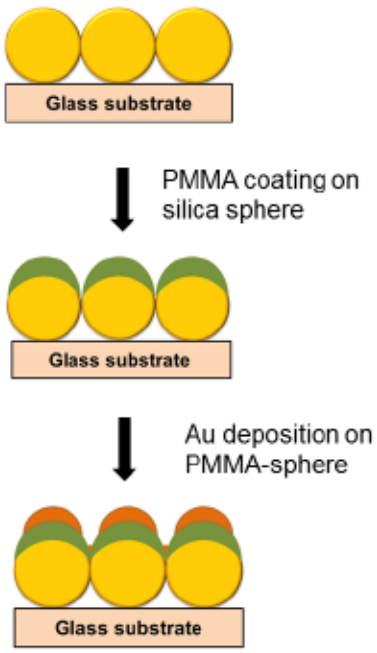

Figure C.1: Schematic representation of Au-PMMA-SiO_2 sphere substrate synthesis. Au is deposited on top of the PMMA-coated SiO_2 spheres and at the junction of the spheres.

C.2 Characterization methods

C.2.1 FESEM

Field emission scanning electron microscopy (FESEM) images were acquired using a JEOL Jsm-7100F equipped with a field emission source at 15 kV.

C.2.2 Scanning probe microscopy (SPM)

A MFP-3D (Asylum Research) scanning probe microscope was used to perform the surface topographic analysis. Tapping mode SPM (KPFM) scans were conducted using a Pt/Ti coated tip (Mikromasch, NSC35/Pt, nominal resonance frequency of 145 kHz). 5×5 μm^2 areas of the sample surface were mapped with 256×256 pixels at a scan rate of 0.5 Hz. All measurements were performed at room temperature and atmospheric pressure.

Table C.1: Surface roughness and EFs for samples with 35 nm Au.

Sample tag	PMMA layer	R_q (nm)	EF$\times10^5$
A3	thick	43.102 ± 2.084	0.42 ± 0.06
B3	thinner	49.343 ± 1.390	0.69 ± 0.04
C3	thinnest	56.901 ± 1.896	1.61 ± 0.08

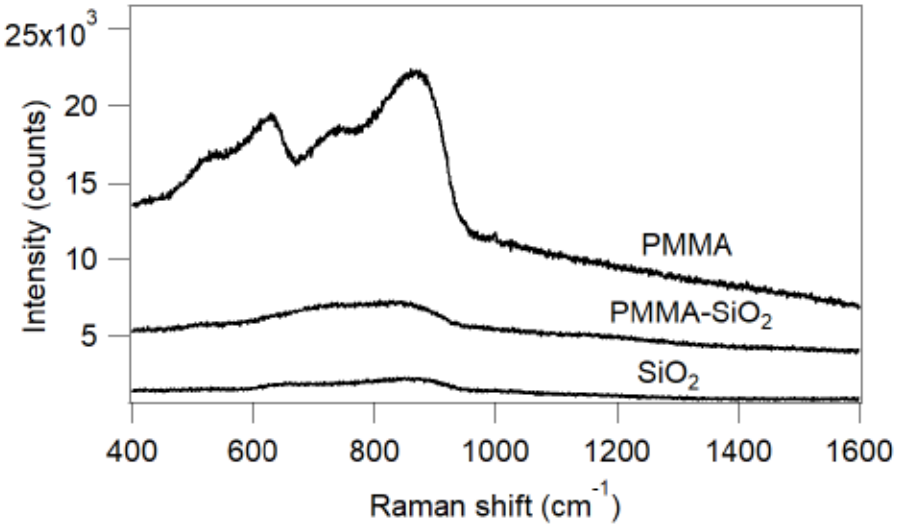

Figure C.2: No SERS activity was observed with substrates of only SiO_2 spheres, only PMMA, or PMMA-SiO_2, when exposed to a 1 ppm aqueous solution of phenanthrene. The peaks below 1000 cm^{-1} are characteristic of the PMMA film itself. Spectra are offset for clarity.

Appendix D

Supporting Information: Chapter 5

D.1 The differences between Au/ZnO hybrids in Chapter 2 and 5

Au doping in the ZnO crystal can be facilitated by the generation of atom vacancies. [13] The ZnO crystal in the Au doping case contained low crystallinity or higher concentration of defects. Au atoms can easily penetrate in the defect-rich ZnO crystal.

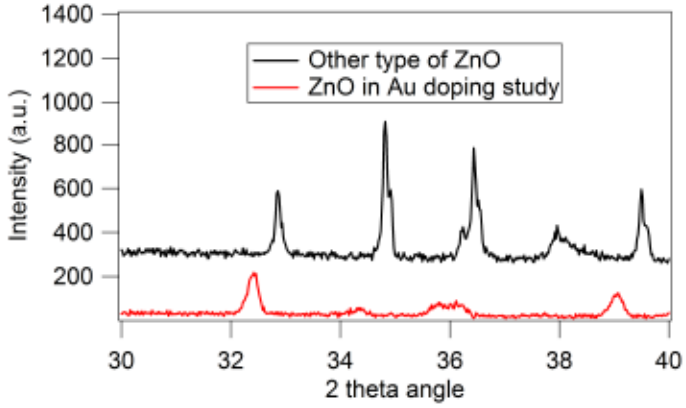

Figure D.1: Low crystallinity of ZnO was observed in Au doping studies compare to ZnO in Chapter 2.

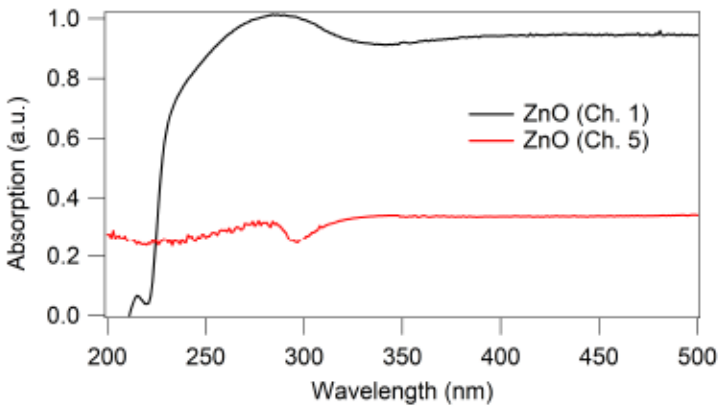

Figure D.2: The different onset of optical absorption of ZnO in Chapter 2 and Chapter 5 reveals different electronic structure of two ZnO.

Crystal parameters were calculated using Bragg's law [14]

$$n\lambda = 2d\sin\theta \tag{D.1}$$

where n=1, λ is the X-ray wavelength (Cu K-α), d is the crystal plane spacing and θ is the angle of diffraction.

Table D.1: Comparison of lattice parameters a and c between ZnO crystals of Chapters 2 and 5

Chapter	a (Å)	c (Å)
2	2.791	5.150
5	2.862	5.212

Table D.2: EFM phase shift ($\Delta\varphi$) to determine the quality of surface charge on the gold in Au/ZnO substrates.

Au (30/35 nm)/ZnO	$\Delta\varphi$ (+3 V)	$\Delta\varphi$ (–3 V)	Surface charge
Chapter 2	6.23 ±0.96	8.51 ±0.50	Positive
Chapter 5	6.91 ±0.76	2.91 ±0.98	Negative

D.2 Enhancement factor calculation

$$\mathrm{EF} = \frac{\mathrm{I}_{SERS}}{\mathrm{C}_{SERS}} \times \frac{\mathrm{C}_{Normal}}{\mathrm{I}_{Normal}} \tag{D.2}$$

I_{SERS} and I_{Normal} are the intensity of the surface enhanced Raman mode and the intensity of the normal Raman mode, respectively. C_{SERS} and C_{Normal} are the concentration of the analyte in SERS experiment and the concentration of the analyte in the normal Raman experiment (0.1 M), respectively. In this calculation, the 710 cm^{-1} mode (C–C stretching, HCC bending) of phenanthrene was taken as the characteristic enhanced peak.

D.3 XPS and EPR spectra

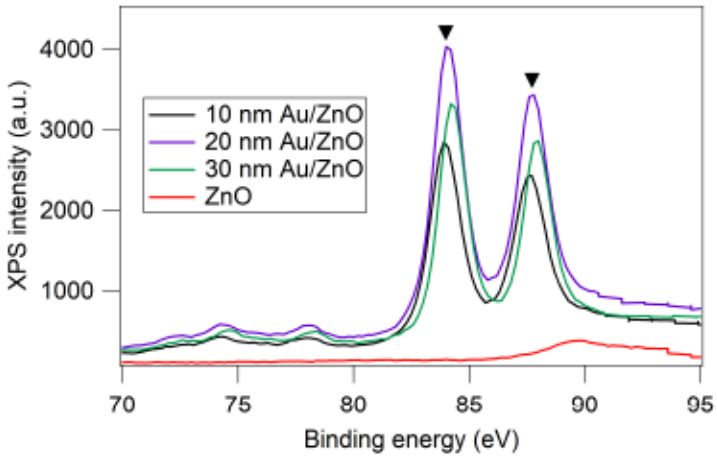

Figure D.3: A shift of $4f_{7/2}$ peak with increasing Au thickness on ZnO indicates Au–ZnO interaction.

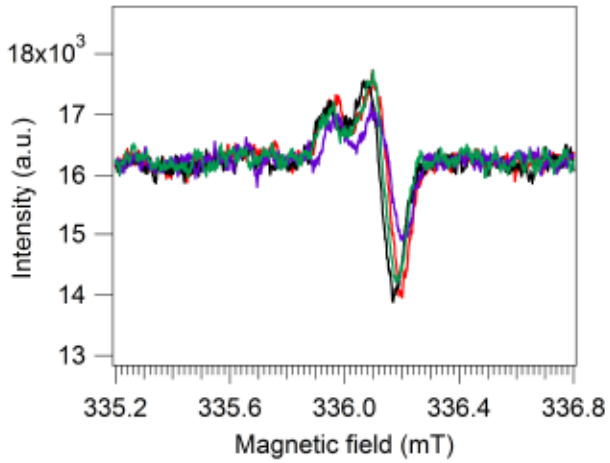

Figure D.4: EPR spectra for ZnO (red), 10 nm Au/ZnO (black), 20 nm Au/ZnO (violet) and 30 nm Au/ZnO (green). All spectra have the same gyromagnetic ratio with nearly the same spin counts, which is related to oxygen concentration in ZnO.

D.4 Roughness of Au/ZnO film

Figure D.5 shows roughness increases with Au thickness. I also compared the change of surface roughness with Au thickness on glass, and it shows that Au on ZnO film exhibits drastic change in surface roughness with Au thickness. This surface roughness is linked with generation of plasmonic hotspots, and thus have impact on SERS activity.

D.5 Exploring the possibility of Au doping

The Au films change the electronic structure of the underlying ZnO, impacting the bonding, crystallinity, band gap, and luminescence. These changes in electronic properties of the ZnO could arise from the bonding and crystallinity changes from Au film-induced interfacial strain. This does not, however, preclude the possibility of Au(0) doping in the ZnO crystal, given the XRD, Raman, CL, XPS and EPR data.

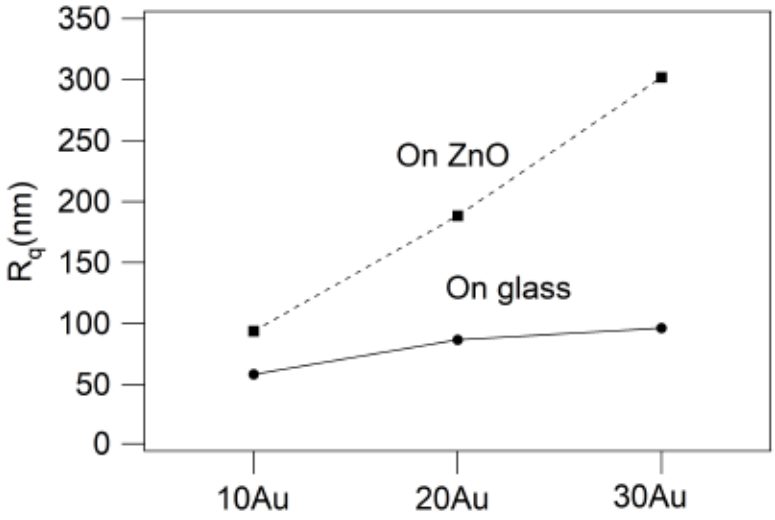

Figure D.5: Roughness of different thicknesses of Au on glass (solid line) and Au on ZnO (dashed line).

D.5.1 XRD data

With increasing Au thickness, all XRD diffraction peaks shifted. The changes in lattice parameter (for detail calculation see D.1) presented in Table D.3 are significant and likely arise from the release of crystal strain due to defects or dopants. [15] The change in lattice parameters is not due to thermal stress introduced during Au deposition, as confirmed by measurements on reference samples of ZnO films placed in the evaporator but blocked from Au coating. The XRD peak positions match between the as-deposited ZnO film and the film which experienced the thermal environment of the evaporator.

Table D.3: The change of lattice parameters (a and c) of ZnO with Au incorporation compared to analogous samples from Chapter 2.

Sample	c (Å)		a (Å)	
	Ch 5	Ch 2	Ch 5	Ch 2
ZnO	5.212	5.150	2.862	2.791
10 or 15 nm Au/ZnO	5.212	5.150	2.871	2.791
20 or 25 nm Au/ZnO	5.218	5.150	2.882	2.793
30 or 35 nm Au/ZnO	5.221	5.151	2.884	2.793

For thin films, interfacial strain impacts the crystal structure of the film significantly. [14, 16] In addition to strain introduced at the Au–ZnO interface, there is a possibility of Au incorporation in this defect-rich ZnO. [13] Others have found changes in lattice parameters for ZnO with deliberate metal doping. [17, 18]

The decrease of peak widths in XRD indicates an increase in crystal domain size. The data in Table D.4 show larger ZnO domain sizes (D) for thicker Au films, as calculated from the Debye–Scherrer equation: [14]

$$D = \frac{K\lambda}{(\mathrm{FWHM})\cos\theta} \tag{D.3}$$

where K is a constant (=0.09), λ is the X-ray wavelength (Cu K-α), θ is the angle of diffraction, and FWHM is full width at half maximum of the (002) peak. This improvement of crystallinity has been linked to Au doping in ZnO materials, [18, 19] but it can also arise from crystal microstrain, which leads to the expansion of crystal domain size. [20]

Table D.4: The ZnO crystal domain size D increases with Au thickness for the defect-rich ZnO, unlike for the ZnO in Chapter 2.

Sample	D (nm), Chapter 5	D (nm), Chapter 2
ZnO	7.01	22.87
10/15 nm Au/ZnO	7.24	22.87
20/25 nm Au/ZnO	11.03	22.87
30/35 nm Au/ZnO	11.09	23.68

D.5.2 Local bonding: Raman and XPS evidence

Raman analysis of ZnO and Au/ZnO substrates offers further insight into the changes in ZnO structure with thicker gold layers. The Raman peak at 368 cm^{-1}, is a shifted ZnO A_1(TO) mode (Figure D.6), while the peak at 265 cm^{-1} is a shifted B_1(TO) mode. [21]. (The symmetric Zn–O stretching mode of $Zn(OH)_2$, if present in the

sample, would also appear near 368 cm^{-1}. [22]) The peak for the [ZnO_4] symmetric stretch [23] at 438 cm^{-1} becomes prominent with thicker Au films, which is consistent with the improvement of ZnO crystallinity from XRD analysis.

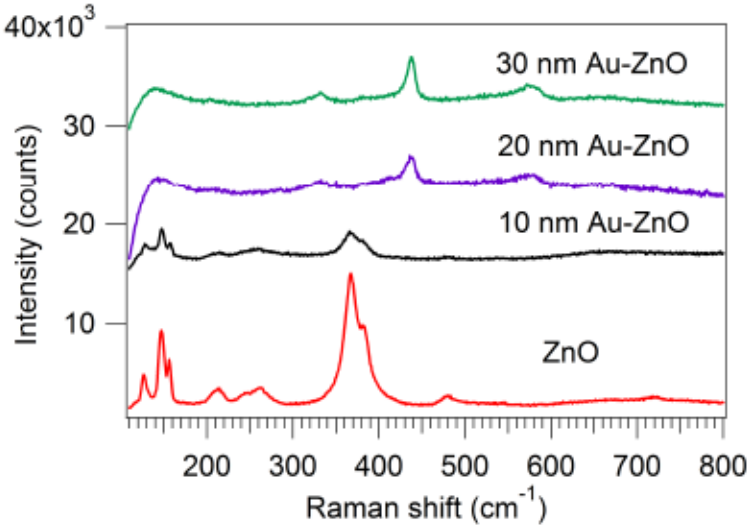

Figure D.6: Raman spectra of ZnO and Au/ZnO samples showing significant changes in the vibrational modes with thicker Au films.

Notable in the Raman analysis is the appearance of a peak at 574 cm^{-1} for both 20 and 30 nm Au/ZnO films, which can be attributed to a shifted lattice mode (A_1(LO)). [2] The presence of this lattice mode peak for samples with thicker Au films also supports the increased crystallinity of those materials. The peak is shifted from its expected position at 580 cm^{-1}, which is attributed to the presence of Au in the ZnO lattice. [13] A shift to lower energy for a Au–O stretch as opposed to a Zn–O stretch is to be expected given the larger reduced mass of Au. [24, 25] Therefore, one cannot rule out the possibility of this peak being a "quasi-LO" mode, [26] where the lattice mode involves Zn, Au and O.

X-ray photoelectron spectroscopy (XPS) was conducted to study the Au–ZnO interaction. From the peak positions, I do not see any evidence of monovalent or trivalent Au, which would have led to a peak shift to higher binding energy.

In Figure D.3 (see the appendix), the $4f_{7/2}$ binding energy peaks of both 20 and 30 nm of Au on ZnO (84.1 eV and 84.3 eV, respectively) were shifted compared to that of 10 nm of Au on ZnO (83.9 eV). This shift is evidence of a changing environment for the Au, [27] although the magnitude of the shift is close to the error in the calibration of the measurement. This interaction is not from Au-Zn bond formation, since there is no Au-Zn XPS peak. [13] In other Au/ZnO hybrid materials, the peak shift is an indication of Au incorporation into the ZnO lattice. [19] Therefore, one cannot rule out Au incorporation in the ZnO lattice. There are examples of Au(0) doping in ZnO from Au sputtering on ZnO [19, 28, 29] or co-precipitation of Au with ZnO. [13]

D.5.3 ZnO luminescence: defects and charge transfer

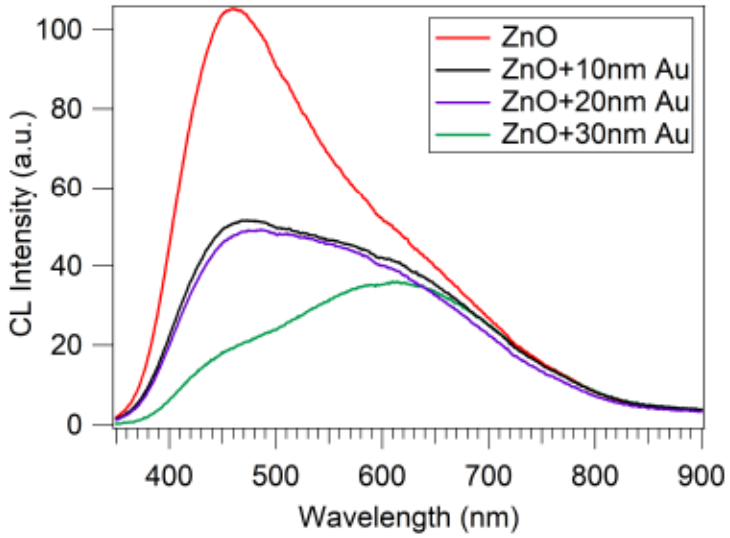

Figure D.7: CL spectra show a drop in the ZnO defect emission peak with increased thickness of the Au film.

The broad spectral envelope seen in the CL spectra in Figure D.7 is composed of the plasmonic response [30, 31] around 650 nm and a shorter wavelength emission due to Zn or O vacancies (plasmon absorption spectrum is shown in Figure 5.5). [32] The drop in the shorter-wavelength emission with the addition of the Au film would

indicate fewer vacancies. Electron paramagnetic resonance (EPR) measurements offer information on the oxygen vacancies. A strong signal with g=2.01 indicates a singly ionized oxygen vacancy (V_{O^+}). [13] From Figure D.4, there are no significant changes in 3 EPR spectra, indicating O_{vac} concentration is not impacted by Au incorporation.

The Au evaporation process could be removing Zn vacancies in the crystal, for example through thermal strain. However, the Zn vacancies are still present in samples, such as in Figure D.7, which were exposed to the thermal environment of the evaporator but blocked from Au deposition. Another reason for quenching of the Zn vacancy emission would be through Au doping in those sites. [13] Finally, in the absence of direct evidence of fewer vacancies, the ZnO defect emission peak can also be quenched due to charge transfer. [33, 34]

Appendix E

Supporting Information: Chapter 6

E.1 Surface morphological information of monometallic substrates

Table E.1: Surface roughness and surface area (5×5 μm^2 scan image) of monometallic substrate and relation with EF

Sample tag	Surface area (μm^2)	R_q (nm)	EF ($\times10^6$)
M1	27.3±0.3	64.31 ± 7.68	0.09 ± 0.06
M2	30.2±0.5	96.24 ± 2.15	1.75 ± 0.18

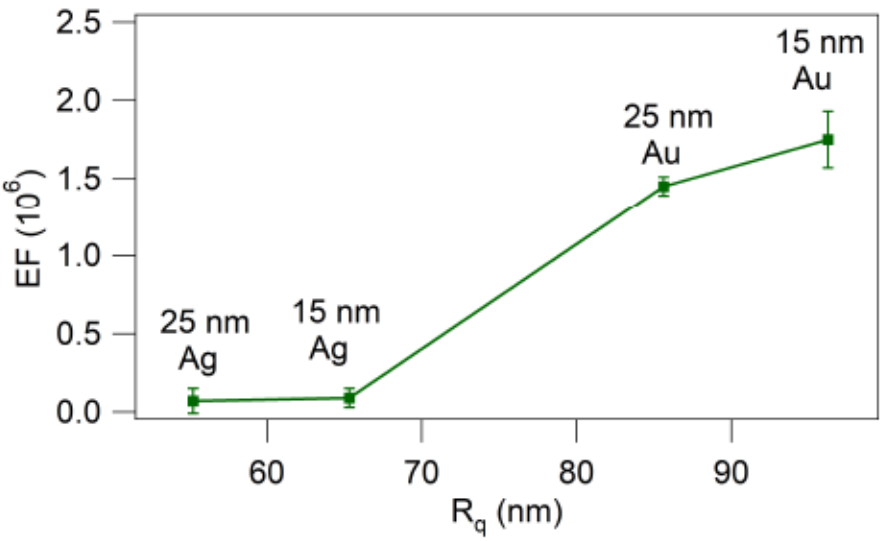

Figure E.1: Surface roughness controls SERS activity in monometallic case.

E.2 EF and surface charge of 25 and 15 nm thick Au and Ag bimetallic SERS substrates

Table E.2: Consistency of surface charge controlled SERS of 25 and 15 nm thick Au and Ag bimetallic substrates.

Sample	Thickness (nm)	Surface charge	SERS activity
Ag on Au	25 on 25	+	SERS-active
Au on Ag	25 on 25	–	SERS-inactive
Ag on Au	15 on 15	+	SERS-active
Au on Ag	15 on 15	–	SERS-inactive

Appendix F

Supporting Information: Chapter 7

F.1 SERS performance with 10 nm of Au

In order to confirm consistent results, a 10 nm Au covered SiO_2 sphere substrate was also tested towards detection of PAHs. As with other substrates discussed in Chapter 7, the Raman peaks of pyrene are highly enhanced compared to phenanthrene (Figure F.1).

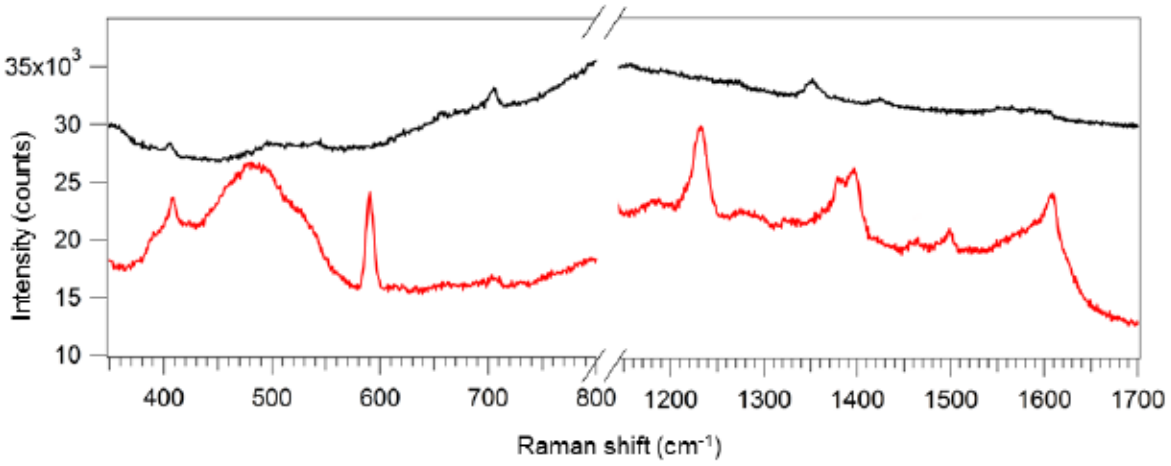

Figure F.1: SERS spectra of phenanthrene (black) and pyrene (red) on 10 nm of Au on SiO_2 spheres show pyrene has high SERS intensity relative to phenanthrene. Spectra are offset for clarity.

F.2 Computational Raman spectra of PAHs in gas phase

Computational Raman spectra (gas phase) of phenanthrene (Figure F.2) and pyrene (Figure F.3) reveal distinct Raman peaks for the two compounds.

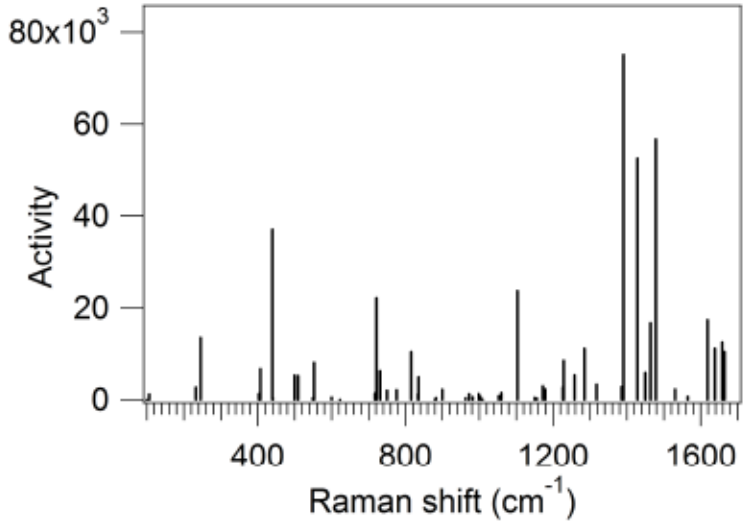

Figure F.2: Computed Raman modes of phenanthrene (gas phase).

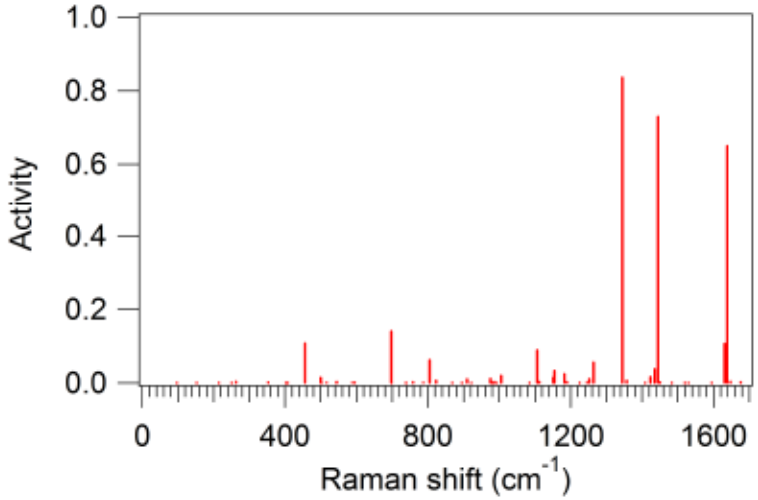

Figure F.3: Computed Raman modes of pyrene (gas phase).

Bibliography

[1] Khan A. Alim, Vladimir A. Fonoberov, and Alexander A. Balandin. Origin of the optical phonon frequency shifts in ZnO quantum dots. *Appl. Phys. Lett.*, 86(5):053103–1, 2005.

[2] M Tzolov, N Tzenov, D Dimova-Malinovska, M Kalitzova, C Pizzuto, G Vitali, G Zollo, and I Ivanov. Vibrational properties and structure of undoped and Al-doped ZnO films deposited by RF magnetron sputtering. *Thin Solid Films*, 379(1):28, 2000.

[3] V. Russo, M. Ghidelli, P. Gondoni, C. S. Casari, and A. Li Bassi. Multi-wavelength Raman scattering of nanostructured Al-doped zinc oxide. *J. Appl. Phys.*, 115(7):073508, 2014.

[4] A. Souissi, A. Marzouki, A. Sayari, V. Sallet, A. Lusson, and M. Oueslati. Origin of the Raman mode at 379 cm^{-1} observed in ZnO thin films grown on sapphire. *J. Raman Spectrosc.*, 42(7):1574, 2011.

[5] James H Nobbs. Kubelka-Munk Theory and the Prediction of Reflectance. *Rev. Prog. Color. Relat. Top.*, 15(1):66, 1985.

[6] Katherine A. Willets and Richard P. Van Duyne. Localized Surface Plasmon Resonance Spectroscopy and Sensing. *Annu. Rev. Phys. Chem.*, 58(1):267, 2007.

[7] E. C. Le Ru, E. Blackie, M. Meyer, and P. G. Etchegoin. Surface Enhanced Raman Scattering Enhancement Factors: A Comprehensive Study. *J. Phys. Chem. C*, 111(37):13794, 2007.

[8] M.G. Donoso, A. Méndez-Vilas, J.M. Bruque, and M.L. González-Martin. On the relationship between common amplitude surface roughness parameters and

surface area: Implications for the study of cell–material interactions. *Int. Biodeterior. Biodegrad.*, 59(3):245, 2007.

[9] Ruth A. McBride, John M. Kelly, and Declan E. McCormack. Growth of well-defined ZnO microparticles by hydroxide ion hydrolysis of zinc salts. *J. Mater. Chem.*, 13:1196, 2003.

[10] Mohd Farhan Khan, Akhter H. Ansari, M. Hameedullah, Ejaz Ahmad, Fohad Mabood Husain, Qamar Zia, Umair Baig, Mohd Rehan Zaheer, Mohammad Mezbaul Alam, Abu Mustafa Khan, Zeid A. AlOthman, Iqbal Ahmad, Ghulam Md Ashraf, and Gjumrakch Aliev. Sol-gel synthesis of thorn-like ZnO nanoparticles endorsing mechanical stirring effect and their antimicrobial activities: Potential role as nano-antibiotics. *Sci. Rep.*, 6:27689, 2016.

[11] Daiming Liu, Qingkang Wang, and Jing Hu. Fabrication and characterization of highly ordered Au nanocone array-patterned glass with enhanced SERS and hydrophobicity. *Appl. Surf. Sci.*, 356:364, 2015.

[12] Rui-wen Shao, Kun Zheng, Bin Wei, Yue-fei Zhang, Yu-jie Li, Xiao-dong Han, Ze Zhang, and Jin Zou. Bandgap engineering and manipulating electronic and optical properties of ZnO nanowires by uniaxial strain. *Nanoscale*, 6:4936, 2014.

[13] Ming-Han Liu, Yun-Wen Chen, Xiaoyan Liu, Jer-Lai Kuo, Ming-Wen Chu, and Chung-Yuan Mou. Defect-Mediated Gold Substitution Doping in ZnO Mesocrystals and Catalysis in CO Oxidation. *ACS Catalysis*, 6(1):115, 2016.

[14] P. Bindu and Sabu Thomas. Estimation of lattice strain in ZnO nanoparticles: X-ray peak profile analysis. *J Theor Appl Phys*, 8(4):123, 2014.

[15] Umair Manzoor, Do K. Kim, Mohammad Islam, and Arshad S. Bhatti. Removal of Micrometer Size Morphological Defects and Enhancement of Ultraviolet

Emission by Thermal Treatment of Ga-Doped ZnO Nanostructures. *PLOS ONE*, 9(1):1, 2014.

[16] A. C. Rastogi, S. B. Desu, P. Bhattacharya, and R. S. Katiyar. Effect of Strain Gradation on Luminescence and Electronic Properties of Pulsed Laser Deposited Zinc Oxide Thin Films. *J. Electroceramics*, 13(1):345, 2004.

[17] K. G. Saw, N. M. Aznan, F. K. Yam, S. S. Ng, and S. Y. Pung. New Insights on the Burstein-Moss Shift and Band Gap Narrowing in Indium-Doped Zinc Oxide Thin Films. *PLOS ONE*, 10(10):1, 2015.

[18] Dojalisa Sahu, N.R. Panda, B.S. Acharya, and A.K. Panda. Enhanced UV absorbance and photoluminescence properties of ultrasound assisted synthesized gold doped ZnO nanorods. *Opt. Mater.*, 36(8):1402, 2014.

[19] Veeradasan Perumal, Uda Hashim, Subash C. B. Gopinath, R. Haarindraprasad, Wei-Wen Liu, P. Poopalan, S. R. Balakrishnan, V. Thivina, and A. R. Ruslinda. Thickness Dependent Nanostructural, Morphological, Optical and Impedometric Analyses of Zinc Oxide-Gold Hybrids: Nanoparticle to Thin Film. *PLOS ONE*, 10(12):1, 2015.

[20] Oshadha K. Ranasingha, Congjun Wang, Paul R. Ohodnicki, Jonathan W. Lekse, James P. Lewis, and Christopher Matranga. Synthesis, characterization, and photocatalytic activity of Au-ZnO nanopyramids. *J. Mater. Chem. A*, 3:15141–15147, 2015.

[21] A. Souissi, A. Marzouki, A. Sayari, V. Sallet, A. Lusson, and M. Oueslati. Origin of the Raman mode at 379 cm^{-1} observed in ZnO thin films grown on sapphire. *J. Raman Spectrosc.*, 42(7):1574, 2011.

[22] Mingsong Wang, Lingxia Jiang, Eui Jung Kim, and Sung Hong Hahn. Electronic structure and optical properties of $Zn(OH)_2$: LDA+U calculations and intense yellow luminescence. *RSC Adv.*, 5:87496, 2015.

[23] Arrigo Calzolari and Marco Buongiorno Nardelli. Dielectric properties and Raman spectra of ZnO from a first principles finite-differences/finite-fields approach. *Sci. Rep.*, 3:2999, 2013.

[24] Xuefeng Wang and Lester Andrews. Infrared Spectra and Structures of the Coinage Metal Dihydroxide Molecules. *Inorg. Chem.*, 44(24):9076, 2005.

[25] Xuefeng Wang and Lester Andrews. Infrared spectrum and structure of the gold dihydroxide molecule. *Chem. Commun.*, page 4001, 2005.

[26] C Kranert, R Schmidt-Grund, and M Grundmann. Surface- and point-defect-related Raman scattering in wurtzite semiconductors excited above the band gap. *New J. Phys.*, 15(11):113048, 2013.

[27] Y. Xu, B. Yao, Y.F. Li, Z.H. Ding, J.C. Li, H.Z. Wang, Z.Z. Zhang, L.G. Zhang, H.F. Zhao, and D.Z. Shen. Chemical states of gold doped in ZnO films and its effect on electrical and optical properties. *J. Alloys Compd.*, 585(Supplement C):479, 2014.

[28] H. Wang, L. Xu, J. Fan, X. Ma, Z. Wei, Y. Zou, and Y. Xu. Study of solid solubility of gold doped in ZnO films and its effect on optical properties. In *2015 International Conference on Optoelectronics and Microelectronics (ICOM)*, page 407, 2015.

[29] Veeradasan Perumal, Uda Hashim, Subash C. B. Gopinath, Haarindraprasad Rajintra Prasad, Liu Wei-Wen, S. R. Balakrishnan, Thivina Vijayakumar,

and Ruslinda Abdul Rahim. Characterization of Gold-Sputtered Zinc Oxide Nanorods—a Potential Hybrid Material. *Nanoscale Res. Lett.*, 11(1):31, 2016.

[30] Arthur Losquin, Luiz F. Zagonel, Viktor Myroshnychenko, Benito Rodríguez-González, Marcel Tencé, Leonardo Scarabelli, Jens Förstner, Luis M. Liz-Marzán, F. Javier García de Abajo, Odile Stéphan, and Mathieu Kociak. Unveiling Nanometer Scale Extinction and Scattering Phenomena through Combined Electron Energy Loss Spectroscopy and Cathodoluminescence Measurements. *Nano Lett.*, 15(2):1229, 2015.

[31] Viktor Myroshnychenko, Jaysen Nelayah, Giorgio Adamo, Nicolas Geuquet, Jessica Rodríguez-Fernández, Isabel Pastoriza-Santos, Kevin F. MacDonald, Luc Henrard, Luis M. Liz-Marzán, Nikolay I. Zheludev, Mathieu Kociak, and F. Javier García de Abajo. Plasmon Spectroscopy and Imaging of Individual Gold Nanodecahedra: A Combined Optical Microscopy, Cathodoluminescence, and Electron Energy-Loss Spectroscopy Study. *Nano Lett.*, 12(8):4172, 2012.

[32] F. Fabbri, M. Villani, A. Catellani, A. Calzolari, G. Cicero, D. Calestani, G. Calestani, A. Zappettini, B. Dierre, T. Sekiguchi, and G. Salviati. Zn vacancy induced green luminescence on non-polar surfaces in ZnO nanostructures. *Sci. Rep.*, 4:5158, 2014.

[33] Xuehong Li, Yang Zhang, and Xijun Ren. Effects of localized surface plasmons on the photoluminescence properties of Au-coated ZnO films. *Opt. Express*, 17(11):8735, 2009.

[34] Ma. De Lourdes Ruiz Peralta, U. Pal, and R. Sánchez Zeferino. Photoluminescence (PL) Quenching and Enhanced Photocatalytic Activity of Au-Decorated

ZnO Nanorods Fabricated through Microwave-Assisted Chemical Synthesis. *ACS Appl. Mater. Interfaces*, 4(9):4807, 2012.